Radio afterglows of Gravitational Waves

Daniele d'Antonio

School of Mathematical and Physical Sciences
Faculty of Science
University of Technology Sydney
NSW - 2007, Australia

Radio afterglows of Gravitational Waves

A thesis submitted in fulfilment of the requirements
for the degree of

Doctor of Philosophy
in
Astrophysics

by

Daniele d'Antonio

to

School of Mathematical and Physical Sciences
Faculty of Science

University of Technology Sydney
NSW - 2007, Australia

December 2022

COVID-19 STATEMENT

The research project presented in this thesis has been impacted by Covid-19. Because of the pandemic, international and national conferences were not held in person. I was hence not able to expand my network of researchers and build up new collaborations.

Moreover, the Laser Interferometer Gravitational-wave Observatory (LIGO) and Virgo suspended their observations in 2020. As a consequence, the PhD project has been repositioned by modifying the methodology and research topic. The project was originally supposed to be a study on radio transients with a particular focus on gravitational wave events. However, a study of variable galactic nuclei was inserted and the study of gravitational waves was from a more theoretical approach.

During the pandemic, Australian borders were closed and universities in Australia fired part of their staff as the number of international students dramatically decreased in 2020 and 2021. In those uncertain times, my main supervisor, Martin Bell, decided to resign from his position as a researcher at the University of Technology, Sydney. He decided to leave research and start a career as a data scientist at the University of Newcastle. During the year 2022, I never met with my supervisor in person and all our meetings were held online. He did everything possible to give me support and proper supervision. Nevertheless, remote supervision clearly made this PhD project more challenging.

Abstract

This thesis describes a study of the research conducted by myself during these years as a PhD candidate working at the University of Technology, Sydney (UTS) and the Commonwealth Scientific and Industrial Research Organisation (CSIRO). The thesis is divided in two main parts: the first part is comprised of research analysing the radio variable sky with a *classical* approach while the second part proposes the usage of statistical techniques poorly used in Astrophysics at the moment of writing this work.

Firstly, a comprehensive description of the instrumentation which has involved my research work. The instrumentation consists in the Australia Telescope Compact Array (ATCA), The Australian Square Kilometre Pathfinder (ASKAP), the Swift Gamma-ray Burst Explorer (*Swift*), the High Energy Stereoscopic System (HESS) and the two Michelson interferometers the Laser Interferometer Gravitational-Wave Observatory (LIGO) and Virgo. Principles of radio astronomy observations are also reported.

Secondly, a transients follow-up with the Australia Telescope Compact Array is presented. The research project comprised the study of the gamma-ray burst GRB190114c, the two flare stars AT Mic and UV Ceti. The investigation has been carried out by using the Rapid Response Mode. This modality consists in triggering radio telescopes as soon as a transient is detected by X-ray and gamma-ray telescopes. The analysis of the gamma-ray burst revealed possible scintillation while the flare stars activity could be due to gyrosynchrotron radiation, electron cyclotron maser or plasma radiation. Furthermore, campaign for detecting ultra-cool dwarfs (UCDs). These objects are hardly detectable and at the time of writing this work, only 25 sources were detected. The campaign is based on searching for objects with photometric variability and fast rotation. The search allowed to detect at least 3 objects from 11 radio observations.

Moreover, a study of variable active galactic nuclei (AGN) using the Australian Square Kilometre Pathfinder (ASKAP) is outlined. This research has been conducted with a targeted approach by selecting ASKAP sources listed in AGN catalogues. The study showed the detection of 30 variable AGN. The most likely explanation for their radio variability is scintillation because of the brightness temperature values above the Compton catastrophe limit of 10^{12}K.

Finally, the second part of this thesis is an analysis of innovative methods for studying variable and transient sources in Astrophysics. The work involves the study of light curves by using statistical methods named State Space Models. These models can be used for detecting a transient source hosted by a variable active galaxy. In this thesis, a method for detecting a gravitational waves event hosted by a hypothetical active galaxy

is explained. In addition, State Space Models can also encode several properties in light curves, such as slope, rise or decline for a given time t.

The conclusions of this thesis summarise the main results and the possible developments of the research projects described in the other chapters.

The thesis also contains an appendix showing fragments of the code used for testing State Space Models on astronomical time series data.

AUTHOR'S DECLARATION

I, *Daniele d'Antonio* declare that this thesis, submitted in fulfilment of the requirements for the award of Doctor of Philosophy, in the *School of Mathematical and Physical Sciences*, *Faculty of Science* at the University of Technology Sydney. This thesis is wholly my own work unless otherwise referenced or acknowledged. In addition, I certify that all information sources and literature used are indicated in the thesis. This document has not been submitted for qualifications at any other academic institution. This research is supported by the Australian Government Research Training Program and the Australian Research Council.

SIGNATURE: Production Note: Signature removed prior to publication.

[Daniele d'Antonio]

DATE: 16th December, 2022

PLACE: Sydney, Australia

Dedication

To my parents and my sister
Ai miei genitori e mia sorella

ACKNOWLEDGMENTS

I feel like I started this PhD yesterday. I still remember how I was feeling my first day at UTS. How nervous I was! I could not wait to start this journey! The first time I stepped into Martin's office to talk about my project I could not be more excited! However, everything comes to an end and here I am writing this section and having a final look at this thesis after three years and half of being a PhD student in Sydney. Time flies!

During these years, my supervisor Martin Bell, has always been a good fella. He assisted me not just on research but also on life in general. Martin, thank you for all our chats. Thank you for checking on me and for sharing your life experience when I broke up with my ex girlfriend. Besides, I will never forget how you did anything possible to supervise me even when you were no longer in Sydney. You didn't even get paid to supervise me anymore but you kept helping me whenever I needed. Maybe I could go to Newcastle and see you for a beer after submitting this thesis!

I'd like to thank also the great researchers I worked with in Australia such as Gemma Anderson who gave me the opportunity to explore the world of gamma-ray bursts and flare stars. It was great to chat with you in person in Narrabri. What a pity that the pandemic made that to be our first and last meeting in person. Thanks to Vanessa Moss who assisted me when I worked at CSIRO and when I had to deal with ATCA observations. You were so easy going and friendly since our first chat! I will always remember our chat about my future, when we talked about a career in research or industry. I also remember when you introduced me to Matthew Bailes. Thanks for everything you have done!

I want to thank Tara Murphy as well. It's been exciting to work in your research group and learn about radio and variable transients. Thanks for your efforts on granting me a PhD stipend during these years. Without those funds my PhD would not be possible. A thing I always appreciated of you is that you are always clear and direct on giving feedback and comments. This makes you tough sometimes but also honest.

I also want to thank James Brown who assisted me on the last two chapters of this

thesis and also made our meetings nice with our funny chats. Your comments were useful and precise but at the same time you helped me to understand that researchers shouldn't take themselves too seriously sometimes!

I can't not mention the people I came across these years at UTS. PhD means years of work but also fun. I shared my office with several people and I can't forget of Aishwarya whose the name still worries me when I have to write it. Now, I hope I wrote it well (damn! why didn't I give her a short easy nickname these years???). Thanks for being my main mate at the office. Thank you Trudy for being there and stand me whenever you came to the office. Natalia, thank you. You did not spend much time with us at UTS but those six months together have been amazing! Virginia, thanks for your company as well. Thanks to Luca who has been one my best friends. I missed you when you left UTS. We had good fun together. Thank you Matias and Tom for the nice time we spent together!

Thanks to Clara and Gioacchino who learnt all my PhD drama stories in these years! Coogee life wouldn't be the same without the two of you! Thank you Arnolda for our friendship! How crazy is the way we met in Sydney!? These years would not have been the same without you!!! Giulia and Christian also deserve a mention here. You guys helped me a lot on starting a life in Sydney!! Living with you guys has been great! You guys are the only flatmates I wouldn't get tired of! Giulia, the story our friendship is just great! That's amazing how we met at university in Italy and then re-met here in Sydney. It's true I followed you though (ahahaha).

Thank you Jessie. You just came to my life but you already mean a lot to me. You made this final stage of my PhD life a wonderful time. I feel soooo lucky I met you.

Finally, I really want to thank my parents mamma and papa', my sister and zio Remo for being always supportive and helpful during these four years in Australia. We were far but at the same time close, especially when I had just arrived in this country and I was alone on the other side of the World. My family always supported me in every decision since I was born. They indeed supported me when I decided to become an astrophysicist. I couldn't ask for a better family!

Table of Contents

List of Figures xv

List of Tables xxiii

1 Introduction 1

1.1 Preface . . . 1
1.2 Instrumentation . . . 2
1.2.1 The Australia Telescope Compact Array . . . 2
1.2.2 The Australian Square Kilometre Array Pathfinder . . . 11
1.2.3 Swift Gamma Ray Burst Explorer . . . 21
1.2.4 High Energy Stereoscopic System . . . 24
1.2.5 LIGO and Virgo detectors . . . 24
1.3 Outline of science chapters: studying radio transients and variables . . . 27

I Part I 31

2 Transients follow-up with the Australia Telescope Compact Array 33

2.1 ATCA Rapid-Response and Monitoring Follow-up of TeV Gamma-ray Bursts 34
2.1.1 Gamma-ray bursts progenitors and classification . . . 34
2.1.2 Gamma-ray emission . . . 35
2.1.3 X-ray emission . . . 36
2.1.4 Radio emission . . . 36
2.1.5 GRB mechanism . . . 36
2.1.6 ATCA Rapid Response Mode . . . 37
2.1.7 The necessity of a rapid radio follow-up of GRBs with the ATCA . 38
2.1.8 Detection of GRB190114C . . . 38
2.1.9 Radio observations and data reduction . . . 39
2.1.10 Results and discussion . . . 39

2.2 ATCA Rapid response of flare stars . . . 42
2.2.1 Introduction . . . 42
2.2.2 High energy emission . . . 42
2.2.3 Radio emission . . . 42
2.2.4 The necessity of a rapid radio follow-up of flare stars with the ATCA 43
2.2.5 Detection of AT Mic and UV Ceti . . . 44
2.2.6 Radio observations and data reduction . . . 45
2.2.7 Results and discussion . . . 45
2.3 Uncovering the population of radio ultra-cool dwarfs . . . 48
2.3.1 Introduction . . . 48
2.3.2 Unresolved issues . . . 48
2.3.3 Method of investigation and initial results . . . 49

3 Radio variability of active galactic nuclei in the VAST pilot survey 53
3.1 Introduction . . . 53
3.2 Data . . . 55
3.2.1 ASKAP Data . . . 55
3.2.2 AGN catalogues . . . 56
3.3 Sample selection . . . 58
3.3.1 Catalogues cross-matching technique . . . 59
3.3.2 Variables selection method . . . 59
3.4 Results . . . 62
3.4.1 Variables and their classification . . . 62
3.4.2 Explanation of the radio variability . . . 63
3.4.3 Scintillation as a function of Galactic latitude . . . 64
3.4.4 Single source analysis . . . 70
3.5 Discussion and conclusions . . . 70

II Part II 77

4 Modelling time series in Astrophysics 79
4.1 Why State Space Models? . . . 80
4.2 The first gravitational waves source observed by telescopes: GW170817 . 82
4.2.1 The discovery of gravitational waves . . . 82
4.2.2 Electromagnetic emission models of GW170817 . . . 84

4.3 An alternative way for time series analysis in Astrophysics: State Space Models . . . 87
4.3.1 The current method for time series analysis . . . 87
4.3.2 Introduction to State Space Models . . . 90
4.3.3 Fitting GW170817 radio light curve with State Space Models . . . 91
4.4 Conclusions and possible developments . . . 108

5 Using State Space Models for detecting gravitational waves 111
5.1 The case of the fast radio burst FRB 50418 . . . 112
5.2 Detecting a gravitational waves event in a simulated host active galaxy . 114
5.2.1 Conditions and scenarios for detecting transients within an active galaxy . . . 114
5.2.2 Using State Space Models for detecting transient signals . . . 116
5.2.3 Change points search in time series . . . 119
5.3 Conclusions . . . 124

6 Conclusions 125
6.1 Main thesis findings and future research . . . 125
6.1.1 Gamma-ray burst GRB190114C investigation . . . 125
6.1.2 A flare stars study . . . 126
6.1.3 Radio variable AGN in VAST-P1 and RACS . . . 127
6.1.4 State Space Models in time domain astronomy . . . 128

A Appendix 131
A.1 State Space Models in Python . . . 131

Bibliography 139

List of Figures

Figure **Page**

1.1 Five of the six antennas of the Australia Telescope Compact Array (Narrabri, New South Wales, Australia). Credit: Wilson et al. (2011). 3

1.2 Graph of a Cassegrain radio telescopes. Credit: S.T. Myers [1] 4

1.3 Representation of two antennas tracking a source with position vectors and baseline. The source is the outline on the celestial sphere. Credit: Thompson et al. (2017) . . . 5

1.4 (u,v)-coverage of an interferometer set out in a logarithmic spiral pattern comprised of 2, 5, 10 and 5 antennas (top to bottom) and observing for 10 seconds, 2, 4, and 6 hours (left to right). Credit: Avison & George (2012). 7

1.5 Geometry of a source with intensity $I(l,m)$ with an interferometer where the baseline vector has components (u,v,w). Credit: Thompson et al. (2017) 8

1.6 Mapping the celestial sphere onto one image plane in one dimension. The point C is the field centre. The position of the point P is estimated with the direction cosine m with respect to the v axis. The projection into a plane surface P appears in P' with a distance from C which is proportional to $sin\phi$. Credit: Thompson et al. (2017) 9

1.7 Radio spectrum of interference for the years 2011, 2015 and 2018 in the 16cm band from the ATCA User Guide. The different colours refer to different sources of the signal which are reported at the top of the graph. 10

1.8 RFI in 15mm band from the ATCA User Guide. The interference is evident from the three high peaks. 12

1.9 The Australian Square Kilometre Array (ASKAP). Credit: Hotan et al. (2021). . . . 13

1.10 Sensitivity profile over the field of view of ASKAP. The data were obtained with a 1.05 deg beam pitch and a centered frequency of 888 MHz. Credit: Hotan et al. (2021). 15

1.11 Overview of the ASKAP systems (Hotan et al., 2021). 17

[1] http://www.aoc.nrao.edu/~smyers/Synth2004/MyersPolarization04print.pdf

1.12 Footprint of VAST-P1 with the number of observations for each field. There is also the VAST-P2 mid-band footprint (green regions). The sky map is based on J2000 equatorial coordinates in the Mollweide projection. The background is based on diffuse Galactic emission at 887.5 MHz modelled by Price (2016) and Zheng et al. (2016). Credit: Murphy et al. (2021). 19
1.13 Graph of the *Swift* satellite with its components. Credit: *NASA*. 22
1.14 The High Energy Stereoscopic System. Credit: Credit: webpages of HESS.[2] 24
1.15 Simple graph explaining how a Michelson interferometer works. A laser beam is splitted in two beams though a Beam-splitting mirror. Each beam is directed to a mirror and then come back to the Beam-splitting mirror. Credit: ScienceNews [3] . . 26
1.16 The LIGO Hanford (left) and LIGO Livingston (right) interferometers. 26
1.17 The Virgo interferometer. 27

2.1 Representation of the GRB mechanism. (Credit: earthsky.org [4]). 37
2.2 Light-curve of GRB190114C. 41
2.3 AMI-LA 13-18 GHz (blue circles) and Swift WT/PC (green diamonds/orange squares) 0.3-10 keV light curves on a logarithmic scale. For clarity, error bars are not plotted but for both radio and X-ray data are typically ≤15 per cent. In X-rays the source was brightest at the first measurement, two minutes after the initial trigger, and then declined for around the first hour, re-brightening somewhere between 0.075 and 0.125 d. The radio flux (in blue) behaved similarly, with a bright, strong detection in the first measurement at 6 min, followed by a decline and subsequent rebrightening. A second, clearly resolved, radio flare occurred at around 1.1 d. By about four days the radio flux had settled down to a quiescent level of a few mJy. Credit: Fender et al. (2014). 43
2.4 VLA light curve of a giant radio flare seen from the dMe EV Lac. Each tick corresponds to 10 s and the inset shows the variation in circular polarisation on 5 min timescales during the flare decay phase. Credit: Osten et al. (2005). 45
2.5 Light-curve of AT Mic in 4cm band 46
2.6 Light-curve of UV Ceti in the 4cm band. 46
2.7 The collected literature detections and limits of UCD quiescent radio emission specific luminosity as presented by Pineda et al. (2017). Radio emission in Utra-cool dwarfs (UCD) is rare. 49

[2] https://www.mpi-hd.mpg.de/hfm/HESS/
[3] https://www.sciencenewsforstudents.org
[4] https://earthsky.org/space/

2.8 Top - Preliminary light curve in the 5.5 GHz band binned at 36s for ATCA test observations of J2228-4310, revealing bursts in Stokes V and Stokes I. Bottom - Same as top, but for the 9 GHz band, partly contaminated by RFI, and showing a spectral dependence to the polarized burst emission. Credit: Sebastian Pineda. 50

3.1 Log scale modulation index (percentage) vs. χ^2 of all the 422 155 VAST-P1 sources obtained from the sample selection (see Section 3.3). The histogram on the top is the χ^2 distribution while the histogram on the right is the modulation index distribution. The red sources are the non-variable AGN of our sample. The yellow star-like objects are the variable AGN. Sources in the top-right quadrant are variable candidates. . . 61

3.2 Modulation index (percentage) vs. χ^2 plot of all the 4008 AGN from this study that are found in VAST-P1. We divided the AGN per class. Both steady objects and variables are reported. The variable AGN are the star-shape markers in the graph. The biggest star-shape markers indicate the high variable AGN. The vertical and the horizontal black lines delimit the threshold values of modulation index and χ^2 for selecting variables. 63

3.3 Histogram of the timescale that we estimated for every variable. Most variable AGN show variability in a time interval between 1 and 9 days. 65

3.4 Distribution of brightness temperature values (logarithm scale) of the sample of variable AGN. The values above 10^{12}K show that the variability is due to scintillation. 65

3.5 Modulation index vs. timescale. In these two plots we have the modulation index values predicted by the scintillation model, as well as the observed modulation index values. The orange and red triangles are the observed data (plot on the top). Most sources have modulation indices below the predictions (red triangles pointing down). Four objects have observed modulation indices values larger than the predicted ones (oranges triangles pointing up). Objects with the grey tick-up are high variables. The plot on the bottom shows the objects by class. All variable BL Lacs have modulation index values below the predictions. 67

3.6 Measured timescale vs. Predicted timescale. Objects on the green line have a measured timescale consistent with the predicted one. For objects below the green line, the predicted timescale is longer than the observed one. For objects above the line, the opposite is true. The objects with the grey tick-up are highly variables. 68

3.7 Radio images of the 6 high variable AGN. Each source is in the centre of its radio image. VAST 090626.8+033311 is a Seyfert galaxy while the other plotted sources are QSOs. 72

3.8 Light curves of the variable AGN. The black points are Selavy measurements while the red triangles are forced measurements. 73

3.8 (continued) Light curves of the variable AGN. The black points are Selavy measurements while the red triangles are forced measurements. 74

3.8 (continued) Light curves of the variable AGN. The black points are Selavy measurements while the red triangles are forced measurements. 75

4.1 Images cutout from three radio telescopes: Giant Metrewave Radio Telescope (GMRT), Very Large Array (VLA) and Australia Telescope Compact Array (ATCA). The two black lines indicate the position of the gravitational waves source. Panels (a), (b) and (c) show images from August to September 2017. Panels (d), (e) and (f) show images from October 2017. The white ellipse in the lower right corner of each image is the synthesised beam. Credit: Mooley et al. (2018). 83

4.2 In each figure, the eye indicates the line of sight. Model (A) is a classical weak sGRB with an ultra-relativistic jet on-axis. Model (B) is a classical strong sGRB with an ultra-relativistic jet slightly off-axis. Model (C) is a mildly relativistic, wide angle, strong cocoon with a chocked jet. Model (D) is a mildly relativistic, wide angle, weak cocoon with a jet coming out from the lobe. Credit: Kasliwal et al. (2017). 85

4.3 GW170817 radio light curve of the first 300 days. The data are scaled to 1.4 GHz given a spectral index $\alpha = -0.58$ ($S \propto \nu^{\alpha}$). The blue fitting line with the shaded uncertainties region is the power law from Dobie et al. (2018). Credit: Dobie et al. (2019). 88

4.4 Plot of the two variability parameters for the radio sources of the VAST Pilot Survey Phase I (Murphy et al., 2021). Sources in the yellow region are classified as variables. These variables exceed 2σ for each parameter distribution, fitting a Gaussian function. Credit: Murphy et al. (2021). 89

4.5 Local level model fitting GW170817 (Dobie et al., 2018). The black points (with their errors also in black) are data from Dobie et al. (2018). The blue line is the modelled fit of the light curve. Every modelled value at the time t is estimated based of the value of the previous modelled value at the time $t-1$. Hence, the model is "one step ahead." The light blue area is the 95% confidence region. Obviously, the negative values included in the confidence region should be ignored. 92

4.6 Example of heteroscedastic data set (top) and homoskedastic data set (bottom). The two plots show the behaviour of residuals vs. a variable X. The residuals are the difference between the predicted values (red fitting) and the actual measurements. Credit: The Free Encyclopedia. [5] 94
4.7 Autocorrelation function of GW170817 light curve. 95
4.8 Local Linear Trend Model fitting GW170817 (Dobie et al., 2018). The black points (with their errors also in black) are data from Dobie et al. (2018). The blue line is the modelled fit of the light curve. The light blue area is the 95% confidence region. Obviously, the negative values included in the confidence region should be ignored. . 98
4.9 AR model in space state representation form (blue fitting and light blue confidence region) with GW170817 light curve (black points and black error bars). 100
4.10 ARIMA model in space state representation form (blue fitting and light blue confidence region) with GW170817 light curve (black points). 103
4.11 Autocorrelation function of the residuals from the Local Level Model. The blue area is the confidence region which is included in the interval $\pm 1.96\sqrt{N}$. 105
4.12 Residuals vs. time for the Local Level Model. 105
4.13 Plot of the residuals fitted a normal distribution (black fitting). 107
4.14 Q-Q plot of the residuals. 107

5.1 Radio light curve at 5.5 GHz of the source (FRB 50418) within the galaxy WISE J071634.59−190039.2. Black crosses are ATCA observations, blue triangles JVLA observations, and red squares VLBA, e-MERLIN and EVN. Credit: Johnston et al. (2016). 113
5.2 GW170817 hosted by a faint AGN. The transient source is between 1000 and 1200 days of observations. The host galaxy is much fainter than the gravitational waves source. It is then simple to detect a transient source. 115
5.3 GW170817 hosted by a bright AGN. The transient source is between 1000 and 1200 days of observations. The brightness of the host galaxy is comparable the one of the transient. It is then very challenging to detect a transient source. 115
5.4 GW170817 hosted by a bright AGN. The transient source is between 1000 and 1200 days of observations. The mean brightness of the host galaxy is much lower than the one of the transient. However, there are a few measurements comparable to the ones of the transient. 116

[5] https://en.wikipedia.org/wiki/Homoscedasticity and heteroscedasticity

5.5 GW170817 hosted by a bright AGN. The transient source is between 1000 and 1200 days of observations. However, the presence of the source is not evident as it is within a variable active galaxy. 117
5.6 Local Level Model fitting the light curve. The error bars were omitted to clearly show the model fitting the data. 118
5.7 SSARIMA(3,1,25) model fitting the light curve. The light blue region is the 95% confidence region. The error bars were omitted to clearly show the model fitting the data. 118
5.8 SSARIMA(3,0,0) model fitting the light curve. The light blue region is the 95% confidence region. The error bars were omitted to clearly show the model fitting the data. 119
5.9 Local Level Model compared to the mean flux density. The blue trend is the prediction of the Local Level Model while the black line is the level of the mean flux density of the light curve. 120
5.10 Example of change points in a time series. The change points are highlighted by the red vertical lines. The change points divides the time series into segments with different statistical characteristics (standard deviation in this case). Credit: webpages of Arc GIS Pro.[6] 121
5.11 Illustration of sliding windows in time series. Credit: Aminikhanghahi (2016). . . . 121
5.12 Illustration of two adjacent sliding windows in a given time series T. The dashed line is the signal. The two rectangles are two sliding windows covering a time interval $a \leq t$ and $b \geq t$, respectively. 122
5.13 Schematic view of the Window-based change point detection method. The time series on the top is the original signal, the one in the middle is the discrepancy curve and the one on the bottom is still the discrepancy curve where the peaks of the curve are highlighted. We have a change point for each peak of the discrepancy curve. Credit: Truong et al. (2020). 122
5.14 Change points location detected with the window-based method. 124

A.1 State Space Autoregression Model analysis. 132
A.2 Code for fitting State Space Autoregression Model on a time series. 133
A.3 AR model in space state representation form (blue fitting and light blue confidence region) with GW170817 light curve (black points and black error bars). 134

[6] https://pro.arcgis.com/en/pro-app/2.9/tool-reference/space-time-pattern-mining/how-change-point-detection-works.htm

A.4 Code for defining the LocalLinearTrend class which is used for Local Liner Trend Models and Local Level Models. 135
A.5 Matrices defining the Local Linear Trend Model. 135
A.6 Code for fitting the Local Level Model on a time series. 136
A.7 Local Level Model (blue fitting and light blue confidence region) with GW170817 light curve (black points and black error bars). 137

List of Tables

Table **Page**

1.1 Observing features reported in the ATCA Users Guide. 4
1.2 Observing features of ASKAP from Hotan et al. (2021). 14
1.3 VAST observing capabilities. Some VAST-P2 parameters could be different when the survey is carried on. The VAST-P2 parameters which can change in future are the number of epochs, the minumum and maximum spacing and the image rms per epoch at 1296 MHz. These numbers are in italics. Credit: Murphy et al. (2021). 19
1.4 Observing capabilities of *Swift* 22
1.5 Observing capabilities of BAT. 23
1.6 Observing capabilities of XRT. 23
1.7 Observing capabilities of UVOT. 23
1.8 Observing capabilities of HESS. H.E.S.S. II refers to the biggest antenna of the array while H.E.S.S. I to the other four antennas. Credit: webpages of HESS. [7] 25

2.1 Radio observations of GRB190114C with the ATCA. 40
2.2 Radio observations of AT Mic and UV Ceti with the ATCA. The flux calibrator PKS B1934-638 is reported as 1934-638. 47
2.3 Detection of ultracool dwarfs summary with name of the source, date of observation, and polarisation regime reporting 'yes' for detections and 'no' for non-detections. 51

3.1 The AGN catalogues used in this study, including the total number of sources per catalogue and the number of AGN for each class: FSRQs, BCUs, BL Lacs, QSOs and active galaxies. The class 'Active galaxies' contains Seyfert galaxies, LINERs and galaxies with nuclear H II regions. 57

[7] https://www.mpi-hd.mpg.de/hfm/HESS/

3.2 This table shows the sources in common among the AGN catalogues. Each number indicates how many sources there are in common between the catalogues in the corresponding row and column (e.g. KDEBLLACS and BZCat have 19 sources in common). KDE stands for KDEBLLACS and WIB stands for WIBRaLS2. All the numbers in this matrix, refer to sources found in VAST-P1. 58

3.3 χ^2 and flux density mean values of the 4006 AGN from this study that are found in VAST-P1. The χ^2 and flux density errors are the standard deviations of the mean. In this table the entire AGN sample is divided in two groups: blazars and non-blazar AGN. We also describe three classes of blazars (FSRQs, BL Lacs and BCU) and two classes of non-blazars (QSOs and Active Galaxies). The Active Galaxies class is composed of LINERs and Seyfert Galaxies. . . . 66

3.4 Proportion of variables in each AGN class and for the overall study, expressed as both a ratio and a percentage. 72

3.5 Main properties of the Véron and KDEBLLACS variable AGN. The KDEBLLACS AGN are in the last five rows. For each source we report the VAST-P1 name, spectral class, χ^2 value, modulation index and redshift. 76

4.1 The following statistical parameters for the Local Level Model are listed: Aikaike Information Criterion (AIC), Bayesian Information Criterion (BIC), Hannan-Quinn Information Criterion (HQIC) and Heteroskedasticity (H). . 97

4.2 The following statistical parameters for the Local Linear Trend Model are listed: Aikaike Information Criterion (AIC), Bayesian Information Criterion (BIC), Hannan-Quinn Information Criterion (HQIC) and Heteroskedasticity (H). 99

4.3 The following statistical parameters are listed: Aikaike Information Criterion (AIC), Bayesian Information Criterion (BIC), Hannan-Quinn Information Criterion (HQIC) and Heteroskedasticity (H). The model is an Autoregressive (p=2) State Space Model. 100

4.4 The following statistical parameters are listed: Aikaike Information Criterion (AIC), Bayesian Information Criterion (BIC), Hannan-Quinn Information Criterion (HQIC) and Heteroskedasticity (H). The model is a State Space ARIMA (1,2,1). 102

4.5 Confidence region width of the five models adopted: Local Level Model (LLM), Local Linear Trend (LLT) Model, State Space AR(2) Model, SSARIMA (1,2,1) and SSARIMA(2,1,1) with missing values. The first data point over time was not included for estimating these parameters. 103
4.6 Statistical results of the four models adopted: Local Level Model (LLM), Local Linear Trend (LLT) Model, State Space AR(2) Model and SSARIMA (1,2,1). . 104

5.1 Statistical results of the four models tested: Local Level Model (LLM), Local Linear Trend (LLT) Model, State Space AR(3) Model and SSARIMA (3,1,25). 117

CHAPTER 1

INTRODUCTION

1.1 Preface

This thesis is focused on time domain astronomy, a branch of Astrophysics studying the time evolution of astronomical objects. Examples of sources which are commonly studied are gamma-ray bursts, pulsars, supernovae, novae, active galactic nuclei, fast radio bursts, binary stars and more. Sources are classified as *transients* when they are undetectable, then show a "flash" for a certain time interval, and then disappear again. Alternatively, sources are instead *variables* when detectable all the time but show dynamic changes in luminosity.

One of the earliest references to time domain astronomy was Galileo Galilei's work *Letters on Sunspots*, with which an astronomical object was described with dark spots on its surface. This was against Aristotle's idea of a perfect and unchangeable Universe over time. William Herschel also gave a great contribution to time domain astronomy with the discovery of Uranus in 1781. This was the first detection of a planet since ancient times and he went on to discover two moons of Saturn, the seasonal changes of the martian ice caps and infrared radiation. His sister, Caroline Herschel also discovered eight comets. John Herschel (son of William) also made relevant discoveries in astronomy by discovering four galaxies: NGC 7, NGC 10, NGC 25 and NGC 28. Remarkable are also the studies on Cepheid variable stars lead by Edwin Hubble. Hubble demonstrated that the object called Andromeda nebula was a galaxy and not a cloud or stellar cluster within the Milky Way as part of the astronomical community had theorised.

Thanks to the fluctuations in light of these variable stars, Hubble was able to estimate the distance between the Earth and the Andromeda nebula. In detail, to calculate this distance, Hubble used the relationship between the period of the Cepheid fluctuations and its luminosity. He calculated a distance of 900,000 light years which was beyond the borders of the Milky Way Galaxy (the largest estimates of its size showed a diameter at roughly 300,000 light years). Hence, the Andromeda nebula could not be a source within the Milky Way and had to be an external galaxy.

Since then, the development of advanced telescopes allowed astronomers to make more and more progress on understanding the physical nature of celestial objects. Nowadays, it is possible to lead detailed investigations such as analysing the spectral variability and the magnetic field activity of an active galactic nucleus (e.g. McCallum et al. 2007) or detecting and exploring the progenitors of gravitational waves (e.g. Abbott et al. 2016a).

In this thesis, I aim to better understand the physics behind gamma-ray bursts and flare stars and the most likely explanation for the radio variability of a sample of Active Galactic Nuclei at 888 MHz. I also propose innovative statistical time series models for selecting transients and variables. In this Chapter, I first give a description of the instrumentation used for the research presented in this thesis. At the end of this chapter, there is also an outline of the science chapters of this work (see Section 1.3).

1.2 Instrumentation

In this section, I describe the instrumentation used for the science chapters of this thesis. The instrumentation is comprised of radio telescopes, telescopes on board of satellites to perform observations at high energies and gravitational waves detectors.

1.2.1 The Australia Telescope Compact Array

Located at the Paul Wild Observatory near Narrabri in the state of New South Wales in Australia, the Australia Telescope Compact Array (ATCA) is an array of six 22-m radio antennas with a Cassegrain design, including receivers located in a turret that protrudes through the main reflector surface (see Fig. 1.1 and 1.2). The array was built with the target of keeping Australia as a leading country in radio astronomy and is managed by the Australia Telescope National Facility (ATNF).

Figure 1.1: Five of the six antennas of the Australia Telescope Compact Array (Narrabri, New South Wales, Australia). Credit: Wilson et al. (2011).

1.2.1.1 Array Configuration

It is possible to move five antennas along a 3Km east-west track system and this allows different baselines (distance between two antennas) depending on the angular resolution required. One antenna is fixed at 3Km to the west of the east-west track. Hence, the longest baseline available is 6Km while the shortest is 30.6m (ATCA User Guide [2]).

The compact array covers a wide frequency range (between ~1.1 GHz and 105 GHz) corresponding to five wavelength bands between 27 cm and 3 mm. The observing features of the array are shown in Table 1.1. Every frequency range is called a band and each antenna has five feedhorns (only four on antenna 6) that collect radio signals. One feedhorn operates in the 16cm band, another one at 4cm and three at 15mm, 7mm and 3mm. The feedhorns are located on a rotating turret and the orientation of the turret depends on the frequency selected because the turret orients the feedhorn suitable for the band chosen by the observer. Once the feedhorn has received the radio signal it is fed to the receivers for amplification and conversion to standard intermediate frequencies. Every antenna allows four intermediate frequency (IF) outputs which are two polarisations and two frequency bands. The purpose is to have simultaneous observations of two polarisations at the two observing frequencies.

[2] https://www.narrabri.atnf.csiro.au/observing/users_guide/html/atug.html

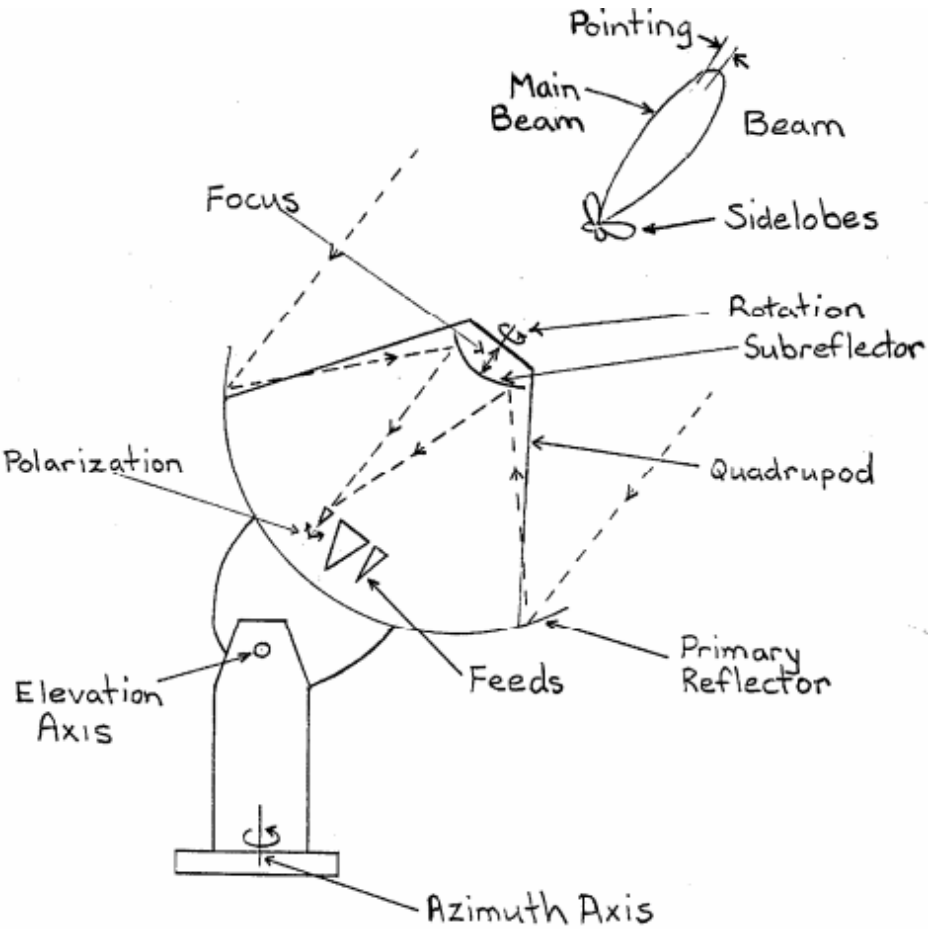

Figure 1.2: Graph of a Cassegrain radio telescopes. Credit: S.T. Myers [1]

.

Table 1.1: Observing features reported in the ATCA Users Guide.

Band	16cm	4cm	15mm	7mm	3mm
Frequency range (GHz)	1.1 - 3.1	3.9 - 11.0	16 - 25	30 - 50	83 - 105
Number of antennas	6	6	6	6	5
Number of baselines	15	15	15	15	10
Primary beam	42’ - 15’	12’ - 4’	2’	70”	30”
System temperature (K)	45	36	60	112	724
Centre frequency assumed below (GHz)	2.1	7.0	17.0	40.0	95.0
RMS noise (mJy/beam) (10 min)	0.04	0.03	0.05	0.09	0.70

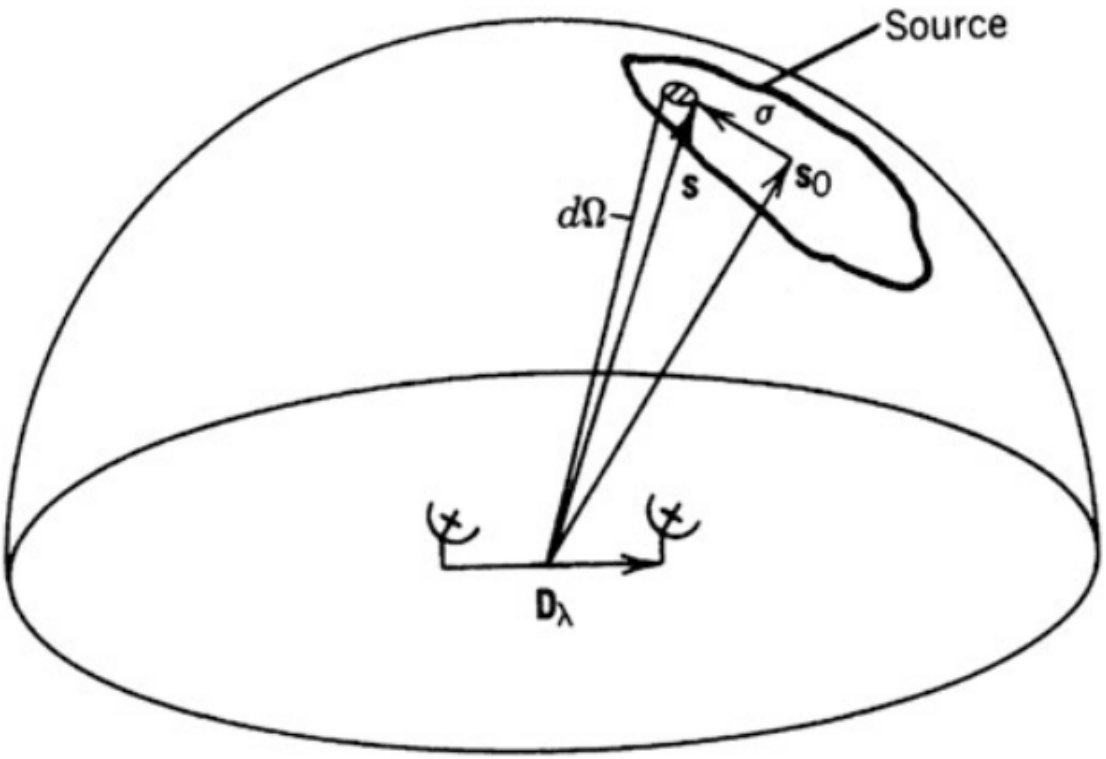

Figure 1.3: Representation of two antennas tracking a source with position vectors and baseline. The source is the outline on the celestial sphere. Credit: Thompson et al. (2017)

1.2.1.2 Relation between intensity and visibility

Thompson et al. (2017) give a detailed explanation of the relationship involving intensity and visibility through the use of the Fourier transform. In this subsection I report a brief description but see Thompson et al. (2017) for a more exhaustive description of the topic. Let us consider the antennas tracking a source as shown in Fig.1.3 where the unit vector $\hat{s_0}$ indicates the phase reference position which is the centre position of the source. Every element of the source is indicated by the vector $\vec{s}$ as $\vec{s} = \hat{s_0} + \vec{\sigma}$ where $\vec{\sigma}$ is the difference between the position of the element and the centre position. The two antennas have a baseline $\vec{D_\lambda}$ and every source element is under a solid angle $\mathrm{d}\vec{\Omega}$.

The following formula defines the complex visibility:

$$V = |V| e^{j\phi_v} = \int_{4\pi} A_N(\vec{\sigma}) I(\vec{\sigma})\, e^{-j2\pi \vec{D_\lambda}\cdot\vec{\sigma}} \mathrm{d}\Omega, \tag{1.1}$$

where $I(\sigma)$ is the source intensity distribution observed by the antennas and $A_N(\vec{\sigma}) =$

$A(\vec{\sigma})/A_0$. $A(\vec{\sigma})$ is the effective collecting area for each antenna, while A_0 is the antenna collecting area in the $\vec{s_0}$ direction. We can separate the imaginary and the real part:

$$\int_{4\pi} A_N(\vec{\sigma})I(\vec{\sigma})\ sin(2\pi\vec{D_\lambda}\cdot\vec{\omega})\ \mathrm{d}\Omega = -|V|sin\phi_v, \tag{1.2}$$

$$\int_{4\pi} A_N(\vec{\sigma})I(\vec{\sigma})\ cos(2\pi\vec{D_\lambda}\cdot\vec{\omega})\ \mathrm{d}\Omega = |V|cos\phi_v, \tag{1.3}$$

If we observed the ATCA from the point of view of the source, we would see the baselines tracing a plane as the Earth rotates. That is called the (u,v) plane. In Fig.1.4 there is a example of interferometer from Avison & George (2012) showing that increasing the number of antennas yields a better coverage of the (u,v) plane (2, 5, 10 and 50 from the top to the bottom).

Several different array configurations would be necessary to get the largest coverage of the (u,v) plane and ideally each configuration should be obervered for 12 hours. Nevertheless, it is not necessary to reach the complete coverage of the (u,v) plane to properly lead most scientific projects thanks to the snapshot imaging technique (Burgess & Hunstead, 1995). This strategy of observation consists of observing a source for a short time (roughly 5 minutes) before pointing to the next source. When the array has observed all the sources, the first source is observed again and the loop starts over. Burgess & Hunstead (1995) reported that the typical number of loops required is between 6 and 10. This is required, especially for arrays with a limited number of baselines such as ATCA. On the other hand, for radio telescopes with several baselines at different angles, one brief observation is enough for each source. The Very Large Array (VLA) is an example (Burgess & Hunstead, 1995).

In detail, we introduce a new coordinates system of which the geometry is shown in Fig. 1.5. The baseline has three components (u,v,w) where u and v are coordinates of a plane which is normal to the direction of the phase reference position. Note also that v is measured towards the north while u is measured towards the east. The component w is measured in the direction of $\vec{s_0}$ (the phase reference position). Using the Fourier transform the phase reference position becomes the origin of the derived intensity distribution $I(l,m)$. The coordinates l and m are direction cosines measured with respect to u and v. We can write the complex visibility as:

$$V(u,v,w) = \int_{-\infty}^{\infty}\int_{-\infty}^{\infty} A_N(l,m)I(l,m)\times\exp\left\{-j2\pi[ul+vm+w(\sqrt{1-l^2-m^2}-1)]\right\}\frac{\mathrm{d}l\,\mathrm{d}m}{\sqrt{1-l^2-m^2}}, \tag{1.4}$$

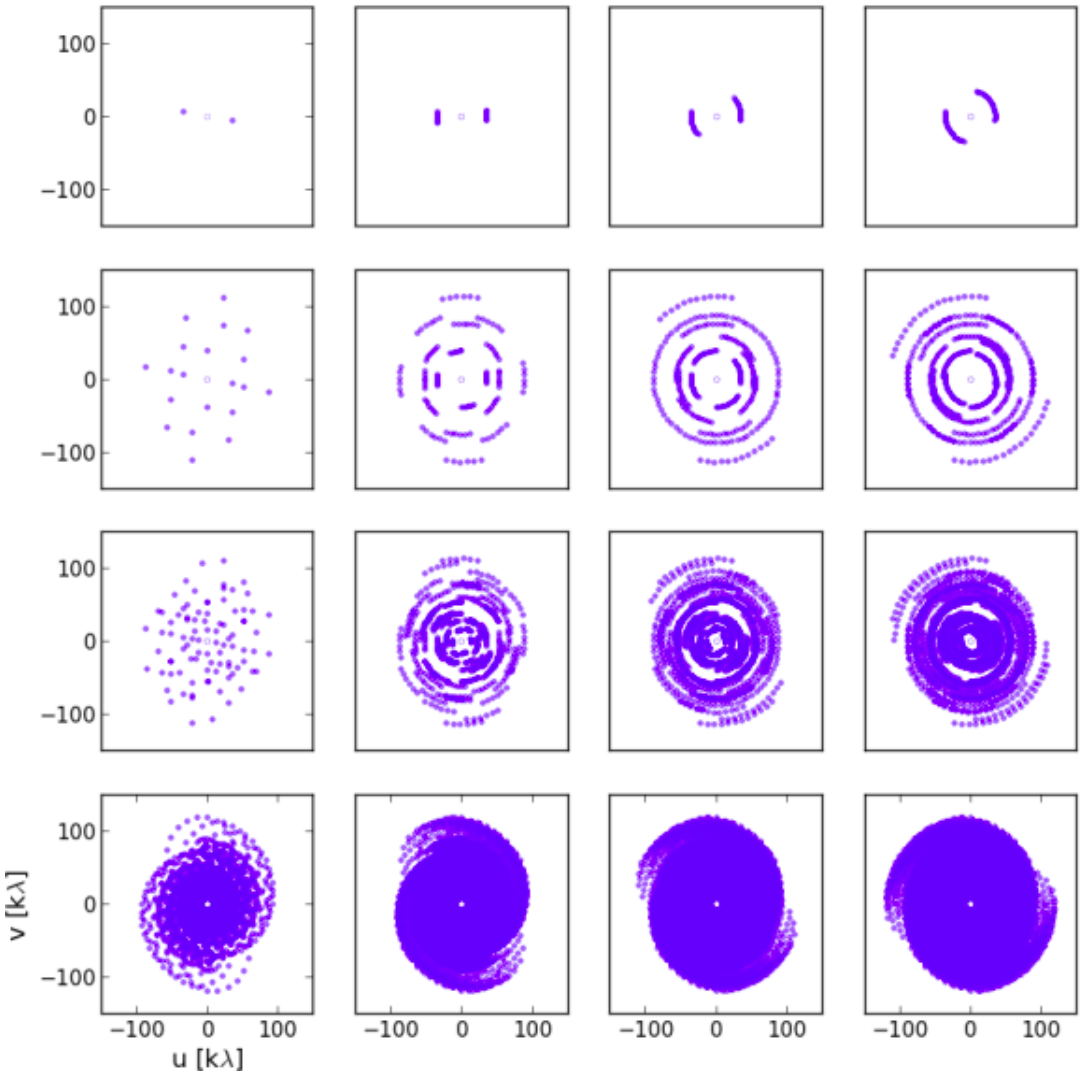

Figure 1.4: (u,v)-coverage of an interferometer set out in a logarithmic spiral pattern comprised of 2, 5, 10 and 5 antennas (top to bottom) and observing for 10 seconds, 2, 4, and 6 hours (left to right). Credit: Avison & George (2012).

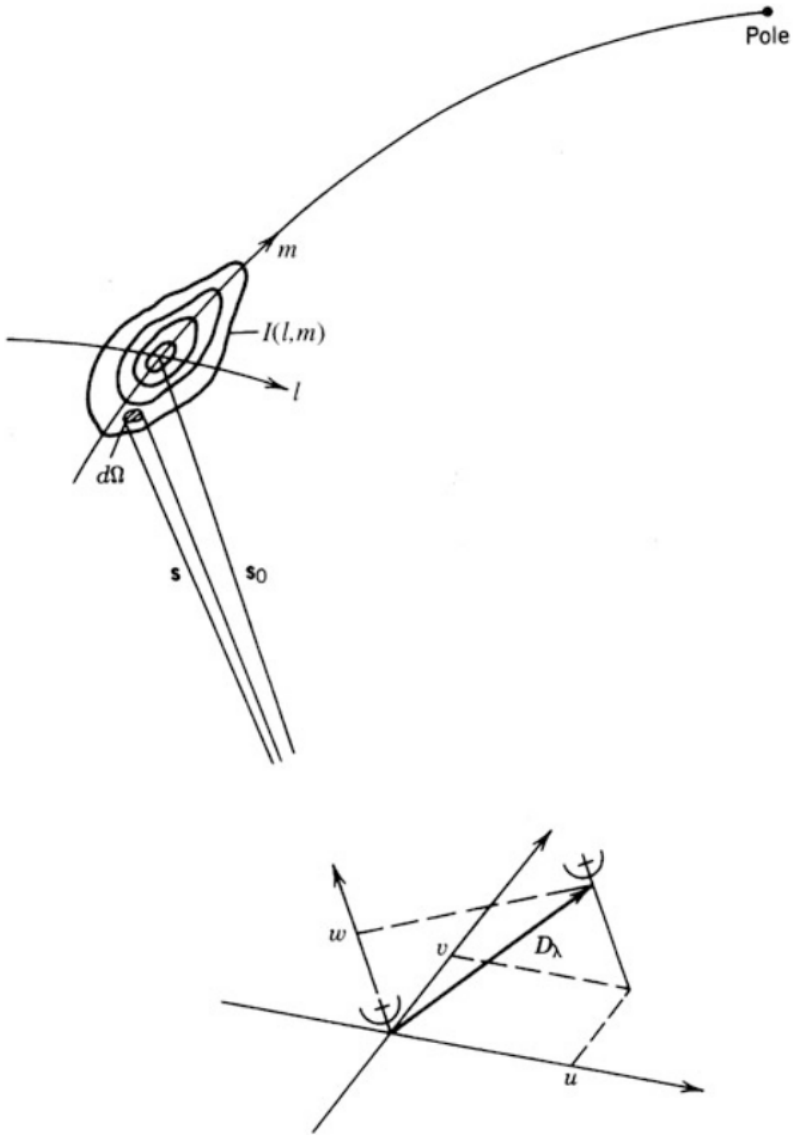

Figure 1.5: Geometry of a source with intensity $I(l,m)$ with an interferometer where the baseline vector has components (u,v,w). Credit: Thompson et al. (2017)

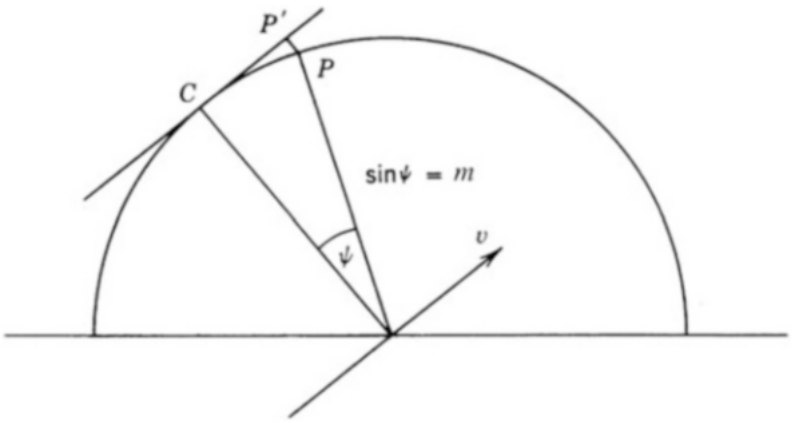

Figure 1.6: Mapping the celestial sphere onto one image plane in one dimension. The point C is the field centre. The position of the point P is estimated with the direction cosine m with respect to the v axis. The projection into a plane surface P appears in P' with a distance from C which is proportional to $sin\phi$. Credit: Thompson et al. (2017)

The coordinate system (l, m) is a projection of the celestial sphere onto a plane tangent at the field centre. A graphical explanation is in Fig. 1.6.

1.2.1.3 CABB correlator

As mentioned in Section 1.2.1.1 the signal goes to the feedhorns, then goes to the receivers which amplify the signal by 30−40 dB. The signal is then converted into the frequency range used by the Compact Array Broadband Backend (CABB) samplers. These work between 4 and 12GHz. Hence, the conversion into this signal is necessary for mm and 16cm observations while at 4cm conversions are not required.

The samplers divide the signal into a discrete-time sequence of values. Then, the signal is digitised and sent to the correlator which analyse the level of correlation between two signals coming from two different antennas. In general, radio waves from the same source arrive at different times on different antennas. This is the reason for which it is necessary to do a delay calibration before sending the signal to the correlator.

1.2.1.4 Interference

Radio Frequency Interference (RFI) is evident especially between 80 MHz and 2 GHz because of human activity. In general, RFI causes evident spikes in the radio spectrum and makes the detection of astronomical sources more difficult. Fig. 1.7 shows the behaviour of interference in the 16cm band. TVs, microwave ovens, navigation satellites

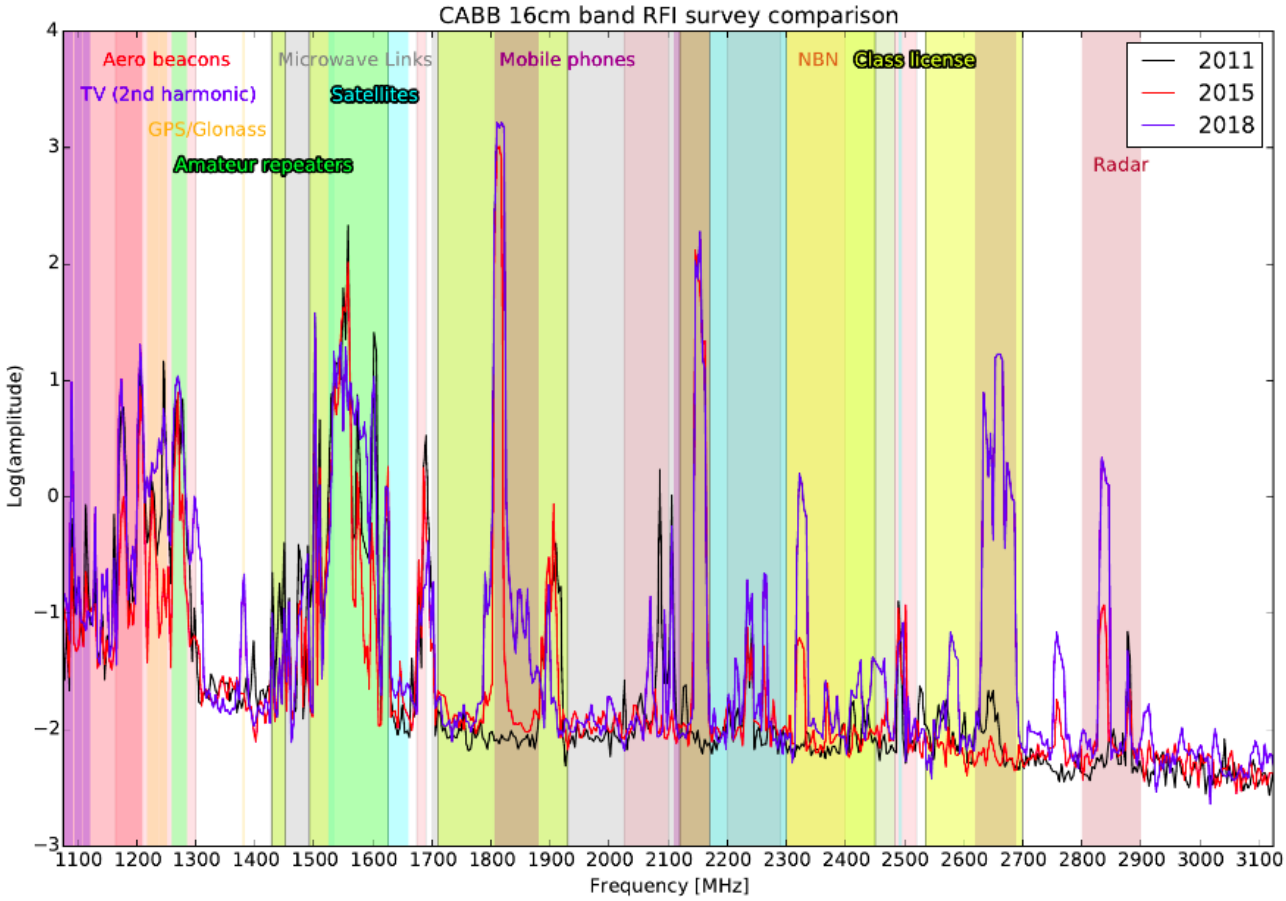

Figure 1.7: Radio spectrum of interference for the years 2011, 2015 and 2018 in the 16cm band from the ATCA User Guide. The different colours refer to different sources of the signal which are reported at the top of the graph.

are typical sources of this kind of interference. In this band it is also possible to observe "mid-week RFI" which presents high peaks in radio spectra at around 1265 and 1300-1310 MHz and may make the data unusable. It is important to specify that the mid-week RFI is local to ATCA and telescopes in more remote areas may not have an evident presence of this kind of RFI. The Australian Square Kilometre Array Pathfinder is an example (see Section 1.9). An RFI monitoring antenna located on the top the control building of the observatory, checks the presence of RFI once every 20s with 2MHz frequency resolution.

At 4cm the RFI strongly depends on the direction and can also be variable over time. RFI coming from satellites on the celestial equator, is supposed to be worse. At 7 and 3mm RFI is not evident while at 15mm RFI from the the Australian National Broadband

Network (NBN) satellite "Sky Muster" is detectable towards the celestial equator (see Fig. 1.8).

In general, radio telescopes need to be built in locations satisfying the following criteria:

- Being as far as possible from human-made electronics emitting radio waves.
- Being in a place which is as dry as possible if operating at certain frequencies (e.g., ATCA at 7 and 3mm).

Human-made electronics could interfere with the capability of radio telescopes of detecting faint radio sources. It can be necessary to operate at a dry location at high altitude because of the atmosphere. Indeed, moisture in our atmosphere can absorb waves at higher radio frequencies (especially at 7 and 3 mm for ATCA). Australia has been chosen (along South Africa) to host the Square Kilometre Array which will be the largest radio telescope in the World. The Murchison Radio-astronomy Observatory (MRO) located in the Australian desert satisfies the criteria listed above. RFI is getting worse in Eastern Australia due to presence of growing cities and population. The MRO is in Western Australia and precursors of the SKA are already in place. One of these is the Australian Square Kilometre Array Pathfinder (ASKAP).

1.2.2 The Australian Square Kilometre Array Pathfinder

The Australian Square Kilometre Array Pathfinder (ASKAP) is a precursor of the Square Kilometre Array (SKA) located at the Murchison Radio-astronomy Observatory (MRO). ASKAP is one of the first radio telescopes having the phased array feed (PAF) technology on a large scale (Hotan et al., 2021). Thanks to this technique it is possible to achieve an instantaneous field of view of 31 $\deg^2$ at 800 MHz which is an advantage over ATCA as the latter cannot reach this large FoV as it does not have the PAF technology. Another advantage that ASKAP has over ATCA is the location. RFI has been deteriorating on the East Coast of Australia because of the growing population in that area of the country. The MRO in Western Australia was chosen for ASKAP as it is in a isolated region and FRI free location. The South African MeerKat Radiotelescope (Jonas & MeerKAT Team 2016, Camilo et al. 2018) is another precursor of SKA located in an isolated region (90 Km outside the small Northern Cape town of Carnarvon). See Sections 1.2.1.4 and 1.2.2.2 for more details on RFI.

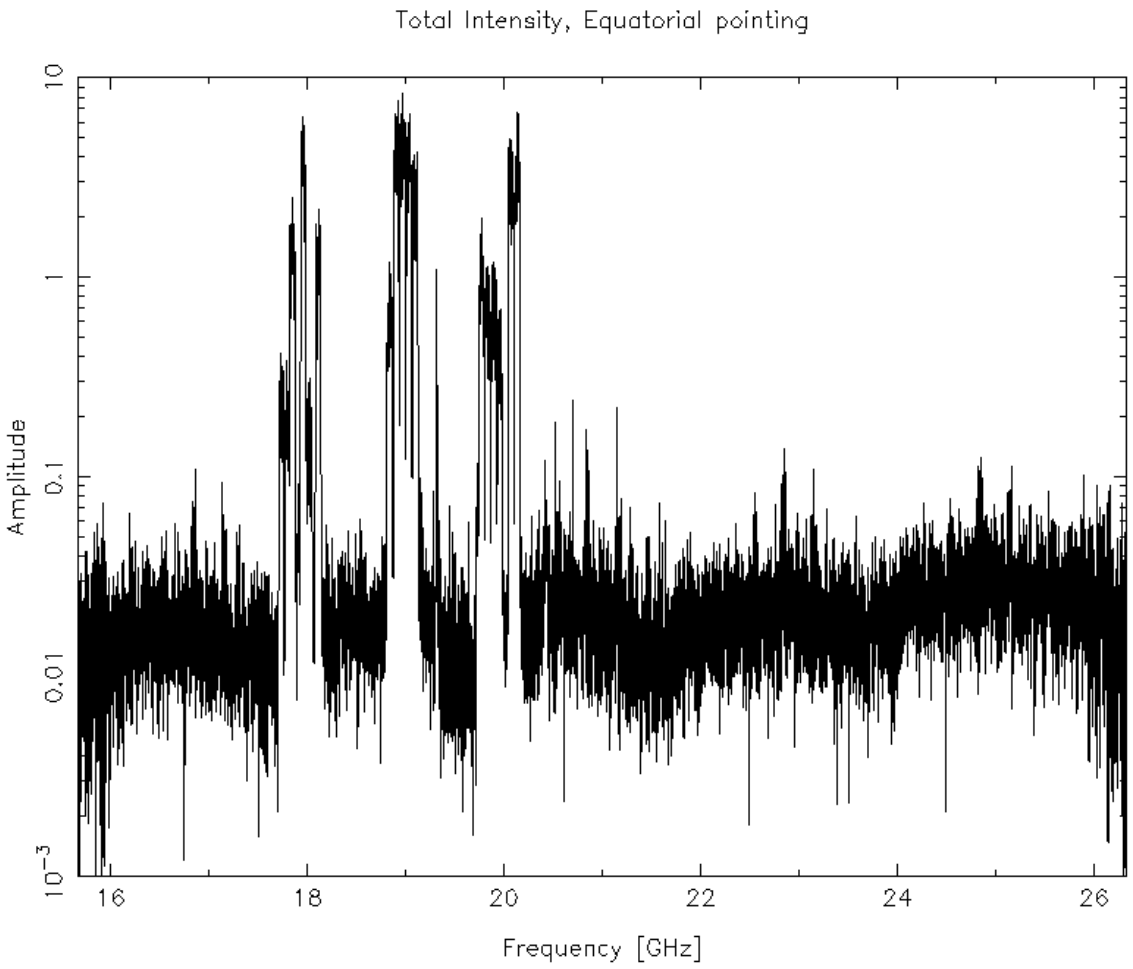

Figure 1.8: RFI in 15mm band from the ATCA User Guide. The interference is evident from the three high peaks.

In ASKAP each Phased Array Feed (PAF) is made up of 188 receivers which are connected to low-noise amplifiers to increase the amplitude of the weak radio waves. The PAFs generates 36 separate and simultaneous beams to obtain a large field of view. The array is comprised of 36 antennas with a diameter of 12m (see Fig. 1.9) and the baselines vary from 22m to 6 Km. The array has been fully operational since 2019.

1.2.2.1 Configuration and design of ASKAP

ASKAP takes advantage of the PAF receivers to get a large field of view (31 deg^2 at 800 MHz). This was the main goal of the array and allows astronomers to maximise the survey speed, which is the rate of observing a given sky area to a certain sensitivity (Johnston et al., 2007). The survey speed is defined by eq. 1.5 below:

Figure 1.9: The Australian Square Kilometre Array (ASKAP). Credit: Hotan et al. (2021).

$$SS = \left(\frac{A_e}{T_{sys}}\right)^2 \Omega_{FoV}, \tag{1.5}$$

where A_e is the effective area of the antenna, T_{sys} is the noise temperature of the system and Ω_{FoV} is the field of view. This definition of SS was given by Hotan et al. (2021).

In Table 1.2 the observing features of ASKAP are reported. The field of view dramatically decreases from 800MHz to 1700MHz. The sensitivity is 54 m^2/K for a beam close to the boresight (central pointing) and is defined as the system equivalent flux density (SEFD):

$$SEFD = \frac{2kT_{sys}}{\eta A}, \tag{1.6}$$

where η is the antenna efficiency, A is the physical area of reflector and k is the Boltzmann constant (1.38×10^{-23} J/K). The ratio T_{sys}/η is between 60K and 80K (η is the antenna efficiency). The T_{sys} is dominated by low-noise amplifier (LNA) noise. Hotan

Table 1.2: Observing features of ASKAP from Hotan et al. (2021).

Frequency range (GHz)	0.7 - 1.8
Number of antennas	36
Maximum baseline	6Km
Angular resolution	10" at 1GHz
System temperature (K)	75
Sensitivity	54 m^2/K
Field of view (800MHz)	31 deg^2
Field of view (1700MHz)	15 deg^2
Survey speed (800MHz)	91 400 m^4 deg^2 K^{-2}
Survey speed (1700MHz)	44 200 m^4 deg^2 K^{-2}

et al. (2021) state that the usage of more modern transistors in the future would improve the sensitivity.

The sensitivity can also be defined as the ratio between the effective area and the system temperature:

$$S(\Omega) = \frac{A_e}{T_{sys}}, \tag{1.7}$$

the sensitivity depends on the direction Ω within the field of view. In Fig. 1.10 there is a comparison between image noise and SEFD, demonstrating the dependence on the direction.

ASKAP includes 36 paraboloidal reflector antennas with a chequerboard PAF located at the primary focus. In each PAF, the radio signals are converted into digitised 1 MHz channels and sent over optical fibres to the central control building. The beamformers are the next step of the process, where 36 dual-polarisation are formed. The signal is subsequently sent to the correlator which collects the visibilities from all the baselines and process up to 15 552 channels for a maximum bandwidth of 288 MHz. Finally, the visibilities are sent to the Pawsey Super-computing Centre based in Perth. Using a custom software package called ASKAPsoft (Guzman et al., 2019) the visibilites are processed to produce images. The Pawsey Super-computing Centre manage a computer cluster with two compute processors (one with 10 cores and the other one with 8 cores), a processing power of 200 TeraFLOPS and a memory of 31.55 Terabytes. The machine is

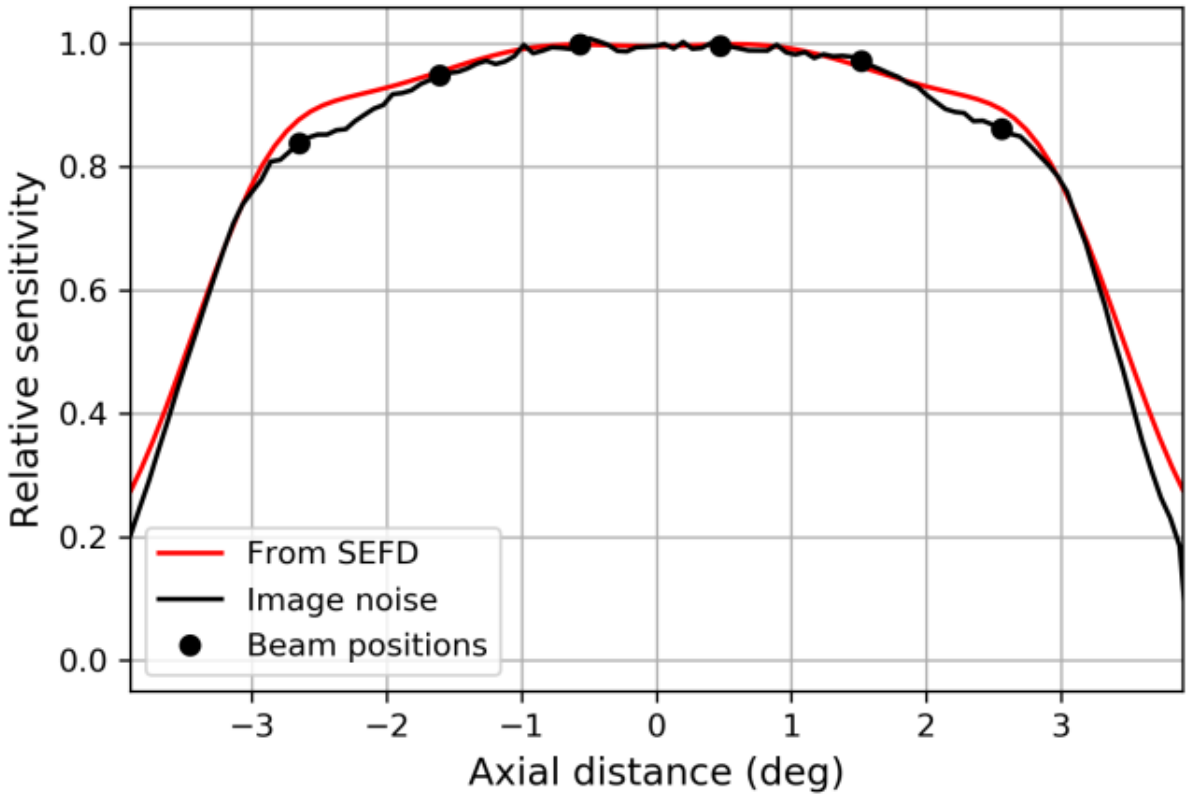

Figure 1.10: Sensitivity profile over the field of view of ASKAP. The data were obtained with a 1.05 deg beam pitch and a centered frequency of 888 MHz. Credit: Hotan et al. (2021).

called *Galaxy*[3] and is used for imaging ASKAP data. An overview of the ASKAP system is shown in Fig. 1.11.

1.2.2.2 Interference

ASKAP is located in an isolated area which is mostly radio quiet. Between 700 MHz and 1080 MHz persistent RFI is nearly absent. However, distant mobile communications could be a non-negligible RFI source depending on the atmospheric conditions. Fortunately, this kind of RFI can be predicted thanks to meteorological data (Indermuehle et al., 2018). The most common RFI is caused by satellites and aircraft. In particular, satellites are found to produce RFI between 1500 MHz and 1620 MHz, while aircrafts generate RFI mostly at 1090 MHz.

[3] https://pawsey.org.au/systems/galaxy/

1.2.2.3 ASKAP Survey Science Projects

During the first five years of ASKAP at least 75% of observation time will be used for survey science projects that were selected by an international panel in 2009. ASKAP is supposed to be fully operational in the current year of this thesis (2022). The projects were chosen based on scientific merit and feasibility. In 2019 a program of pilot surveys also started. This program has been crucial to demonstrate how ASKAP is suitable for providing interesting scientific results. The projects and their scientific goals are described below with a particular focus on the ASKAP Survey for Variables and Slow Transients (VAST, Murphy et al. 2013, Murphy et al. 2021) and the commensal role every ASKAP project can have.

An ASKAP Survey for Variables and Slow Transients (VAST)
The ASKAP Survey for Variables and Slow Transients (VAST, Murphy et al. 2013, Murphy et al. 2021) has the main target of studying radio transients and variables on timescales of 5 seconds to approximately 5 years. The central frequency of this survey is 888 MHz with a bandwidth of 288 MHz. The typical rms sensitivity at this frequency is 0.24 mJy/beam and the angular resolution is 12−20 arcsec, with a total sky area of 5131 deg^2.

Synchrotron transients (Metzger et al., 2015) are particular target sources for VAST. Examples of these are supernovae (SNe), tidal disruption events (TDEs), fast radio bursts (FRBs), gamma-ray bursts (GRBs). Interestingly, new classes of synchrotron transients have been observed (e.g. **AT2018cow**, Smartt et al. 2018). VAST investigates the origin of these events which in the rearly stages of observations can remain unclear (e.g. Prentice et al. 2018).

VAST is also probing two propagation effects which are extreme scattering events (ESEs) and scintillation. There is currently no satisfactory model describing ESEs (Bannister et al., 2016) and the origin of scattering plasma is still unclear. Thus, VAST will provide a large dataset of these events to probe their origin. In early observations with ASKAP, the discovery of five intra-day variability (IHV) variables in a 2 deg long line indicates a narrow plasma filament (Wang et al., 2021), which has highlighted the potential of VAST (and ASKAP) for studying the interstellar medium.

Other transients and variables are also VAST target sources including flare stars, neutron stars, pulsars and AGN. The latter will be discussed in detail later in this thesis (see Chapter 3).

The first release of VAST data is called the VAST Pilot Survey Phase I (VAST-P1,

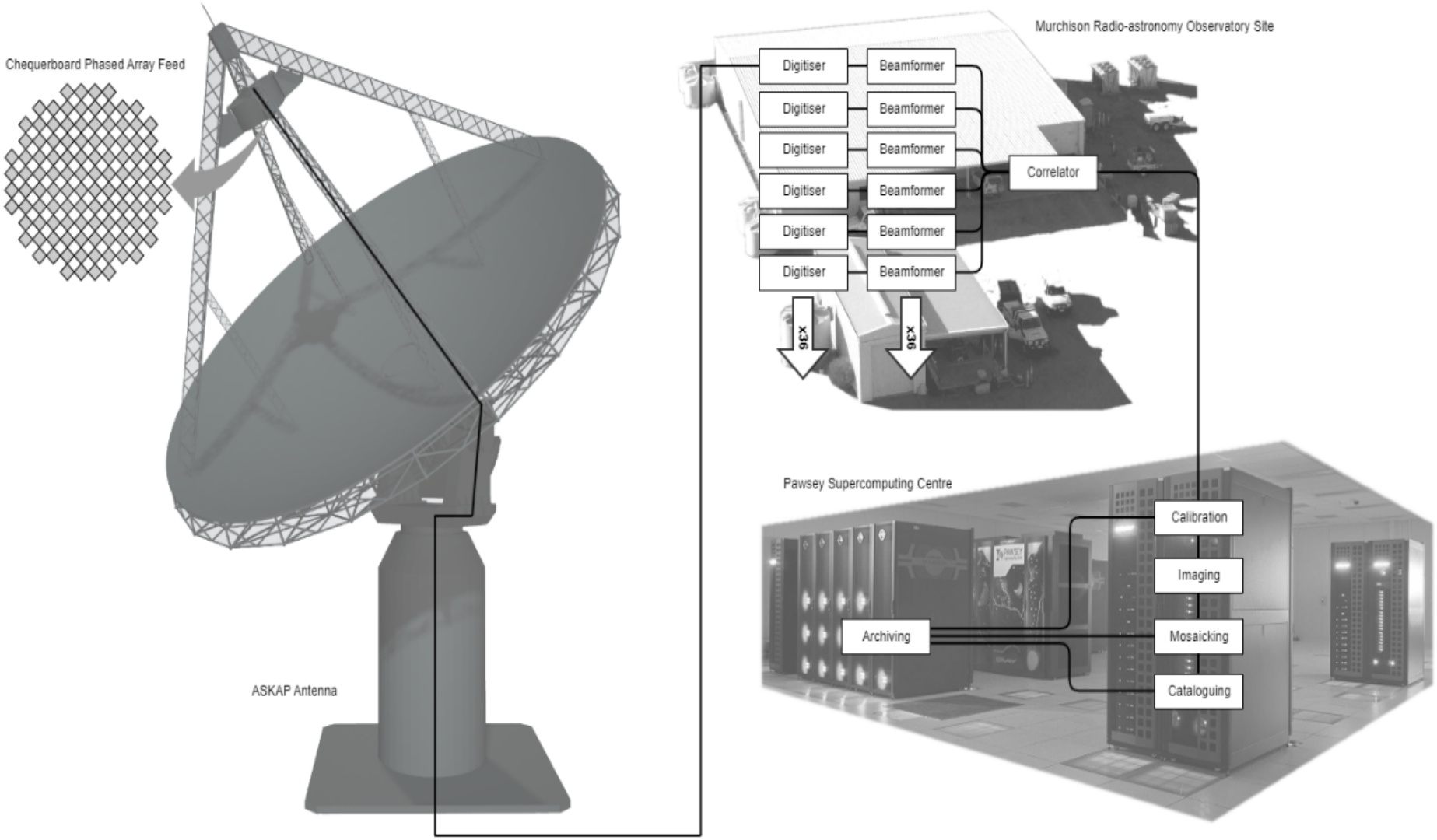

Figure 1.11: Overview of the ASKAP systems (Hotan et al., 2021).

Murphy et al. 2021). The pilot survey started in 2019 August and was completed in 2020 August. The VAST-P1 survey includes 13 epochs and there are a total of 113 fields. Each field is the combination of 36 beam images and was observed multiple times (with a cadence between 1 day and 8 months). The survey currently covers roughly 5000 $\deg^2$ but only five of the epochs have reached this sky coverage. The data are centred at 888 MHz with a bandwidth of 288 MHz. The rms sensitivity for a single epoch is typically 0.24 mJy beam^{-1} and the angular resolution is 12−20 arcsec. See Murphy et al. (2021) for information about the observation dates and number of fields. I have used VAST-P1 data to study variable AGN (see Chapter 3).

There is also a second release of the survey commenced in 2021 (Murphy et al., 2021). This second run is supposed to span for 6 months observing 5 epochs of the sky. Two epochs are to be observed in the same footprint of VAST-P1 at low frequency (centered at 888 MHz) while the other three epochs will be at higher frequency (centered at 1296 MHz) and will cover the Rapid ASKAP Continuum Survey (RACS, McConnell et al. 2020) footprint mid band survey. In Table 1.3 the observing capabilities of the two VAST releases are reported. The sky coverage of VAST-P1 and VAST-P2 is in Fig. 1.12 where we can see that part of the region 4 (VAST 4 in Fig. 1.12) is also covered by EMU survey (Norris et al., 2021). There is also overlapping with POSSUM (Gaensler et al., 2010) in the same sky area. This gives the possibility of having commensal surveys.

The Commensal Real-time ASKAP Fast Transients survey (CRAFT)

The Commensal Real-time ASKAP Fast Transients survey (CRAFT, Macquart et al. 2010) is a completely commensal survey designed to study fast radio transients (< 5s). Short-timescale transients allow to study matter in extreme physical conditions and there is a huge potential for scientific research. Highly-luminous Fast Radio Bursts (FRBs) are an example with their recent discovery (Lorimer et al., 2007). The survey covers the frequency range between 700 and 1500 MHz. At the moment of writing this thesis, the VAST Collaboration have been aiming to find out if the CRAFT COherent detector (CRACO) can be used for fast imaging.

Deep Investigations of Neutral Gas Origins (DINGO)

The Deep Investigations of Neutral Gas Origins (DINGO, Meyer 2009) survey was planned to study the evolution of neutral hydrogen (HI) from redshift $z = 0$ to $z \sim 0.4$. In detail, the goal is to learn about the evolution of the cosmic HI density in single galaxies. Therefore, the survey consists in 21 cm spectral line observations. DINGO also has the

Table 1.3: VAST observing capabilities. Some VAST-P2 parameters could be different when the survey is carried on. The VAST-P2 parameters which can change in future are the number of epochs, the minumum and maximum spacing and the image rms per epoch at 1296 MHz. These numbers are in italics. Credit: Murphy et al. (2021).

Parameter	VAST-P1	VAST-P2 (low)	VAST-P2 (mid)
Centre frequency	888 MHz	888 MHz	1296 MHz
Bandwidth	288 MHz	288 MHz	288 MHz
Integration per tile	12 min	12 min	12 min
Footprint	square6×6	square6×6	closepack36
Beam spacing	1.05 °	1.05 °	0.9 °
Total footprint area	5131 deg^2	5131^2	*2638 deg^2*
Number of epochs	5–13	*2*	*3*
Minimum spacing	1 day	*1 month*	*2 months*
Maximum spacing	12 months	*1 months*	*4 months*
Image rms per epoch	0.24 mJy beam^{-1}	0.24 mJy beam^{-1}	*0.2 mJy beam^{-1}*

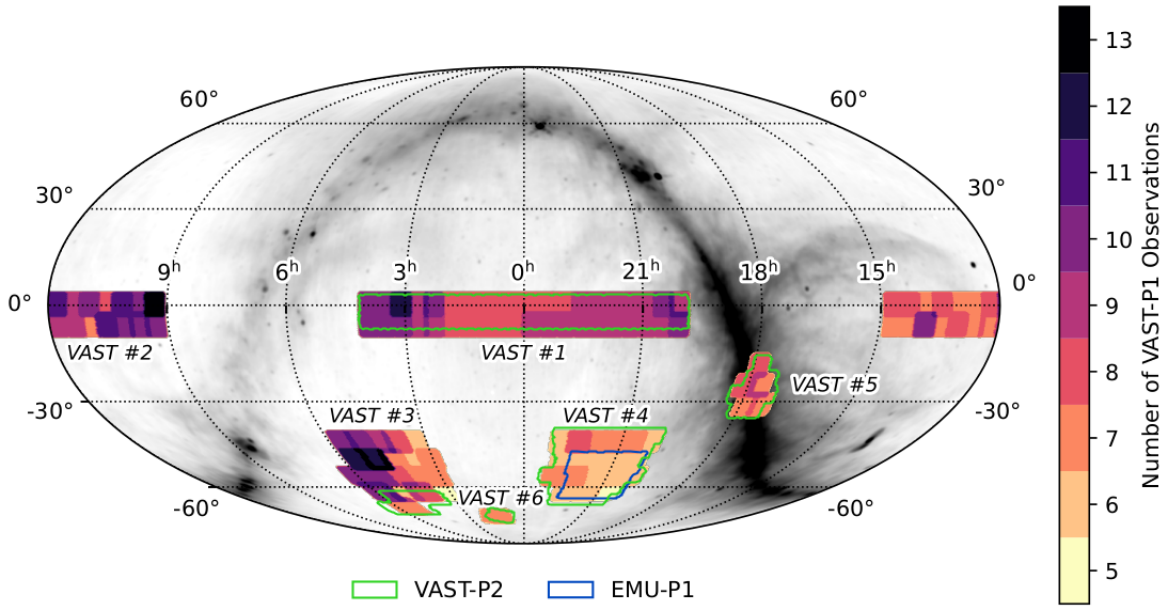

Figure 1.12: Footprint of VAST-P1 with the number of observations for each field. There is also the VAST-P2 mid-band footprint (green regions). The sky map is based on J2000 equatorial coordinates in the Mollweide projection. The background is based on diffuse Galactic emission at 887.5 MHz modelled by Price (2016) and Zheng et al. (2016). Credit: Murphy et al. (2021).

objective to study the evolution of galaxies over the last 4 Gyr. DINGO aims 400−800 hours observations of 6 fields which can be useful for commensal purposes with VAST.

Evolutionary Map of the Universe (EMU)

The main target of the Evolutionary Map of the Universe (EMU, Norris et al. 2011) is to examine the evolution of star forming galaxies and massive black holes. EMU is a deep continuum survey (rms ~ 10 mJy/beam) covering the entire Southern Sky and part of the Northern sky (declination +30 deg) at 1.3 GHz. EMU aims to study star forming galaxies up to $z = 2$, the evolution of massive black holes and their interaction with star forming galaxies, the Universe on large scales and the dark matter distribution. A remarkable discovery was made in 2020 with the observation of a new class of radio objects (Norris et al., 2021). These sources have a circular edge-brightened disc structure with about 1 arcmin diameter. The new objects have been named Odd Radio Circles (ORCs) and their formation process is currently unclear Norris et al. (2011). Commensal observations with VAST would allow to study radio variability from minutes to hours. This would be relevant especially for flaring stars and scintillation.

The First Large Absorption Survey in HI (FLASH)

The First Large Absorption Survey in HI (FLASH, Allison et al. 2021) is a blind neutral atomic hydrogen (HI) 21-cm absorption-line survey. The frequency range is between 711.5 and 999.5 MHz. The survey will cover the Southern sky of declination +40 deg with a redshift between $z = 0.4$ and $z = 1.0$. FLASH is designed to better characterise the properties of neutral cold gas and galaxies at cosmological distances observed in the radio continuum band. FLASH may be also useful to analyse star formation and the evolution of radio-loud AGN in their host galaxies. The 2 hours commensal observations with VAST would allow us to study transients and variables with timescales from minutes to hours (similarly to EMU).

The Galactic ASKAP Spectral Line Survey (GASKAP)

The Galactic ASKAP Spectral Line Survey (GASKAP, Dickey et al. 2013) is a high spectral resolution survey of the HI and OH lines in the Milky Way and Magellanic Systems. The survey will show the distribution of HI emission and absorption, molecular line thermal emission absorption, and maser lines. The survey was planned to cover the sky region below a declination of +40 deg including longitudes of 167 deg through 360 deg to 79 deg at $b = 0$ deg. The area of the Magellanic Stream and Clouds is also covered.

The total sky covered by this survey is 13 020 deg^2. The scientific goals of GASKAP are based on the narrow spectral channels and high brightness sensitivity of the survey to study galaxies evolution (Dickey et al., 2013). Commensal observations would be useful especially for the region of the Magellanic Clouds and the Galactic Centre. GASKAP indeed includes 200hr × 6 for the former and 50hr × 16 for the latter.

Polarization Sky Survey of the Universe's Magnetism (POSSUM)
The Polarization Sky Survey of the Universe's Magnetism (POSSUM, Gaensler et al. 2010) is a continuum polarisation survey of the whole sky south of +30 deg. It covers the frequency range between 1130 and 1430 MHz. The rms sensitivity is 10 μJy/beam at 10 arcsec resolution.

The survey was planned to estimate the Faraday rotation of three million extragalactic radio sources over 30 000 deg^2 and improve our knowledge of magnetic activity in the Universe. Commensal observations may taget radio variability between minutes and hours.

Widefield ASKAP L-Band Legacy All-Sky Blind Survey (WALLABY)
The Widefield ASKAP L-Band Legacy All-Sky Blind Survey (WALLABY, Koribalski et al. 2020) is a HI survey of the Local Universe. WALLABY is supposed to cover a large sky area ($-90° < \delta < 30°$) with a ~1.6 mJy/beam per 4 Km/s channel sensitivity. Importantly, WALLABY will provide the largest, most homogeneous HI sample of galaxies ever made.

The scientific targets of WALLABY are several. WALLABY will allow to trace gas-rich galaxies nearby the Local Group, analyse HI in galaxies, groups and clusters to better understand the relation between galaxy evolution and environment. Star formation correlated with HI will also be studied. The survey will also allow a refinement of cosmological parameters by analysing the spatial and redshift distribution of gas-rich galaxies. Commensal observations would allow to study variability from minutes to hours.

1.2.3 Swift Gamma Ray Burst Explorer

The Swift Gamma Ray Burst Explorer, commonly called *Swift*, is a multi-wavelength satellite (see Fig. 1.13) built with the target of observing gamma-ray bursts. The satellite takes advantage of the following capabilities described in Table 1.13.

The *Swift* observatory is comprised of three telescopes. Each of them operates in a different spectrum range. A brief description of each instrument is provided below.

Table 1.4: Observing capabilities of *Swift*

Spectrum coverage	gamma-ray, X-ray, UV, optical
Reaction time of the telescopes	<~90 s
Spectroscopy range	180−600 nm and 0.3−150 keV
position precision per GRB detection	0.5−5 arcsec

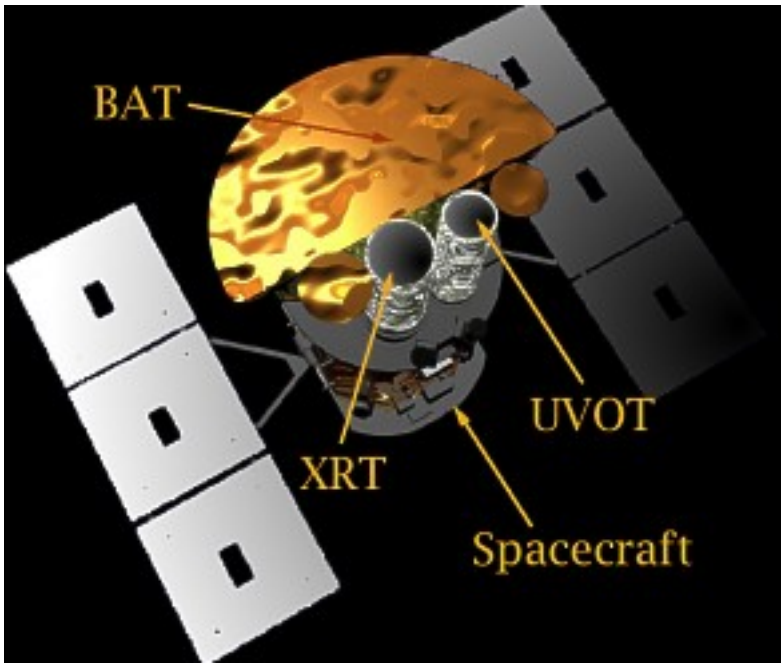

Figure 1.13: Graph of the *Swift* satellite with its components. Credit: *NASA*.

1.2.3.1 Burst Alert Telescope

The Burst Alert Telescope (BAT) operates in the energy range between 15 and 150 KeV and its field of view of 2 steradians. This large field of view was designed to efficiently detect GRBs and provide 4 arcsec localisation. The observing properties of BAT are shown in Table 1.5.

1.2.3.2 X-Ray Telescope

The X-ray-Ray Telescope (XRT) operates in energy range between 0.3 and 10 KeV and it was designed to measure fluxes, lightcurves and spectra of GRBs. This telescope provides GRBs positions with a 5 arcsec precision. The observing capabilities are in Table 1.6

Table 1.5: Observing capabilities of BAT.

Detecting Area	5200 cm^2
Detector operation	photon counting
Field of view	1.4 sr (partially coded)
Telescope PSF	17arcmin
Energy range	15−150 keV
Sensitivity	~10−8 erg cm^{-2} s^{-1}

Table 1.6: Observing capabilities of XRT.

Effective Area	110 cm^2 at 1.5 KeV
Detector operation	Imaging, Timing, and Photon-counting
Pixel scale	2.36 arcsec/pixel
Telescope PSF	18 arcsec at 1.5 keV
Energy range	0.3−10 keV
Sensitivity	8×10−14 erg cm^{-2} s^{-1} in 104 seconds

Table 1.7: Observing capabilities of UVOT.

Focal ratio	12.7
Detector operation	Photon-counting
Detection element	2048 x 2048 pixels
Telescope PSF	2.5 arcsec at 350 nm
Wavelength range	170-650 nm
Sensitivity	$B = 22.3$ in white light in 1000 s

1.2.3.3 UV/Optical Telescope

The UV/Optical Telescope (UVOT) has a wavelength range between 170 and 650 nm and a field of view of 17 x 17 arcmin. Optical afterglows typically decline in brightness ~$t^{-1.1}$ to $t^{-2.1}$ as reported on the National Aeronautics and Space Administration (NASA) website[4]. It is thus necessary to observe optical afterglow and measure their redshift with a rapid response mode (observe as soon as possible after detection at high energy). The observing features are in Table 1.7.

[4] https://swift.gsfc.nasa.gov/about_swift/uvot_desc.html

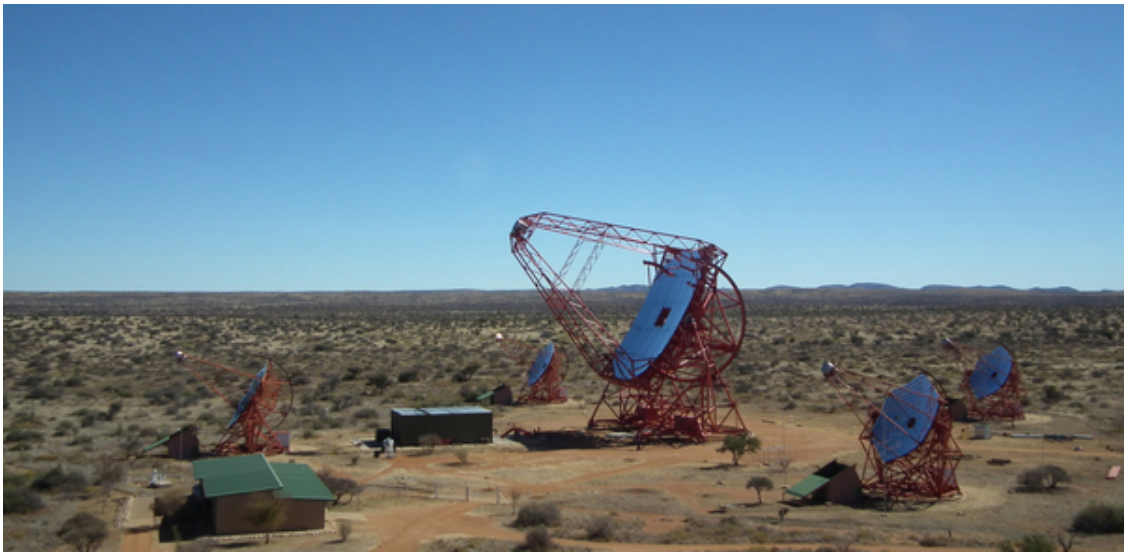

Figure 1.14: The High Energy Stereoscopic System. Credit: Credit: webpages of HESS.[5]

1.2.4 High Energy Stereoscopic System

The High Energy Stereoscopic System (HESS) is a system of Imaging Atmospheric Cherenkov Telescopes operating in the gamma-rays energy regime from 10s of GeV to 10s of TeV. It is currently the largest gamma-ray telescope in the world. This instrument is designed to investigate gamma-ray sources with flux intensity a few thousandths times the Crab nebula which is the brightest steady gamma-ray source in the whole sky. The array is composed of four 12 m-diameter antennas and a 28 m-diameter antenna.

The name HESS is also in memory of Victor Hess (Nobel Prize in 1936 for discovering of cosmic radiation). The telescopes system is located nearby the Gamsberg mountain, in Namibia (see Fig. 1.14). Observing capabilities of array are listed in Table 1.8

1.2.5 LIGO and Virgo detectors

The Laser Interferometer Gravitational-Wave Observatory (LIGO, Collaboration et al. 2015) and Virgo (Acernese et al., 2014) are Michelson interferometers (Michelson & Morley, 1887) built with the target of detecting and studying gravitational waves.

In a Michelson interferometer a laser beam is split into two beams thanks to a Beam-splitting mirror. Each beam is directed to a mirror and is reflected back to the Beam-splitting mirror. Here, the two beams are combined again. Because the phase difference between the two beams is 180°, they should cancel each other. However, in presence of gravitational waves the length of each arm (distance between mirror and

Table 1.8: Observing capabilities of HESS. H.E.S.S. II refers to the biggest antenna of the array while H.E.S.S. I to the other four antennas. Credit: webpages of HESS. [6]

	H.E.S.S. II	H.E.S.S. I
Focal length	36 m	15 m
Mirror area	614 m^2	108 m^2
Field of view	3.2 deg	5.0 deg
Image recording rate	3600 images per second	500 images per second
Pixel size	0.067 deg	0.16 deg
Energy threshold	0.16 TeV (zenith)	0.16 TeV (zenith)
Energy range	10s of GeV to 10s of TeV	10s of GeV to 10s of TeV

Beam-splitting mirror) changes over time. As a consequence, the phase difference is no longer 180° and the beams do not cancel each other. Light is hence observed by the light detector. This process is shown in Fig 1.15.

LIGO is the largest gravitational waves observatory in the World and is comprised of two interfermoters: one built in Hanford (Washington state, USA) and the other one built in Livingston (Lousiana, USA). The two interferometers are 3000 Km apart. Each LIGO interferometer has two 4 Km long arms adjusted in a "L" shape. Fig. 1.16 shows a photo of the two interferometers. Virgo is located in Cascina (Pisa, Italy) and this interferometer consists of two 3 Km long arms to form an "L" structure (likewise LIGO). Fig. 1.17 shows a photo of the interferomoter.

Because the distortion of the laser path could be due local events and not astronomical phenomena, it is necessary to have quasi-simultaneous detection in multiple interferometers. For instance, GW150914 was detected both by Virgo and LIGO (Abbott et al., 2016b). When it has been established that a gravitational waves source is detected, an algorithm (BAYESTAR, Singer & Price 2016) provides a map of the sky showing the probability density function of the source position.

Gravitational wave events can be classified as binary black hole mergers, binary neutron star mergers or black hole - neutron star mergers. This depends on the mass: $M > 5M_\odot$ for back holes, $M < 3M_\odot$ for neutron stars and $3M_\odot < M < 5M_\odot$ for "mass-gap event." An alert system is also used to communicate the detection of possible gravitational waves candidates. The system is the Gamma-ray Coordinates Network[8] (GCN).

[8] https://gcn.gsfc.nasa.gov/

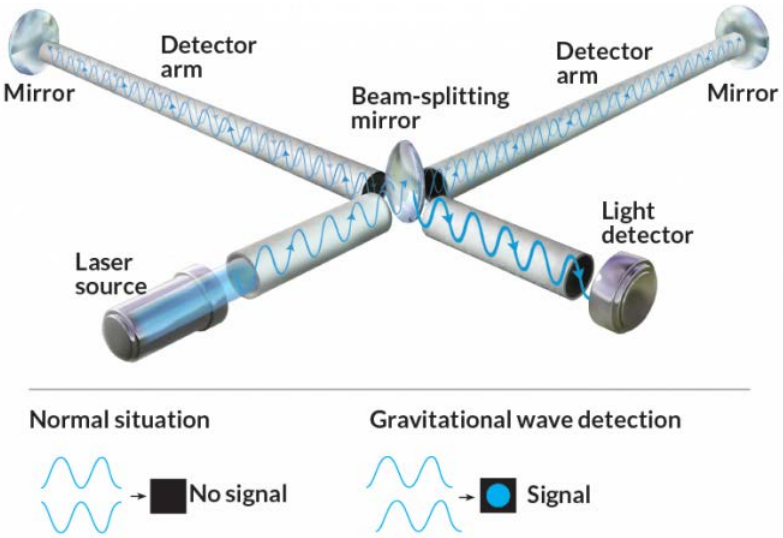

Figure 1.15: Simple graph explaining how a Michelson interferometer works. A laser beam is splitted in two beams though a Beam-splitting mirror. Each beam is directed to a mirror and then come back to the Beam-splitting mirror. Credit: ScienceNews [7]

Figure 1.16: The LIGO Hanford (left) and LIGO Livingston (right) interferometers.

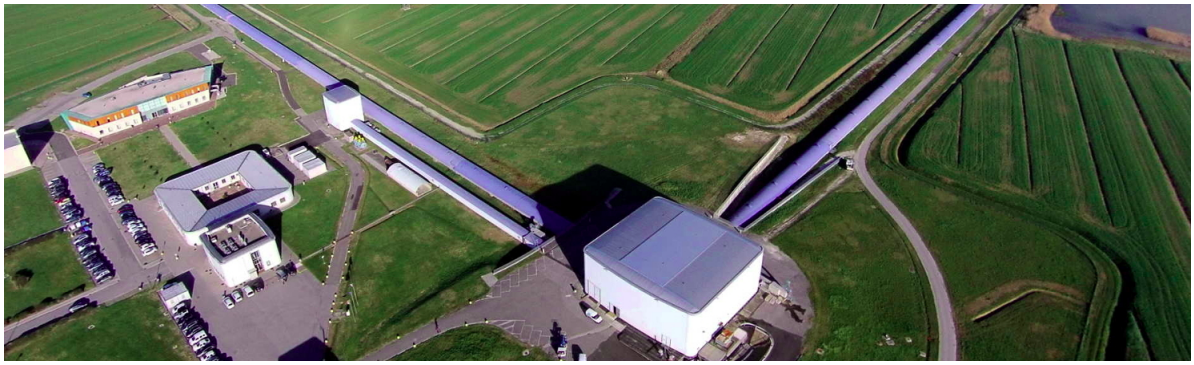

Figure 1.17: The Virgo interferometer.

1.3 Outline of science chapters: studying radio transients and variables

Each chapter contains a detailed and independent scientific introduction to the objects and observations contained within that chapter. The instrumentation described in the sections above provided the required data to perform the overall research in this PhD thesis. Below I outline each of the chapters and introduce the main astrophysical targets.

In Chapter 2 I use ATCA to study the behaviour of flare stars using the rapid response mode. Two particular flare stars were studied: AT Mic (Sasaki et al., 2019) and UV Ceti (Lynch et al., 2017) which are both M dwarf binaries. In general, rapidly rotating M dwarfs (dMe) have magnetic fields of the order of kilogauss (Johns-Krull & Valenti, 1996). This intense magnetic activity may cause stellar flares (Fender et al., 2014) and the radio emission may be proceeded by higher energy emission, which allows rapid radio response follow-up (e.g. on the timescale of hours). My work outlined three possible causes for the radio variability of UV Ceti and AT Mic: gyrosynchrotron radiation, electron cyclotron maser and plasma radiation (see Chapter 2).

In Chapter 2 ATCA observations were also used to study ultra-cool dwarfs. These are radio quiescent low-mass stars (0.08-0.45 solar masses) and brown dwarfs showing periodic polarised pulsations. Gyrosynchrotron emission of electrons could cause the quiescent activity (e.g., Ravi et al. 2011) whereas electron-cyclotron maser instability may be responsible for the pulsations (e.g, Williams et al. 2015b). Pineda et al. (2017) also report that there is a link between auroral processes typical of planets and brown dwarfs. Ultra-cool dwarfs are generally difficult to detect (Pineda et al., 2017). I hence adopted an innovative research method for detecting these objects which consists of

searching for fast rotating objects with photometric variability. At least 3 sources were detected using this strategy in the radio domain (see Chapter 2) .

Gamma-ray bursts (GBRs) are another class of transients I examined by using ATCA observations. GRBs are explosions which are caused by the implosion of massive stars, or collision of two compact objects (Berger, 2014). These sources generally present a dominant prompt gamma-ray emission. The collision of compact objects cause short GRBs (SGRBs), with a duration $t < 2s$, whereas massive stars are the progenitors of long GRBs (LGRBs) with $t > 2s$ (Berger, 2014). I focused my studies on the source grb190114C (Schulze et al., 2019) and concluded that the most likely cause of the radio variability of this source is scintillation (see Chapter 2).

In Chapter 3, I studied a sample of 30 variable active galactic nuclei (AGN) by using ASKAP and data from the VAST survey. Radio variability of AGN can be extrinsic or intrinsic, with extrinsic variability often being referred to as scintillation, which is caused by turbulence in an ionised medium such as the ionosphere, interplanetary, or interstellar plasma (Bell et al. 2014, Koay et al. 2019, Lazio et al. 2004). Intrinsic variability refers to several different phenomena such as shocks along relativistic jets (Blandford & Königl 1979, Hughes et al. 1985, Hovatta et al. 2008a), jet procession (Kudryavtseva et al., 2011), tidal disruption events (Kochanek 1994, Donnarumma et al. 2015) and a variable accretion rate (Shields & Wheeler 1978, Lin & Shields 1986). The analysis described in this chapter showed that scintillation is the most likely explanation for the radio variability of the variable AGN presented (see Chapter 3).

In Chapter 4 and 5 statistical models are applied to the light curve of the gravitational waves event GW170817 (Abbott et al. 2017a). This is the first gravitational waves event observable by traditional electromagnetic telescopes (Abbott et al. 2017a). The source was initially detected by LIGO and Virgo and then, by all the X and gamma-ray telescopes as well as the radio telescopes described in this Chapter (Abbott et al., 2017a).

In Chapter 4, I explain that the current method used in time domain astronomy for defining variables and transients using the modulation index and χ^2 test (see eq. 3.3 and eq. 3.4). These parameters describe the overall modulation and significance of variability in the time series, however, the ordering of the data is not taken into account. State Space Models (Tusell, 2008) can describe deeper properties in the time series (e.g. trend change, slope, rise or decline for a given time t) and I explore the usage of these models in time-series astrophysics. I show that State Space Models may be used for classifying transients by utilising feature extraction to classify the physical properties. In other words, these models could establish if a transient is a flare star, a gamma-ray burst, a

magnetar and so on. Finally, I show that these models could also be used for detecting transients hosted by another source e.g an active galaxy as explained in Chapter 5 and Keane et al. (2016).

Part I

Part I

CHAPTER 2

TRANSIENTS FOLLOW-UP WITH THE AUSTRALIA TELESCOPE COMPACT ARRAY

As discussed in Section 1.1, this thesis is a study of celestial sources through the lens of time domain astronomy. This is the analysis of how sources change and evolve over time, including the variation of the physical properties in astronomical objects such as supernovae, active galactic nuclei, black holes, neutron stars, gamma-ray bursts and fast radio bursts. Hence, a follow-up (post-explosion) with radio telescopes is crucial to understanding these phenomena which can be used as "laboratories" to probe the physics of matter in very extreme conditions (e.g. plasma under magnetic fields 100 times stronger than in our Sun).

In this chapter an analysis of radio transients carried out with the Australia Telescope Compact Array (ATCA) is reported. This work involved the study of:

- The gamma-ray burst grb190114c (Schulze et al., 2019).
- The flare stars AT Mic (Sasaki et al., 2019) and UV Ceti (Lynch et al., 2017).
- A multi-object campaign with the aim of detecting ultra-cool dwarfs.

My work consisted of managing the data reduction of telescope observations, production of light curves and scientific interpretation. This means to explain the physical phenomena causing radio variability in these objects. In detail, I state that the most likely explanation on the radio variability of the GRB at 5 and 9 GHz is scintillation.

I listed three possible physical processes for the variability of the UV Cet and AT Mic: gyrosynchrotron radiation, electron cyclotron maser and plasma radiation. Moreover, I detected at least 3 ultra-cool dwarfs. These sources were found to be fast rotators with photometric variability.

2.1 ATCA Rapid-Response and Monitoring Follow-up of TeV Gamma-ray Bursts

2.1.1 Gamma-ray bursts progenitors and classification

Gamma-ray bursts (GRBs) are explosions caused by the collision of two compact objects or the implosion of massive stars (Berger, 2014). Bromberg et al. (2013) also refer to these events as Collapsars (long) and non-Collapsars (short). A typical property of a GRB is a dominant and non-repeating prompt gamma-ray emission which can have a short or long duration. The collision of compact objects are the progenitor of short GRBs (SGRBs), with a duration $t < 2s$ while massive stars are the progenitors of long GRBs (LGRBs) with $t > 2s$ (Berger, 2014). SGRBs were also found to be gravitational waves progenitors (Abbott et al., 2017a). However, this separation between SGRBs and LGRBs, is not rigorous since there is a duration overlap between the two populations (Bromberg et al., 2013). Different instruments measure GRB durations in different energy bands. The 2s duration criteria was decided on a particular detector (BATSE) and for other instruments a different time duration may be more suitable. For instance, Bromberg et al. (2013) and Berger (2014) reported that for *Swift* the separation time is $t \sim 0.8s$. On the one hand, Bromberg et al. (2013) explain that there is a significant fraction of non-Collapsars which are longer than 10s, and there are also bursts detected by *Swift* that are shorter than 0.5s and have a non-negligible probability to be Collapsars. Classifying GRBs at high redshift (e.g. GRBs 080913 at $z = 6.7$ and 090423 at $z = 8.3$) involves another complication which is the cosmological time dilation. The two high redshft burst GRBs 080913 at $z = 6.7$ and 090423 at $z = 8.3$ are an example. Because of their duration they should be classified as LGRBs but their rest-frame time showed that these sources are actually SGRBs (Belczynski et al., 2010).

2.1.2 Gamma-ray emission

2.1.2.1 Prompt gamma-ray component

As mentioned in Section 2.1.1, GRBs present a prompt gamma-ray emission. GRB prompt emission light curves can show one dominant burst but can also be irregular and complex.

SGRBs and LGRBs show different properties. Ghirlanda et al. (2009) found that SGRBs have harder spectra than LGRBs because of a higher low energy spectral index ($\alpha_{short} = -0.4 \pm 0.5$, $\alpha_{long} = -0.92 \pm 0.42$) and a peak at higher energy ($E_{short} \sim 400$ keV, $E_{long} \sim 200$keV). In addition, there are no LGRBs detected at GeV and TeV energies while, at the moment of writing this work, only a few SGRBs were observed at this regime (Berger, 2014).

There are also similarities between SGRBs and LGRBs. For both the two populations there is an inverse correlation between the duration and intensity for single pulses (Norris et al. 2011, Berger 2014). Nakar & Piran (2002) showed that the variability timescales of SGRBs and LGRBs are similar in the first ~ 2s ($\delta t_{min}/T < 10^{-4} - 10^{-3}$ where δt_{min} is the minimum observed duration for a single pulse and T is the burst duration).

2.1.2.2 Extended gamma-ray component

A fraction of SGRBs show an extended gamma-ray component with a duration between 10 and 100s and softer than the prompt burst (Lazzati et al. 2001, Berger 2014). The incidence rate of SGRBs with this component is about 15% (Berger, 2014). In the literature there are several works trying to understand the cause of an extended emission. SGRBs could be originated by the formation of a rapidly rotating proto-magnetar, formed by a collapsed white dwarf, merger of a binary system of two white dwarfs or neutron stars (Metzger et al., 2008). The prompt peak could be due to accretion onto a central compact object and the extended emission could be caused by a relativistic wind that would slow down the magnetar. Another model suggests that the accretion of a collapsed neutron star generates the prompt emission and the interaction between the outflow and a non-degenerate companion would cause the extended emission (MacFadyen et al., 2005).

2.1.3 X-ray emission

GRBs have X-ray flares that, in general, quickly rise and decay with $\delta t/t << 1$ where δt is the duration of the flare and t is the time since the beginning of the burst (Berger, 2014). Margutti et al. (2011) found that the X-ray flare is correlated to the gamma-ray prompt emission in both SGRBs and LGRBs. Margutti et al. (2011) also claimed that X-ray flares are observed both in SGRBs with no extended emission and SGRBs with extended emission. It is possible that the X-ray flare is originated from the top of a weak gamma-ray component which is not detected. Late flares are also reported in the literature (Campana et al. 2006, Grupe et al. 2006, Malesani et al. 2007). Campana et al. (2006) analysed the afterglow of GRB 050724 and explained that there are flares and an extended emission following an initial spike. The first flare may be consistent with the model proposed by MacFadyen et al. (2005) indicating an interaction of the GRB outflow with a non-degenerate stellar companion. Nevertheless, the presence of more short duration ($\delta t_{min}/t < 1$) flares suggests that they are formed in a more compact region than the external shock. The most likely explanation is a delayed activity from the central engine.

2.1.4 Radio emission

The radio emission is mostly due to post-burst phenomena such as a dynamical ejecta and its shock with the circumstellar medium (CSM) as explained by Piran (1999). Sari & Piran (1999) and Anderson et al. (2014) also describe the presence of reverse-shocks. This component is dominant at early stages (within 24 hours post-burst) and become fainter in a few weeks when the forward shock component is dominant (Sari & Piran 1995, Resmi & Zhang 2016, Lamb & Kobayashi 2019). It is thought that the dynamical ejecta becomes detectable in a timescale of decades and would not depend on the shocks components but on its mass and velocity (Nakar & Piran 2011, Piran et al. 2013, Radice et al. 2018). The radiation processes accepted to explain the radio counterpart of GRBs is the synchrotron emission with a power-law spectrum including the three radio emission components described above (Granot & Sari, 2002).

2.1.5 GRB mechanism

From the explosion a jet is launched, causing a shock in the CSM as shown in Fig. 2.1. These shocks cause acceleration of electrons, resulting in synchrotron radiation. The accepted model is the forward-reverse shock scenario (Piran, 1999). For this model

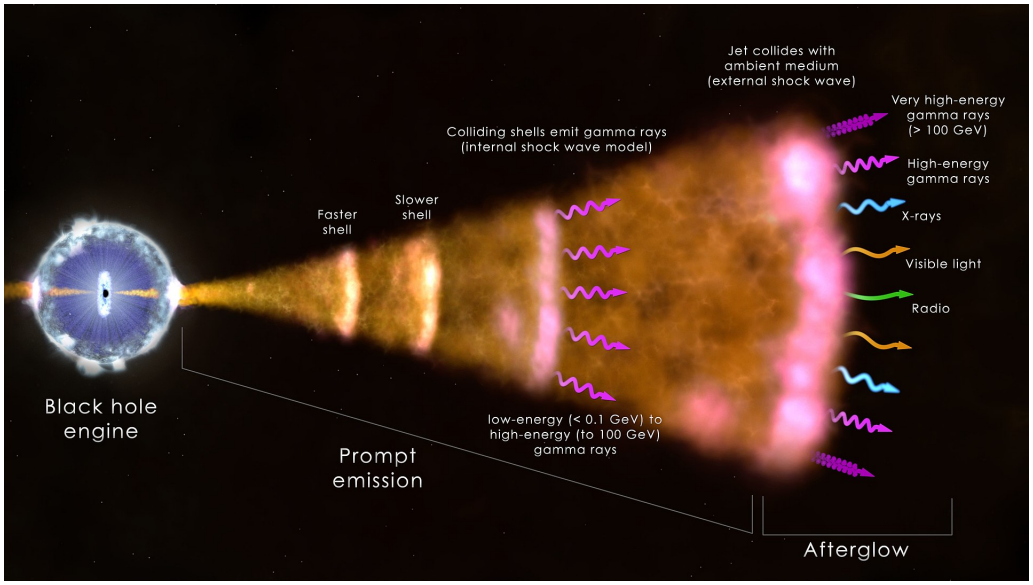

Figure 2.1: Representation of the GRB mechanism. (Credit: earthsky.org [1]).

forward shocks are generated by the jet moving towards the CSM, causing a radio afterglow. Moreover, reverse-shocks move towards the post-shock ejecta region, causing a radio/optical flare (Sari & Piran 1999, Anderson et al. 2014). GRB afterglows give rise to a power-law spectrum fitted with a synchrotron model with a maximum energy photon of 10 GeV at ~100s post-burst (Piran & Nakar, 2010). High energy emission is explained with the Synchrotron Self Compton model (SSC), considering the inverse Compton process (Sari & Esin, 2001).

The nature of the central engine is still unclear. Some models claim the formation of a hypermassive neutron star after the collision of two neutron stars (Hotokezaka et al. 2013, Rowlinson et al. 2013). This very compact object would subsequently collapse into a black hole (Murguia-Berthier et al., 2017) or turning into a magnetar (Bucciantini et al., 2012).

2.1.6 ATCA Rapid Response Mode

Since 2017, the ATCA has been able to search for transients right after a detection at high energies with the *Swift* satellite. When there is a detection of a GRB in the gamma-ray regime, ATCA can be triggered thanks to the Rapid Response Mode to search for a radio counterpart. It is possible to take advantage of this strategy in three centred wavelengths: 16 cm, 4 cm and 15 mm (from 1.1 to 25 GHz). The Rapid Response Mode uses theVOEvent Transport Protocol (VTP) which is the standardised system adopted to

report observations of transients and variable sources (Seaman et al. 2011; Swinbank 2014).

More information on the ATCA Rapid Response Mode is provided by Anderson et al. (2021) and the ATCA Users Guide[2].

2.1.7 The necessity of a rapid radio follow-up of GRBs with the ATCA

We required the ATCA rapid response to observe HESS-detected GRBs. For this study, ATCA is the most suitable radio instrument because of the wide frequency coverage, full polarisation capabilities and high sensitivity.

The TeV afterglow emission is dominated by the forward-shock component (Laskar et al., 2019). Hence, radio observations can allow for an analysis of the forward-shock synchrotron emission in the low energy regime. At radio frequencies, it is possible to study the spectral shape of the forward-shock component and get some physical properties of the source such as the strength of the magnetic field and the CSM structure and density.

This investigation allows us to address the difference between TeV-detected GRBs and non-TeV detected GRBs. In other terms, we still do not know why only some GRBs reach energies of the order of TeV. It is also possible that all GRBs present these high energies but TeV photons are not always detectable because the source is not enough bright.

It is thought that the inverse Compton process is responsible for the production of TeV photons (MAGIC Collaboration et al., 2019). The verification of this theory is another target of our GRB analysis.

2.1.8 Detection of GRB190114C

GRB 190114C is one of three bursts (the other two are GRBs 180720B and 190829A) detected in the GeV/TeV regime. The Major Atmospheric Gamma Imaging Cherenkov Telescopes (MAGIC) detected TeV photons from GRB190114C (MAGIC Collaboration et al., 2019). A radio observation of the GRB was performed within 24 hours post-burst. Early radio observations allow us to study the rise and peak of emission at different radio frequencies. This GRB is particularly interesting because of the very rare high energy emission range (0.2-1 TeV) reported by MAGIC Collaboration et al. (2019). This

[2] https://www.narrabri.atnf.csiro.au/observing/users_guide/html/atug.html#rapid-response-mode

energy range was theoretically possible but it is the first time it has also been detected (MAGIC Collaboration et al., 2019).

2.1.9 Radio observations and data reduction

The source GRB190114C was detected up to 177 days post-burst (from January 2019 to October 2019) with the ATCA. The Principal Investigator (PI) of the project was Dr. Gemma Anderson. The data were obtained using the CABB continuum mode (Wilson et al., 2011). I did the data reduction of 6 days of observations (see Table 2.1). For two observations at high frequency (at 43 and 45 GHz on 2019 January 27 and February 4) there was no evident detection. For these two observations I reported the flux density upper limits in Table 2.1. For all observations listed the flux density calibrator was PKS B1934-638 (Partridge et al., 2016) except for the observation performed on 2019 May 14, when PKS 0823-500 was used since PKS B1934-638 was not above the horizon. PKS B1934-638 was also used as bandpass calibrator for observations at 5 and 9 GHz. Because PKS B1934-638 is not bright enough at higher frequencies, PKS 1921-293 was our bandpass calibrator for observations at 17, 19, 43 and 45 GHz (see ATCA Users Guide). For all observations for which I reduced the data the phase calibrator was 0237-233 (RA = 02:40:08.17, Dec. = -23:09:15.7).

I reduced the data using the standard procedure available in MIRIAD (Sault et al., 1995). To get robust flux density upper limits at the position of the source, we used MFCLEAN to adopt a clean model of the sources in the field (manually drawing clean boxes). Subsequently, we subtracted this model from the visibilities. We estimated the flux density values using a model-fitting on the visibility planes (task UVFIT). We also did a model-fitting on the radio images with the CASA (McMullin et al., 2007) task IMFIT for a double check. The flux density errors are 1σ (rms and gaussian 1σ errors). We used these measurements to get the GRB light-curve (see Fig. 2.2).

2.1.10 Results and discussion

Propagation effects through the interstellar medium generate variations of the flux densities of compact sources (Rickett, 1990). This effect is called interstellar scintillation (ISS) and can affect GRBs with timescale between hours and days (e.g. Frail et al. 2000). There are two kind of ISS: strong and weak scintillation (Lazio et al., 2004). We expect to observe large flux density variations especially at low frequencies, while at higher frequencies this effect is supposed to be less evident (Lazio et al., 2004). In other terms,

Table 2.1: Radio observations of GRB190114C with the ATCA.

UT Date	ν [GHz]	Array configuration	Flux density [mJy]
2019 Jan 24	45	H75	0.95 ± 0.17
2019 Jan 25	5.5	H75	1.14 ± 0.04
2019 Jan 25	9	H75	1.4 ± 0.04
2019 Jan 25	17	H75	1.51 ± 0.05
2019 Jan 25	19	H75	1.33 ± 0.08
2019 Jan 25	43	H75	0.55 ± 0.07
2019 Jan 25	45	H75	0.55 ± 0.07
2019 Jan 27	5.5	H75	1.22 ± 0.09
2019 Jan 27	9	H75	1.35 ± 0.04
2019 Jan 27	17	H75	1.05 ± 0.09
2019 Jan 27	19	H75	1.06 ± 0.1
2019 Jan 27	43	H75	0.37 ± 0.05
2019 Jan 27	45	H75	0.14 ± 0.02
2019 Feb 4	5.5	H75	0.75 ± 0.06
2019 Feb 4	9	H75	0.82 ± 0.1
2019 Feb 4	17	H75	0.69 ± 0.05
2019 Feb 4	19	H75	0.67 ± 0.1
2019 Feb 4	43	H75	0.30 ± 0.09
2019 Feb 4	45	H75	0.11 ± 0.02
2019 Mar 27	5.5	6A	0.32 ± 0.01
2019 Mar 27	9	6A	0.18 ± 0.06
2019 May 14	5.5	1.5B	0.14 ± 0.01
2019 May 14	9	1.5B	0.13 ± 0.01

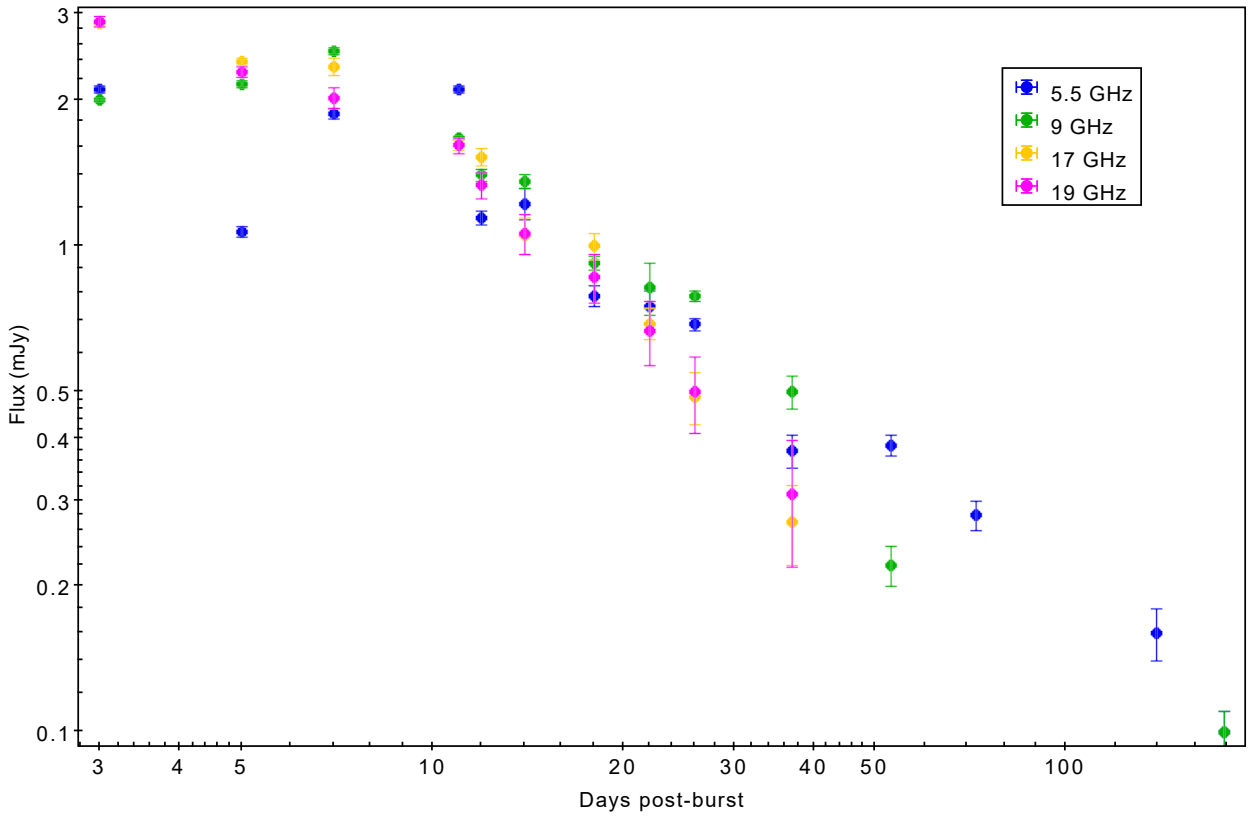

Figure 2.2: Light-curve of GRB190114C.

the data at 5 GHz and 9 GHz are expected to be more affected by ISS. The early drop of the light-curve at about 5 days post-burst suggests this interpretation (see Fig. 2.2). Misra et al. (2021) confirm this interpretation and suggest that GRB190114C show both strong and weak ISS.

Research which went beyond my work as a co-author was a multi-wavelength analysis of the afterglow that showed that this GRB is not consistent with the standard fireball model (Misra et al., 2021). A time evolution of shock microphysics is the most likely explanation. For this model the fractional energy content in non-thermal electrons and the magnetic field are not constant as suggested by the standard model, but change over time (see Misra et al. 2021 for a complete explanation).

2.2 ATCA Rapid response of flare stars

2.2.1 Introduction

Rapidly rotating M dwarfs (dMe) and tidally-locked RS Canum Venaticorum binaries (RS CVns; composed of evolved stars) show magnetic activity of the order of kilogauss (Johns-Krull & Valenti, 1996), which can cause stellar flares covering the whole electromagnetic spectrum. This is confirmed by Fender et al. (2014) that found a bright (~100 mJy) radio flare at 15 GHz from the stellar system DG CVn. The radio flare was observed 6 minutes after the gamma-ray flare was detected by *Swift*. The two flares systems I studied are M dwarfs binaries.

2.2.2 High energy emission

Bremsstrahlung radiation is emitted in hard X-rays (> 20 keV) when electrons and ion beams collide with the denser stellar chromosphere. The gas in the chromosphere is heated and there is emission of UV and optical radiation. The density and temperature of the newly formed coronal loops increase. This causes soft X-ray and extreme UV wavelengths emission. This is the scenario consistent with Mitra-Kraev et al. (2005). Audard et al. (2000) proposed that flares are the main cause of the heating in outer stellar atmospheres and in the case of quiescent activity stars would have undetected nano-flares.

The soft X-ray spectrum can also show the presence of the iron Kα emission line at 6.4 keV that can be explained as fluorescence of the photospheric iron and collisions of accelerated particles (Osten et al., 2010).

2.2.3 Radio emission

M dwarf radio emission below 5 GHz, is mostly due to coherent circularly polarised radiation caused by instabilities in the electron velocity distribution (Dulk 1985, Bastian et al. 1990, Melrose 2017) and auroral-type magnetic activity (Zic et al., 2019). Dulk (1985) showed that the coherent emission can be useful to examine the electron velocity distribution and the magnetic field. The radio emission is incoherent above 5 GHz and is caused by gyrosynchrotron radiation of mildly relativistic electrons (e.g. Zhang et al. 2018).

Giant radio flares lasting for a few hours vary in polarisation, spectral index and brightness on short timescales (from seconds to minutes) as discussed by Osten et al.

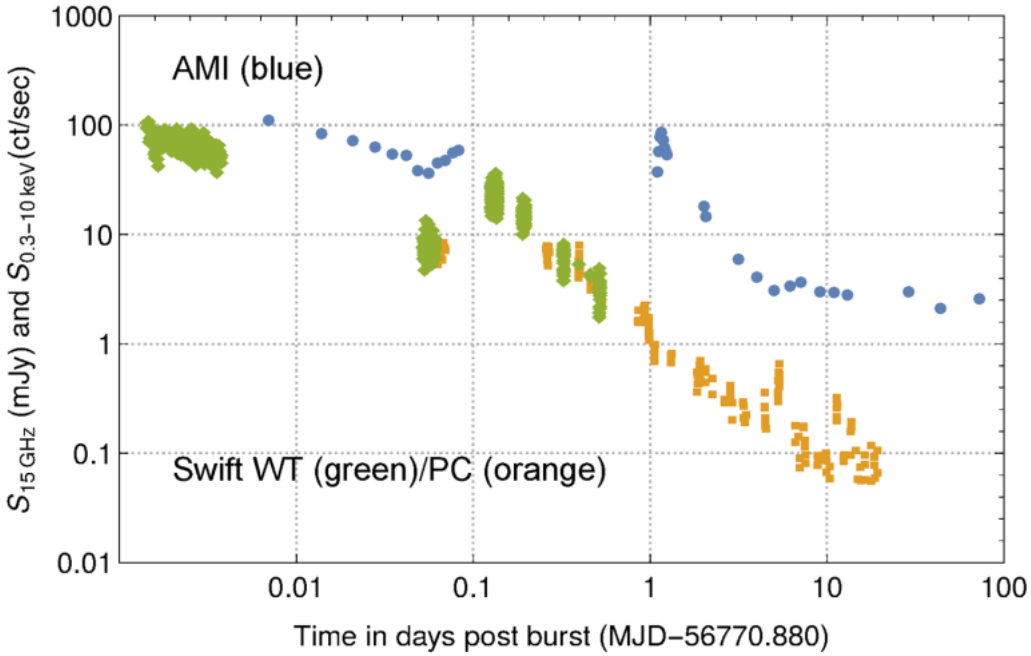

Figure 2.3: AMI-LA 13-18 GHz (blue circles) and Swift WT/PC (green diamonds/orange squares) 0.3-10 keV light curves on a logarithmic scale. For clarity, error bars are not plotted but for both radio and X-ray data are typically ≤15 per cent. In X-rays the source was brightest at the first measurement, two minutes after the initial trigger, and then declined for around the first hour, re-brightening somewhere between 0.075 and 0.125 d. The radio flux (in blue) behaved similarly, with a bright, strong detection in the first measurement at 6 min, followed by a decline and subsequent rebrightening. A second, clearly resolved, radio flare occurred at around 1.1 d. By about four days the radio flux had settled down to a quiescent level of a few mJy. Credit: Fender et al. (2014).

(2005). It is not possible to predict giant radio flares (Osten et al., 2005). Hence, it would be difficult to find these sources by monitoring the radio sky. A better strategy consists of monitoring the sky even at high energy. Fender et al. (2014) found that gyrosynchtron radio flares are associated with X-ray/gamma-ray flares using radio data from the Arcminute Microkelvin Imager Large Array (AMI-LA; Zwart et al. 2008) and high energy data from *Swift* (see Fig. 2.3).

2.2.4 The necessity of a rapid radio follow-up of flare stars with the ATCA

The early detection of a radio flare from DG CVn reported by Fender et al. (2014) is a demonstration of the correlation with a high energy flare and it is was the earliest radio detection of a high energy transient at the time of writing that paper. Fender et al. (2014)

also found that the radio emission varied on minute timescales. The radio detection was possible thanks to the Arcminute Microkelvin Imager Large Array (AMI, Zwart et al. 2008) rapid-response system. The AMI array has only a single polarisation regime available (I+Q) and a limited frequency range (14-18 GHz). Because of its wide frequency coverage and full polarisation, ATCA is the most suitable instrument for a rapid radio follow-up.

Rapid radio follow-up with the ATCA may be the key to find out the mechanism responsible for the accelerated electrons causing the high energy/radio flare. Not all bright incoherent radio flares have an X-ray counterpart (Osten et al., 2005). In Fig. 2.4 a light-curve of a radio flare is shown with an analysis of the circular polarisation on 5 minutes timescales. ATCA is able to do the monitoring activity on the same timescale and with two frequencies at once. This would allow to study the variability of the spectral index which is linked with the geometry of the emitting region, the magnetic field and the electrons population. Thus, we can compare these properties with radio flares with no high energy counterpart.

Rapid radio follow-up with the ATCA can also be a strategy to estimate the magnetic field and the distribution of the electrons. We need to observe the radio flare peak to probe the distribution of the electrons, the magnetic field and the kinetic energy (Dulk, 1985).

We can study the contribution of non-thermal energy. An estimation of the kinetic energy of the radio flare can set constrains on the X-ray emission. Osten et al. (2007) suggest a non-thermal X-ray emission while Osten et al. (2016) claim thermal radiation. Hence, this point is still under debate.

We know that X-ray/gamma-ray flares are associated with incoherent radio flares (e.g. Fender et al. 2014) but it is still unclear if coherent flares may also be linked with high energy flares. Rapid ATCA observations could find coherent flares and allow us to investigate the radiation mechanism which would be connected with high energy activity.

2.2.5 Detection of AT Mic and UV Ceti

The Monitor of All-sky X-ray Image (MAXI) detected an X-ray/gamma-ray flare from the M-dwarfs binary systems AT Mic and UV Ceti in January 2019. ATCA was triggered and radio observations started 1 hour post-flare for AT Mic and 13 hours post-flare for UV Ceti. The PI of the project was Dr. Gemma Anderson.

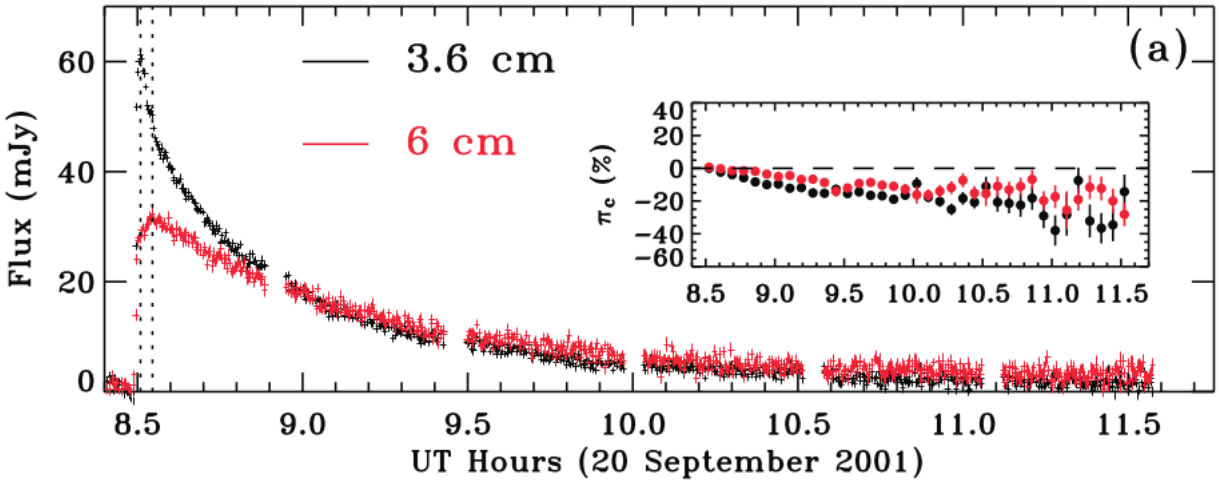

Figure 2.4: VLA light curve of a giant radio flare seen from the dMe EV Lac. Each tick corresponds to 10 s and the inset shows the variation in circular polarisation on 5 min timescales during the flare decay phase. Credit: Osten et al. (2005).

2.2.6 Radio observations and data reduction

I reduced data at 5.5 and 9 GHz in Stokes I and V (linear and circular polarisation, respectively) using the CABB continuum mode (Wilson et al., 2011). We had data available over two days of observations for each stellar system (see Table 2.2). I used the standard ATCA flux density calibrator PKS B1934-638 when it was not below the horizon. Otherwise, I adopted 0823-500 (see Table 2.2). The phase calibrator was different for each observation day (see Table 2.2). The data reduction technique was the same of the one adopted with GRB190114C using MIRIAD (see Section 2.1.9). However, this time I did not use the MIRIAD task UVFIT but the CASA task IMFIT to estimate the flux density values. I also run a code for producing light-curves which was provided by Dr. Jamie Stevens (ATNF scientist). The light-curves that I obtained are shown in Fig. 2.6 and 2.5 (linear polarisation). The data reduction process allows us to obtain radio images but not light curves. Short duration light curves are normally difficult to obtain with ATCA data. However, I was able to produce light curves thanks to coding scripts specifically created to analyse data from the Compact Array.

2.2.7 Results and discussion

The radio images show that we have detectable circularly polarised emission from AT Mic on 2019 January 15 at 5 and 9 GHz. However, we do not have a clear detection on January

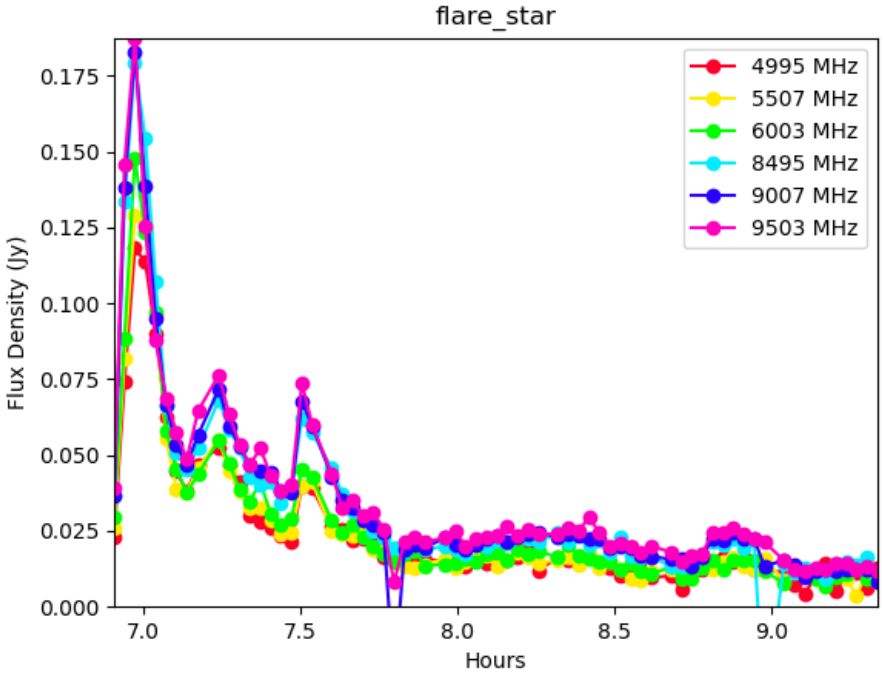

Figure 2.5: Light-curve of AT Mic in 4cm band

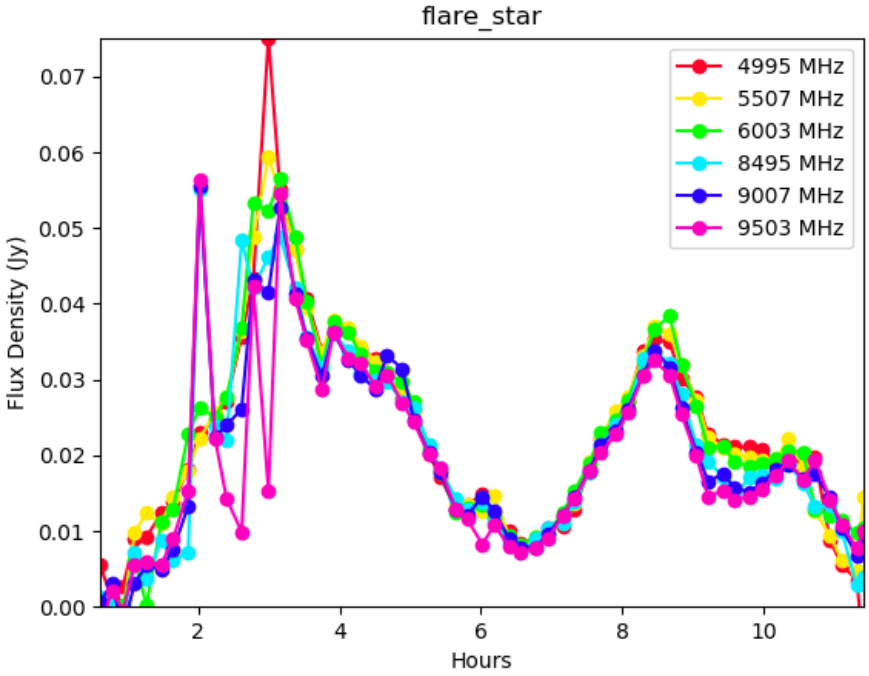

Figure 2.6: Light-curve of UV Ceti in the 4cm band.

Table 2.2: Radio observations of AT Mic and UV Ceti with the ATCA. The flux calibrator PKS B1934-638 is reported as 1934-638.

UT Date	ν [GHz]	Array configuration	Stokes	Stellar system	Flux calibrator	Phase calibrator
2019 Jan 12	5.5	1.5D	I	AT Mic	0823-500	2032-350
2019 Jan 12	5.5	1.5D	V	AT Mic	0823-500	2032-350
2019 Jan 12	9	1.5D	I	AT Mic	0823-500	2032-350
2019 Jan 12	9	1.5D	V	AT Mic	0823-500	2032-350
2019 Jan 15	5.5	1.5D	I	AT Mic	1934-638	2058-297
2019 Jan 15	5.5	1.5D	V	AT Mic	1934-638	2058-297
2019 Jan 15	9	1.5D	I	AT Mic	1934-638	2058-297
2019 Jan 15	9	1.5D	V	AT Mic	1934-638	2058-297
2019 Feb 12	5.5	H75	I	UV Ceti	1934-638	0130-171
2019 Feb 12	5.5	H75	V	UV Ceti	1934-638	0130-171
2019 Feb 12	9	H75	I	UV Ceti	1934-638	0130-171
2019 Feb 12	9	H75	V	UV Ceti	1934-638	0130-171
2019 Jun 29	5.5	750C	I	UV Ceti	0823-500	0114-211
2019 Jun 29	5.5	750C	V	UV Ceti	0823-500	0114-211
2019 Jan 29	9	750C	I	UV Ceti	0823-500	0114-211
2019 Jan 29	9	750C	V	UV Ceti	0823-500	0114-211

12. This means that the circularly polarised emission become observable three days post-burst. We also observed circular polarisation from UV Ceti (on February 12). Previous works (Dulk 1985, Bastian et al. 1990, Melrose 2017) showed that circularly polarised radiation is observed at lower frequency (below 5 GHz) and is coherent. Interestingly, we observed circular polarisation at higher frequency.

The flux density of AT Mic in Fig. 2.5 follows the same behaviour over time for all the frequencies with three peaks forming a unique triple flare structure peaking at ~0.175 Jy. The flare could be due to gyrosynchrotron radiation, electron cyclotron maser (Leto et al., 2016) or plasma radiation (Dulk, 1985). A similar discussion can be done for UV Ceti (Fig. 2.6). Nevertheless, the time series is different, with two flare structures. The early peak at 9 GHz could be due to RFI, considering the evident decoupling with the trend at 5 GHz. The flare activity of AT Mic lasts not more than one hour while UV Ceti is in the flare regime for ~10 hours. Probably, lower values of flux densities favour a

more efficient emission lasting for a longer time. Indeed, UV Ceti does not reach 0.08 Jy, while AT Mic is above 0.150 Jy. I will be a co-author of this work, and further analysis may more deeply explain these preliminary results.

2.3 Uncovering the population of radio ultra-cool dwarfs

2.3.1 Introduction

Low-mass stars (0.08-0.45 solar masses) and brown dwarfs show a radio quiescent activity interrupted by periodic polarised pulsations. The quiescent regime could be owing to gyrosynchrotron emission of electrons in plasma (Ravi et al. 2011, Williams et al. 2015a), while the pulsations may be due to electron-cyclotron maser instability (Hallinan et al. 2008, Williams et al. 2015b).

It is thought that the magnetic activity in early M-dwarfs is the same observed in the Sun, depending on the layer between radiating core and convective envelope. Through this layer of rotational energy would be converted into magnetic energy (e.g. Browning et al. 2006). This causes a link between angular momentum lost (through stellar wind) and magnetic field (Reiners & Mohanty 2012).

Brown dwarf are also associated with auroral processes typical of planets. Pineda et al. (2017) explain that in the solar system there are three kinds of auroral process: one due to the interaction between solar wind and planetary magnetosphere, one due to satellites moving within planets magnetosphere and another one due the the breakdown of co-rotation between rotating plasma disk and planetary magnetosphere. All these processes generate electrons beams and the acceleration of electrons causes electron cyclotron maser instability (ECMI).

The study of brown dwarfs spans from a planetary magnetic regime to a stellar magnetic regime. In detail, Morin et al. (2011) consider the possibility that magnetic activity of giant planets, low-mass stars and brown dwarfs could be similar.

2.3.2 Unresolved issues

In spite of the progress on understanding these sources, there are still unclear questions such as how the stellar magnetosphere is generated, how the plasma is generated, and how electrons reach the necessary energy to cause gyrosynchrotron emission. The

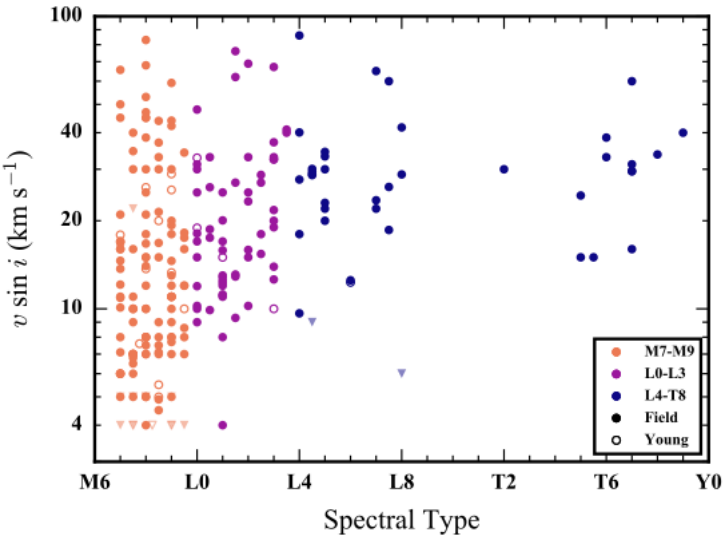

Figure 2.7: The collected literature detections and limits of UCD quiescent radio emission specific luminosity as presented by Pineda et al. (2017). Radio emission in Utra-cool dwarfs (UCD) is rare.

ongoing research suggests an internally driven magnetospheric engine and reconnection with the interstellar medium (e.g. Nichols et al. 2012, Pineda & Hallinan 2018).

Understanding the physics of these objects is a difficult challenge as very few sources (~25) have been discovered at the time of writing this thesis (Pineda et al., 2017). See also Fig. 2.7. More observations are needed to test the current theories and better understand these objects.

2.3.3 Method of investigation and initial results

Radio surveys with a limited volume have provided detection rates of only ~7-10% (e.g., Antonova et al. 2013; Route & Wolszczan 2016; Lynch et al. 2016), with recent detections bolstered by the strategy of Kao et al. (2016) which is based on searching for Hα emission or optical/IR variability. The problem of this technique is that in late-M and early-L dwarfs, there is a weak chromospheric emission with no correlation with electrodynamic process causing UCD radio emission (Pineda et al., 2017).

Our strategy has consisted on targeting UCDs with rapid rotation and photometric variability. The advantage of this approach is that these two properties are applicable to all UCDs and not only the coolest stars as happened for previous campaigns. Rapid rotation is consistent with current auroral electrodynamic models (e.g., Nichols et al. 2012). Furthermore, Pineda et al. (2017) and Shulyak et al. (2017) indicate that rapid ro-

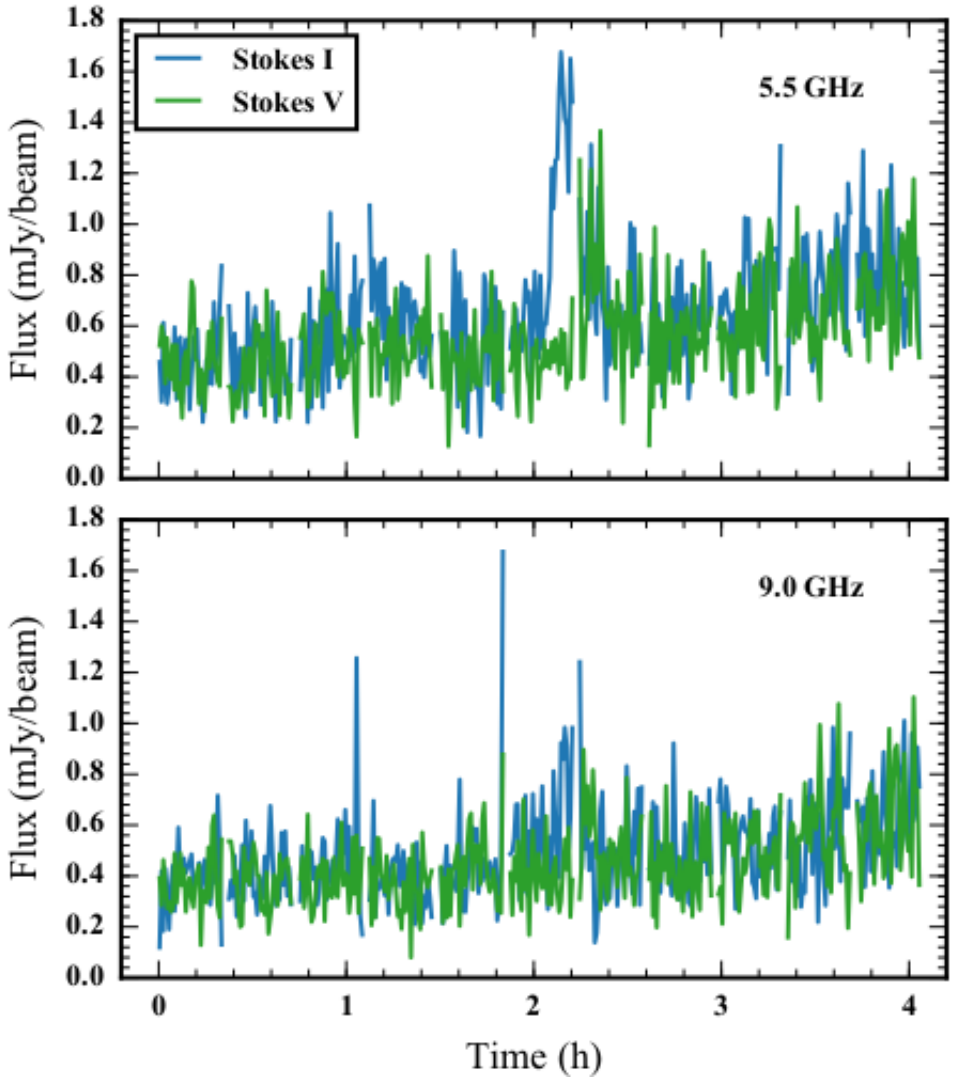

Figure 2.8: Top - Preliminary light curve in the 5.5 GHz band binned at 36s for ATCA test observations of J2228-4310, revealing bursts in Stokes V and Stokes I. Bottom - Same as top, but for the 9 GHz band, partly contaminated by RFI, and showing a spectral dependence to the polarized burst emission. Credit: Sebastian Pineda.

tation could be necessary for having a strong dipolar magnetic field. Harding et al. (2013) also found that radio UCDs have variability at optical wavelengths. Hence, searching for rapid rotating sources with photometric variability can be an efficient strategy to detect UCDs. This is confirmed by preliminary results obtained by the PI Dr. Sebastian Pineda (University of Colorado) who had already obtained one detection before I was involved in this project (see Fig. 2.8)

My role in the project has consisted of doing the data reduction and one of the

Table 2.3: Detection of ultracool dwarfs summary with name of the source, date of observation, and polarisation regime reporting 'yes' for detections and 'no' for non-detections.

		5.5 GHz		9 GHz	
Source	date of observation	Stokes I	Stokes V	Stokes I	Stokes V
j2228-4310	11-12/05/2019	yes	yes	yes	no
j2228-4310	3/06/2019	yes	no	yes	no
j1454-6604	3-4/09/2019	yes	yes	yes	yes
j0050-3322	13/09/2019	unclear	unclear	no	no

observations with the ATCA. Our strategy for detecting UCDs, allowed me to get 3 detections out of 11 observations with the ATCA (detection rate: 27%) triggering ATCA over 4 days of observation lasted at least 6.5 hours each. There is also an uncertain detection that might increase the number of detections to 4 (detection rate of 36%).

The detections are reported in Table 2.3. The two observations of J2228-4310 show an intense variability in circular polarisation (stokes V), since the detection for the first observation and the non-detection for the second one at 5.5 GHz. In detail, during the first observation there was stokes V detection at 5.5 GHz only. Hence, at high frequency (9 GHz) the ECM process is no longer able to produce radiation. Perhaps, at this frequency electrons have enough energy for penetrating to the surface of the star and not causing radio emission (Leto et al., 2016). j1454-6604 was detected at every frequency and polarisation regime. This demonstrates a correlation between linear and circular polarisation (stokes I and V, respectively). Whether a detection of j0050-3322 is confirmed the non-detection at 9 GHz will suggest the same behaviour of j2228-4310.

CHAPTER 3

RADIO VARIABILITY OF ACTIVE GALACTIC NUCLEI IN THE VAST PILOT SURVEY

3.1 Introduction

Active galactic nuclei (AGN) represent the largest population of varying radio sources, with timescales lasting from seconds to years (Hovatta et al. 2008b, Mooley et al. 2016, Sarbadhicary et al. 2020). Radio variability of AGN can be due to shocks along relativistic jets (Blandford & Königl 1979, Hughes et al. 1985, Hovatta et al. 2008a), jet procession (Kudryavtseva et al., 2011), tidal disruption events (Kochanek 1994, Donnarumma et al. 2015) and a variable accretion rate (Shields & Wheeler 1978, Lin & Shields 1986). Variability at radio frequencies can also be a result of scintillation. This can occur due to turbulence in an ionised medium such as the ionospheric, interplanetary, or interstellar plasma (Bell et al. 2014, Koay et al. 2019, Lazio et al. 2004). The early discovery of AGN radio variability via interstellar scintillation (ISS) was initially reported in a 408-MHz study by Hunstead (1972). They found four radio sources that showed high levels of variability; the mechanism of this variability was concluded to be scintillation. Observations at higher frequencies also showed that in the regime between 5 and 8 GHz the radio variability of AGN occurs on time-scales from hours to days and is mainly caused by scintillation in the ionised Galactic interstellar medium (Heeschen & Rickett 1987, Rickett 1990). For example, the Micro-Arcsecond Scintillation Induced Variability

(MASIV) survey at 5 GHz showed variation mostly due to Galactic scintillation (Lovell et al., 2003). The survey was composed of 443 compact flat-spectrum radio sources and 58 per cent of the sample was classified as variable in at least one of the first four observations (Lovell et al., 2008). In addition, Koay et al. (2018) reported that sources showing strong scintillation behaviour at 5 GHz (modulation index $m_5 > 0.02$) are also variable at 15 GHz (modulation index $m_{15} \geq 0.1$). The modulation index is defined in eq. 3.3. In this work we examine the variability properties of large numbers of sources around 1 GHz on the timescales of months.

AGN can also show variability across different frequencies of the electromagnetic spectrum (see Ulrich et al. 1997 and Padovani et al. 2017). At longer wavelengths, the variations in flux density become slower and the amplitude of the overall variability decreases (Kinney et al., 1991). As the central nucleus becomes brighter, the shape of the spectral energy distribution (SED) at UV–optical wavelengths is harder in radio-quiet AGN (Kinney et al., 1991), while in BL Lacs there is only a small change of the SED in the presence of flux density variations (Ulrich et al., 1997).

Under the AGN unification model there are different classes of AGN (Urry & Padovani, 1995). These classes are determined by the viewing angle, such as Seyfert galaxies, radio galaxies, blazars, quasi-stellar objects (QSOs) and low-ionisation nuclear emission-line regions (LINERs); see Urry & Padovani (1995) for more details. Blazars are divided into flat-spectrum radio quasars (FSRQs) and BL Lacs (Urry & Padovani, 1995). In BL Lacs the emission lines are weak in the optical spectrum (Stickel et al. 1991), while FSRQs show strong emission lines (Blandford et al., 2019a). In Seyfert galaxies, AGN are classified as type 1 and type 2. Type 1 Seyfert galaxies have broad and narrow lines in their optical spectra, while only narrow lines are present in type 2 Seyfert galaxies (Khachikian & Weedman, 1974). LINERs have been classified as AGN, since their low-ionisation emission lines could not be explained by star formation activity (Heckman, 1980). However, Ho et al. (1997), Eracleous et al. (2002), Stasińska et al. (2008) and McKernan et al. (2010) explained that the emission lines of LINERs cannot be triggered by AGN activity but instead by other phenomena such as thermal plasma, low-mass X-ray binaries or evolved stars.

The aim of this work was to probe a statistically robust sample of known AGN to identify the variability mechanism(s) at gigahertz frequencies. We also investigated the prevalence of variability as a function of AGN class. We used data from the Australia Square Kilometre Array Pathfinder (ASKAP, Hotan et al. 2021). In particular, we used data from the Variables and Slow Transients (VAST-P1) Phase I Pilot Survey (hereafter

VAST-P1, Murphy et al. 2013, Murphy et al. 2021) and the Rapid ASKAP Continuum Survey (RACS, McConnell et al. 2020), which provided the first epoch of this survey at 888 MHz. We used these data to analyse the radio variability in AGN with a targeted approach. We searched for radio counterparts to sources in four AGN catalogues. The catalogues that we used are the second release of the *Wide-Field Infrared Survey Explorer* (*WISE*) Blazar-like Radio-Loud Sources (WIBRaLS2) catalogue (D'Abrusco et al., 2019), the kernel density estimation (KDE)-selected BL Lac candidates (KDEBLLACS) catalogue (D'Abrusco et al., 2019), the Roma-BZCat catalogue (Massaro et al. 2015b) and the Véron catalogue (Véron-Cetty & Véron 2010).

3.2 Data

3.2.1 ASKAP Data

We analysed AGN sources from VAST-P1 and RACS. We describe these two surveys below.

3.2.1.1 VAST-P1

VAST-P1 (Murphy et al. 2021) is a radio survey performed by ASKAP. The survey started in 2019 August and was completed in 2020 August. The VAST-P1 survey includes 13 epochs, 12 of which were used for this work. There are a total of 113 fields. Each field is the combination of 36 beam images and was observed multiple times (with a cadence between 1 day and 8 months). The survey currently covers roughly 5000 deg^2 but only five of the epochs have reached this sky coverage. The data are centred at 888 MHz with a bandwidth of 288 MHz. The rms sensitivity for a single epoch is typically 0.24 mJy beam^{-1}. The angular resolution is 12−20 arcsec. See Murphy et al. (2021) for information about the observation dates and number of fields.

3.2.1.2 RACS

RACS (McConnell et al., 2020) is the first all-sky survey produced by all 36 antennas of ASKAP. The first survey release includes 903 radio images at low frequency (centred at 888 MHz with a bandwidth of 288 MHz) with a sky coverage of 34,240 deg^2 (for the sky south of a declination of +41°) and a resolution of ~ 15 arcsec. Every field was observed for ~15 minutes with a typical sensitivity of 0.25 mJy beam^{-1}. We included RACS as epoch 0 of VAST-P1.

3.2.2 AGN catalogues

We used four AGN catalogues and searched for the counterparts of these AGN in VAST-P1 and RACS. We describe the AGN catalogues below in further detail. One of the targets of this work is to probe potentially different variability characteristics among different classes of AGN. We therefore used the Véron catalogue (Véron-Cetty & Véron, 2010) which lists LINERs, quasars, Seyfert galaxies and BL Lacs. We also incorporated blazar catalogues to have more classes of AGN available because blazars are currently poorly studied at low radio frequencies (below 1 GHz) as reported by Giroletti et al. (2016a) and d'Antonio et al. (2019). We decided to use three blazar catalogues to have a large sample of blazars. We also searched for sources which were sufficiently compact (see Section 3.3), and blazars were suitable for this kind of selection since they are point-like objects.

We summarise the number of sources for each AGN catalogue in Table 3.1. Note that these AGN catalogues have sources in common (see Table 3.2). Hence, the total number of AGN in our sample is not the sum of sources listed in the catalogues.

3.2.2.1 The Véron catalogue

The Véron catalogue (Véron-Cetty & Véron, 2010) consists of 168 940 AGN in both the northern and the southern hemispheres (from a declination of $-86°$ to $+88°$). The current version (13th edition) lists 133 336 quasars, 1 374 BL Lac objects and 34 231 active galaxies. The objects classified as active galaxies include Seyfert 1, Seyfert 2 and LINERs fainter than an absolute B-band magnitude (wavelength $\lambda \sim 450$nm) $M_B > -22.25$. There are also 167 galaxies with a nuclear ionised hydrogen (H II) region. These sources were historically classified as AGN and remained in the catalogue. For each source, a redshift and M_B are reported.

3.2.2.2 The Roma–BZCat catalogue

Roma–BZCat is a multi-frequency catalogue of blazars (Massaro et al., 2015a). A wide range of the spectrum has been covered (radio, millimetre, optical, X-rays, and gamma rays). The catalogue reports coordinates, redshifts and multi-frequency data for 3561 sources. The sample is composed of 1909 FSRQs, 227 blazar candidates unidentified (BCU), and 1059 BL Lacs.

Table 3.1: The AGN catalogues used in this study, including the total number of sources per catalogue and the number of AGN for each class: FSRQs, BCUs, BL Lacs, QSOs and active galaxies. The class 'Active galaxies' contains Seyfert galaxies, LINERs and galaxies with nuclear H II regions.

Catalogues	Total sources	FSRQs	BCUs	BL Lacs	QSOs	Active galaxies
BZCat	3561	1909	227	1059	0	0
WIBRaLS2	9541	5089	3744	708	0	0
KDEBLLACS	5579	0	0	5579	0	0
Véron	168 940	0	0	1374	133 336	34 231

3.2.2.3 The second release of the *WISE* Blazar-like Radio-Loud Sources (WIBRaLS2) catalogue

The second release of the *WISE* Blazar-like Radio-Loud Sources (WIBRaLS2, D'Abrusco et al. 2019) contains 9541 radio-loud blazars selected from *WISE* (Wright et al., 2010). The catalogue reports information about the *WISE* colours, radio counterparts and coordinates. The sources listed are 5089 FSRQs, 3744 BL Lacs and 708 BCUs with no optical spectra available. The number of BL Lacs is much lower than the number of FSRQs because BL Lacs are often not detected in the mid-infrared *WISE* regime. For this reason, D'Abrusco et al. (2019) combined this catalogue with another one listing BL Lacs detected by *WISE*: the Kernel Density Estimation (KDE)-selected BL Lac candidates (KDEBLLACS) catalogue.

3.2.2.4 The KDE-selected BL Lac candidates (KDEBLLACS) catalogue

The KDE-selected BL Lac candidates (KDEBLLACS, D'Abrusco et al. 2019) catalogue lists 5579 BL Lac candidates selected from *WISE*. Information about the *WISE* colours, radio counterparts and coordinates are also reported. WIBRaLS2 blazars are selected from all four passbands (3.4, 4.6, 12, and 22μm) of *WISE*, while KDEBLLACS sources are selected from the sample of *WISE* objects detected in the first three *WISE* passbands only (3.4, 4.6 and 12 μm). D'Abrusco et al. (2019) used this technique to identify a larger number of BL Lacs (see D'Abrusco et al. 2019 for more information about the selection process).

Table 3.2: This table shows the sources in common among the AGN catalogues. Each number indicates how many sources there are in common between the catalogues in the corresponding row and column (e.g. KDEBLLACS and BZCat have 19 sources in common). KDE stands for KDEBLLACS and WIB stands for WIBRaLS2. All the numbers in this matrix, refer to sources found in VAST-P1.

Catalogues	Véron	BZCat	KDE	WIB
Véron	3205	203	29	149
BZCat	203	255	19	91
KDE	29	19	373	0
WIB	149	91	0	576

3.3 Sample selection

We initially had 1 063 417 radio sources across all epochs and images. The selection method described below reduced this number to 422 155.

With all the available observations, our data consisted of at most 13 observations for each radio source. To build up light curves and variability metrics (see Section 3.4.4), we ruled out objects having fewer than three observations or two detections.

To remove sources with artificial variability due to changing decomposition of extended objects, we only selected point sources. For this reason we estimated the compactness as the ratio between the integrated flux density and the peak flux density as indicated in the following equation (Huynh et al., 2012):

$$\frac{F_{int}}{F_{peak}} = \frac{\theta_{max}\theta_{min}}{b_{max}b_{min}}, \tag{3.1}$$

where θ_{max} and θ_{min} are the source full width at half-maximum (FWHM) axes, and b_{max} and b_{min} are the synthesized beam FWHM axes. We retained objects with an average compactness (integrated flux to peak flux ratio) between 0.9 and 1.5, considering the 1σ variation from the mean value of the distribution.

We decided to remove from our sample the sources with a signal-to-noise ratio SNR < 5. We also ruled out negative flux density measurements which are likely to be non-detections or artefacts.

In some cases, target sources had 'siblings' which consisted of islands (groups of pixels with neighbouring flux density emission) fitted with multiple components. This involves the presence of nearby sources, extended structure of the target source or artefacts. The VAST pipeline identifies multi-component sources via the source finder and we

remove these from our analysis. For each target source, we estimated the modulation index m, weighted reduced χ^2, mean flux density, SNR, right ascension and declination, ruling out epochs affected by siblings. The measurements of flux density with siblings were 1 280 544 out of 8 312 313 in total. In simple terms, 15% of the measurements had siblings.

3.3.1 Catalogues cross-matching technique

The VAST pipeline (Pintaldi et al., 2021) provides averaged coordinates for each radio source that we have used to cross-match with sources from the other catalogues of interest. We queried all our radio sources within a radius of 15 arcsec of the coordinates of the Véron, the Roma-BZCat, the WIBRaLS2 and the KDEBLLACS catalogues. We also aimed to select only radio cores by selecting sources with average compactness between 0.9 and 1.5 (Section 3.3). With this query method, we obtained a sample of 3204 AGN from the Véron catalogue, 578 AGN from the WIBRaLS2, 373 AGN from the KDEBLLACS and 255 from the Roma-BZCat catalogue. We found 4008 AGN in total. We ruled out multiple associations (more than one object within 15 arcsec) since in those cases, we could not distinguish real counterparts from nearby sources. Multiple associations could also be due to extended sources decomposed into several points and we aimed to study compact sources (see above in this section).

For every radio source, the probability that the nearest unrelated radio source is within an angular distance r is shown by eq. 3.2 (Condon et al., 1998) below:

$$P(r) = 1 - e^{-\pi\rho r^2}, \tag{3.2}$$

where r is the cross-matching radius in degrees and ρ is the density of radio sources from the sample selection process (422 155 sources over the 5000 deg^2 of VAST-P1). Based on eq. 3.2, the probability of having the nearest unrelated source within an angular size $r = 15$ arcsec, is ~0.5%. We are hence confident that this is a suitable radius for our query. This is also confirmed by the fact that we only found 15 multiple associations compared to over 4000 unique matches.

3.3.2 Variables selection method

We used two parameters to determine variability: the modulation index m and the weighted reduced χ^2 (Murphy et al., 2021). We define these parameters below:

$$m = \frac{1}{\overline{S}}\sqrt{\frac{N}{N-1}(\overline{S^2} - \overline{S}^2)}, \tag{3.3}$$

$$\chi^2 = \frac{N}{N-1}\left(\overline{wS^2} - \frac{\overline{wS}^2}{\overline{w}}\right), \tag{3.4}$$

where N is the number of measurements, S is the flux density value of a single measurement, $\overline{S}$ is the average flux density, $\overline{S^2}$ is the average square flux density, $\overline{S}^2$ is the square average flux density, and w is the weight defined as

$$w = \sum_{i=0}^{N} \frac{1}{\sigma_i^2}, \tag{3.5}$$

where σ_i is the error of the ith flux density measurement. Therefore, $\overline{wS^2}$ is the average of the weights multiplied by the square of flux density measurements for each source and $\overline{wS}$ is the average of the weights multiplied by the flux density measurements. To estimate these metrics we used peak flux density measurements as we wanted to focus on unresolved sources only. The modulation index m and the weighted reduced χ^2 described above were also defined in the same way by Swinbank et al. (2015) and Rowlinson et al. (2019).

We considered sources to be variable if they satisfied the following criteria: $\chi^2 \geq 2.06$ and $m \geq 0.26$. We obtained these variability thresholds by choosing 1σ (standard deviation) above the mean for both parameters.

We assumed a Gaussian distribution for both metrics in logarithm scale. This is an approximation as the two distributions are not perfectly symmetric. In Fig. 3.1 we can see the distribution of the two metrics and the whole sample of radio sources. The radio sources $\chi^2 \geq 2.06$ and $m \geq 0.26$ are 16 144 while the total number of sources is 422 155. Thus, the radio sources above the variability thresholds are 3.8% of the total sample. We found 97 AGN above the variability threshold. These candidate variables are 2.4% of the whole AGN sample which is comprised of 4008 AGN. We manually inspected light curves and radio images of these candidates variables. The final sample of AGN that we claim to be genuine variables is composed of 30 variable AGN. Hence, we found that 0.7% of the AGN sample is variable.

In particular, for these candidate variables we checked for the presence of neighbours (nearby sources) by manually examining the images of the sources. We ruled out the

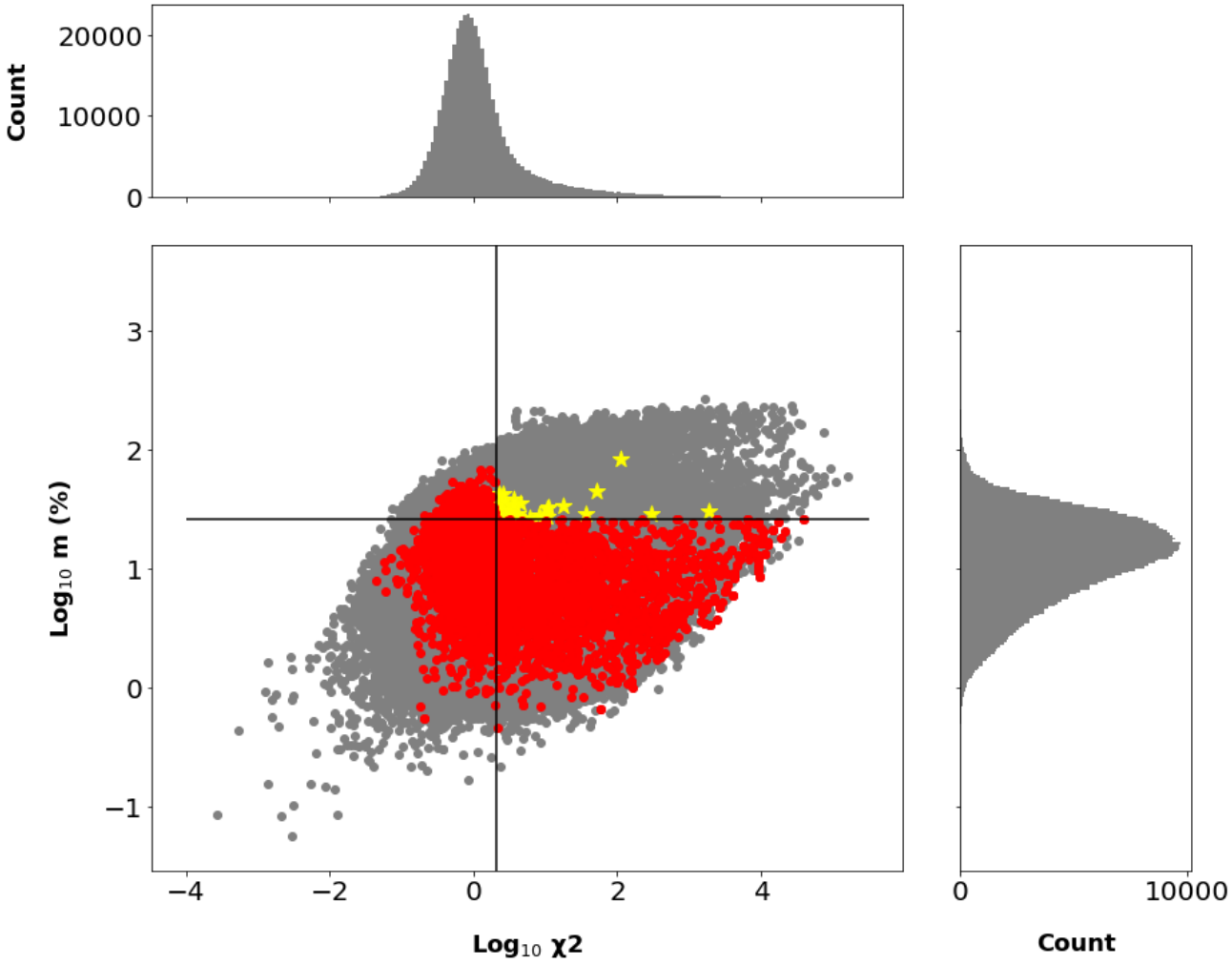

Figure 3.1: Log scale modulation index (percentage) vs. χ^2 of all the 422 155 VAST-P1 sources obtained from the sample selection (see Section 3.3). The histogram on the top is the χ^2 distribution while the histogram on the right is the modulation index distribution. The red sources are the non-variable AGN of our sample. The yellow star-like objects are the variable AGN. Sources in the top-right quadrant are variable candidates.

single epochs having neighbours that may cause a bias on measuring the flux density of the target source. This case is different from siblings. In the case of siblings, we have islands fitted with multiple components while in the case of neighbours we have a nearby source unaffected by multiple fitting. However, neighbours may cause a bias on measuring the flux density of the target source. This could happen since the value of the Gaussian fitting the target source may be contaminated by the Gaussian fitting a nearby source.

3.3.2.1 Variable AGN with higher confidence level

We also searched for AGN which are variable with higher confidence by choosing 1.5σ as our detection threshold in both m and χ^2. In this case, the threshold variability parameters are $\chi^2 \geq 3.14$ and $m \geq 0.37$. In our AGN sample there are 3 objects above these values. We term objects above 1.5σ "highly variable objects".

3.4 Results

3.4.1 Variables and their classification

Among a total number of 4008 AGN that we found in VAST-P1, we selected 30 variable AGN based on our variability metrics. The variable objects sample is comprised of 20 QSOs, 3 Seyfert galaxies and 2 BL Lacs from the Véron catalogue. There is 1 BL Lac from the Roma-BZCat catalogue which is also one of the BL Lacs found in the Véron catalogue. Finally, 5 BL Lacs are from $WISE$. In detail, we selected 3 highly variables and 27 variables. All the highly variables are QSO. Among the set of 27 variables there are 17 QSO, 3 Seyfert Galaxies and 7 BL Lacs.

Fig. 3.2 shows a modulation index m (%) vs. χ^2 plot of all of the sources and we will discuss individual sources in Section 3.4.4. We note that blazars dominate the right side of the plot with high χ^2 values. Blazars also have higher flux density values (see Table 3.3). Hence, this trend could be an effect of brightness. We did a further investigation of the error budget as a function of flux density to better diagnose this trend. We added a calibration error term in quadrature with the fitting uncertainty. We included a 6% calibration term to shift the reduced χ^2 distribution to 1.0. Bhandari et al. (2018) used the same method. However, our sample of variables have low flux densities and are not effected by this potential bias. In fact, the variables sample has not significantly changed after applying this correction.

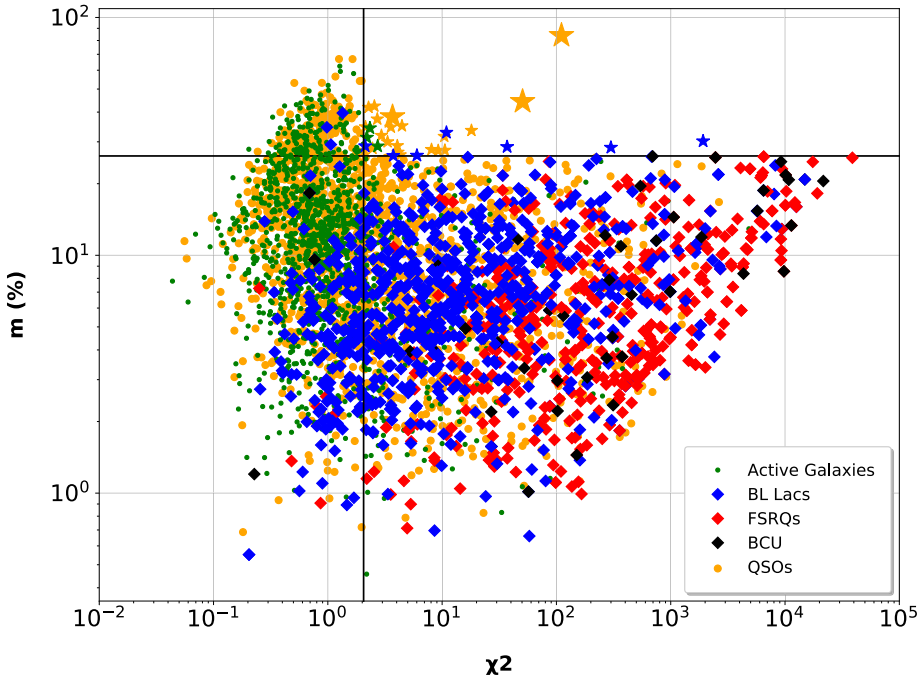

Figure 3.2: Modulation index (percentage) vs. χ^2 plot of all the 4008 AGN from this study that are found in VAST-P1. We divided the AGN per class. Both steady objects and variables are reported. The variable AGN are the star-shape markers in the graph. The biggest star-shape markers indicate the high variable AGN. The vertical and the horizontal black lines delimit the threshold values of modulation index and χ^2 for selecting variables.

3.4.2 Explanation of the radio variability

Following Miller-Jones et al. (2008) we estimated the brightness temperature of each source to understand if the variability is caused by intrinsic processes or scintillation. We used the following formula:

$$T_B = \frac{S\lambda^2}{2k_B\Omega}, \tag{3.6}$$

where S is the flux density, λ the wavelength, k_B the Boltzmann constant, c the velocity of light and Ω is the solid angle subtended by the source. The solid angle is $\Omega = r^2/D^2$ where r is the source size and D the luminosity distance. We assumed that the variability timescale is the only factor limiting on the source size r which can be written as $r = c \times \tau$, where τ is the variability timescale. This can be defined by the relation $L =$

$10^{30.96}\tau^{4.94}$, where L is the peak luminosity (Pietka et al., 2014). The minimum brightness temperature is given by:

$$T_B \geqslant \frac{\Delta S \lambda^2 D^2}{2k_B c^2 \tau^2}, \tag{3.7}$$

where ΔS is the variability amplitude. The same approach to estimate the minimum brightness temperature was also adopted by Bell et al. (2014). We also considered an increase of brightness temperature due to the relativistic beaming effect in radio jets. The amplification is given by a factor D_p^3(Lähteenmäki et al. 1999, Bell et al. 2014). To remove this amplification we divided the brightness temperature by this factor, adopting a value $D_p = 10$ which is consistent with estimations from previous studies (e.g. Hovatta et al. 2009). We hence calculated the minimum brightness temperature for each object of the sample. To estimate the timescale for each variable, we took the minimum timescale over the modulation index of two consecutive observations (Mooley et al., 2016) was above 0.26 (modulation index threshold for selecting variables). Murphy et al. (2021) also used the same technique to estimate the timescale variability. Fig. 3.3 shows the distribution of the timescale variability for all the variable AGN. A distribution of the brightness temperature is shown in Fig. 3.4. Intrinsic variability coexisting with a brightness temperature $T_B > 10^{12}$K would be above the Compton catastrophe limit (Kellermann & Pauliny-Toth, 1969). This leads to a conclusion of scintillation as the main cause of the observed variability in our variable AGN. In the KDEBLLACS catalogue there are no redshifts for the blazars, so we used the NASA/IPAC Extragalactic Dataframe (NED[1]). We found a redshift value for two of the variable KDEBLLACS blazars. For the other three blazars we assumed a low redshift $z = 0.001$. This low redshift minimises the brightness temperature. Although, we still have brightness temperature values $T_B > 10^{12}$K. The value $z = 0.001$ is lower than the redshift of Centaurus A and Circinus which are the nearest Radio galaxy and the second nearest AGN in the Southern sky, respectively (Prieto et al., 2010). We obtained the redshift of Centaurus A ($z = 0.00183$) and Circinus ($z = 0.00145$) from NED.

3.4.3 Scintillation as a function of Galactic latitude

The purpose of this section is to test a model to predict the modulation index of scintillat-

[1]The NASA/IPAC Extragalactic Database (NED) is operated by the Jet Propulsion Laboratory, California Institute of Technology, under contract with the National Aeronautics and Space Administration (https://ned.ipac.caltech.edu/).

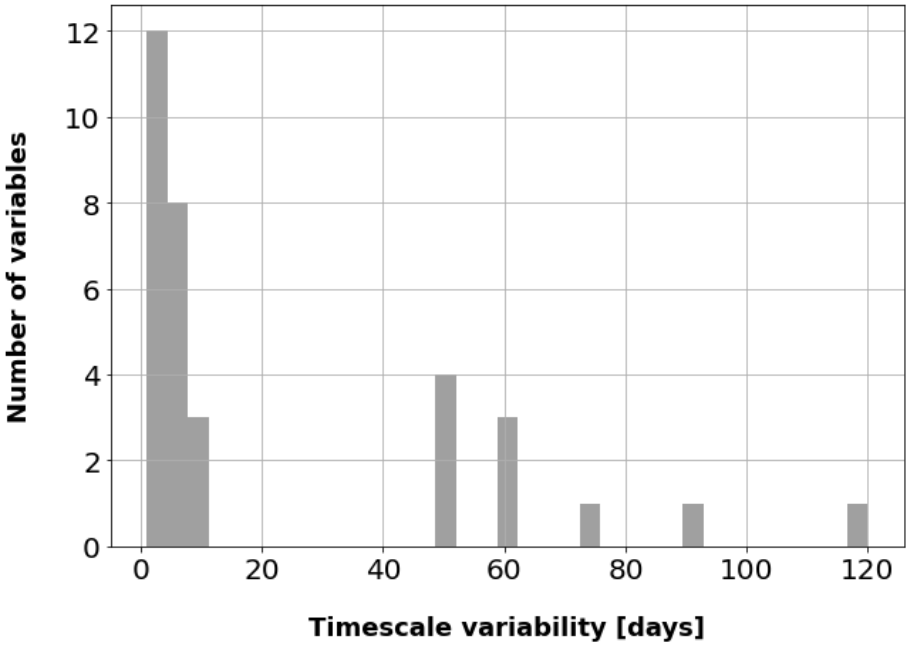

Figure 3.3: Histogram of the timescale that we estimated for every variable. Most variable AGN show variability in a time interval between 1 and 9 days.

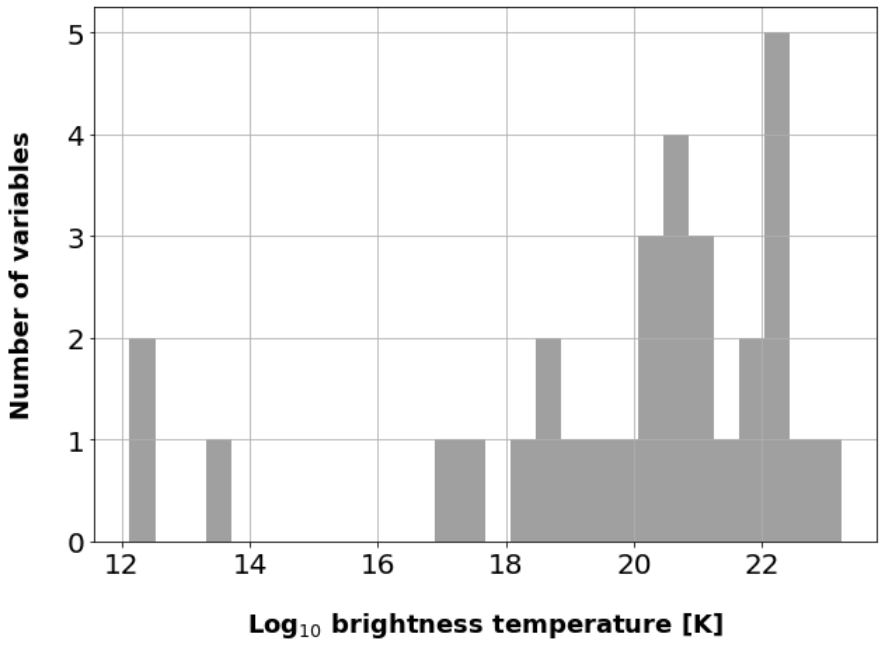

Figure 3.4: Distribution of brightness temperature values (logarithm scale) of the sample of variable AGN. The values above 10^{12}K show that the variability is due to scintillation.

Table 3.3: χ^2 and flux density mean values of the 4006 AGN from this study that are found in VAST-P1. The χ^2 and flux density errors are the standard deviations of the mean. In this table the entire AGN sample is divided in two groups: blazars and non-blazar AGN. We also describe three classes of blazars (FSRQs, BL Lacs and BCU) and two classes of non-blazars (QSOs and Active Galaxies). The Active Galaxies class is composed of LINERs and Seyfert Galaxies.

Class	Total	$\langle\chi^2\rangle \pm \sigma_{\langle\chi^2\rangle}$	$\langle S_{peak}\rangle \pm \sigma_{\langle S_{peak}\rangle}$ [mJy]
Blazars	1311	666.2 ± 62.2	121.4 ± 7.1
FSRQs	445	1221.3 ± 143.5	213.4 ± 14.6
BL Lacs	817	243.3 ± 40.9	57.7 ± 5.5
BCU	49	2675.6 ± 643.8	346.8 ± 81.5
Non-blazar AGN	3097	137.7 ± 19.7	40.4±3.2
QSOs	1770	202.5 ± 32.4	51.7 ± 4.4
Active Galaxies	1327	51.2 ± 15.4	25.4 ± 4.5

ing sources. A comparison between model and data shows the goodness of the modelled predictions. Testing a model is a key point to better understand the distribution of interstellar medium which is correlated with scintillation. Propagation effects through the interstellar medium generate variations of the flux densities of compact sources (Rickett, 1990). The degree of variability caused by scintillation increases with decreasing Galactic latitude (Hancock et al., 2019), and therefore the effects of scintillation will be more prominent in certain regions of the VAST-P1 footprint.

Radio variability at about 1 GHz is mainly caused by strong scintillation (Lazio et al., 2004). There are two types of strong scintillation: refractive interstellar scintillation (RISS) and diffractive interstellar scintillation (DISS). Because AGN are in general too extended to be affected by DISS (Lazio et al., 2004), we considered RISS to be the most likely scintillation regime that we observe in our data. However, we do not completely rule out the possibility to observe DISS since in the literature there is a case of AGN showing DISS (Macquart & de Bruyn, 2006). Other works also report the analysis of single AGN and state that DISS could play a role (McCallum et al. 2007, Tuntsov et al. 2017).

Hancock et al. (2019) presented a model for RISS. The model is based on H_α intensity maps to get a scintillation strength $\xi = r_F/r_{dif}$ where r_F is the Fresnel scale and r_{dif} is the diffractive length scale. The model shows a more evident RISS at lower absolute

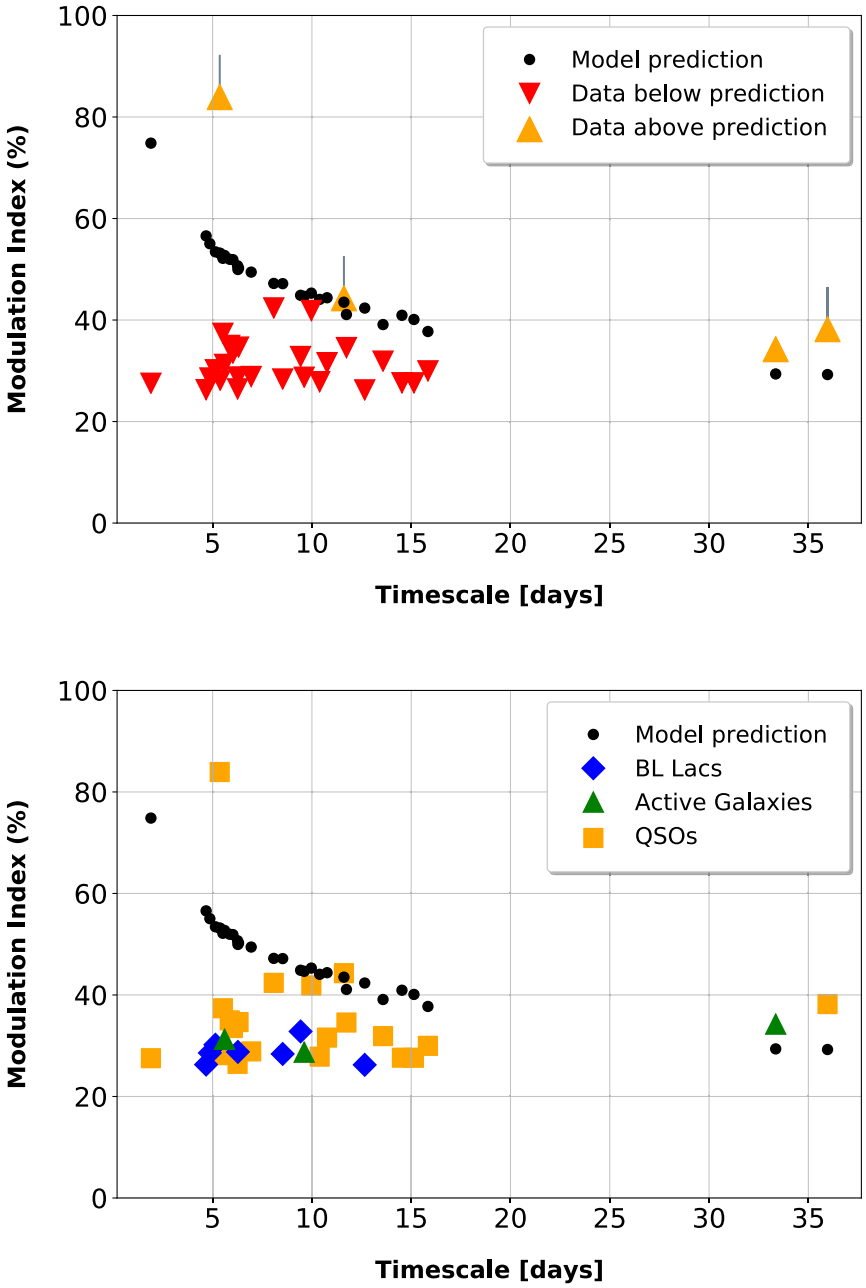

Figure 3.5: Modulation index vs. timescale. In these two plots we have the modulation index values predicted by the scintillation model, as well as the observed modulation index values. The orange and red triangles are the observed data (plot on the top). Most sources have modulation indices below the predictions (red triangles pointing down). Four objects have observed modulation indices values larger than the predicted ones (oranges triangles pointing up). Objects with the grey tick-up are high variables. The plot on the bottom shows the objects by class. All variable BL Lacs have modulation index values below the predictions.

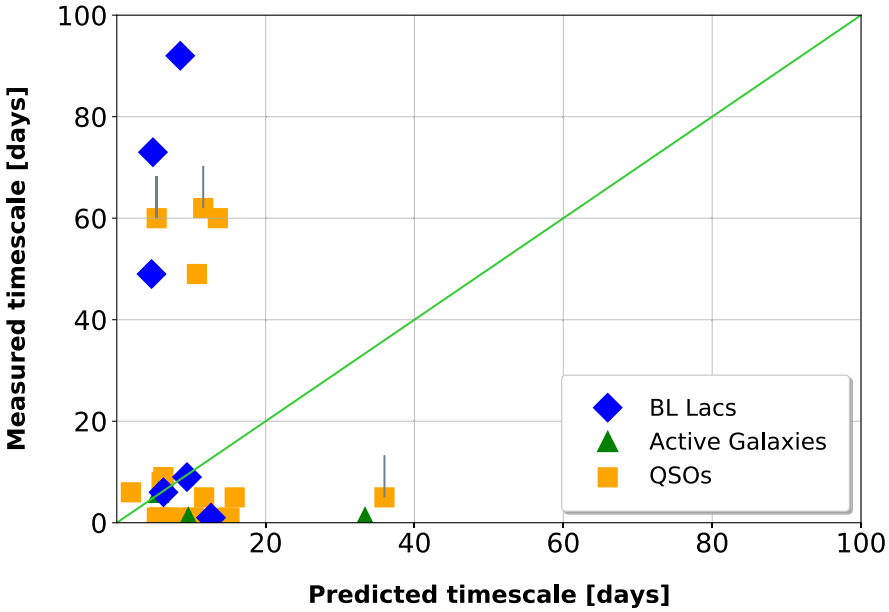

Figure 3.6: Measured timescale vs. Predicted timescale. Objects on the green line have a measured timescale consistent with the predicted one. For objects below the green line, the predicted timescale is longer than the observed one. For objects above the line, the opposite is true. The objects with the grey tick-up are highly variables.

values of the Galactic latitude. For each variable AGN we measured the modulation index value (see eq. 3.3). The scintillation model also gave us modulation index values (predicted values) and variability timescale. We compared the observed values with the predicted values (see Fig. 3.5). We also compared the timescales predicted by the model with the timescale that we have estimated (Fig 3.6). See Section 3.4.2 for our timescale estimation method.

Most observed modulation indices are considerably below the predicted ones, especially for lower predicted timescale values. This is not surprising since the model is likely to overestimate the modulation index values because of its limitations. For instance, in each radio source where a compact component is within in a diffuse region, we would have a modulation index reduced by a factor $1-f$, with f being the flux density from the compact component. Hancock et al. (2019) reported that this model only considers the behaviour of the compact component. This causes an overestimation of the modulation index.

For the longest predicted timescales the observed modulation indices are above the predicted ones. The reason could be due to the presence of small structures (not possible

to resolve above a resolution of 6 arcsec in the Hα maps). The model underestimates the modulation index and overestimates the timescale for small scale structures (see Hancock et al. 2019 for details). In detail, we are referring to the two variables with predicted timescale of roughly 35 days (see Fig. 3.5). This overestimation of the predicted timescale is also confirmed by Fig 3.6, where we can see that the two variables have a predicted timescale nearby 35 days but a measured timescale below 20 days.

The observed modulation indices are never below the predictions for the high confidence variables (objects with grey tick-up in Fig. 3.5). This could be partially explained by the presence of small structures as explained above. Indeed, one highly variable AGN is among the objects with the longest predicted timescale (longer than 20 days). We could have the same explanation for highly variables at shorter timescales. If this is correct, their actual timescale would be even shorter than what was predicted by the model as the model overestimates the timescale when there are small structures. However, in Fig 3.6 these two highly variables have an observed timescale of about 60 days which is longer than the predicted one. On the other hand, our light curves are not heavily sampled. In fact, between two consecutive data points we can find time intervals of months.

In general, the model underestimates the modulation index of highly variables and overestimates the modulation index of variables. Therefore, the presence of small scale structures may not be the only reason for underestimating observed modulation indices.

We tried to verify if the objects with measured modulation index above the predictions are in a region with a particular distribution of interstellar medium, causing an amplification of the modulation index. These objects are at nearly equatorial declination (from -6° and 3°). The largest region of sky covered by both the Véron catalogue and VAST-P1 is also at nearly equatorial declination (from -10° to 4°). Hence, we cannot state if these objects are in a region where there is a different distribution of interstellar medium.

We also verified the anti-correlation between modulation index and timescale predicted by the model (Fig. 3.5). Despite the gap between observed values and predicted values, there are no variable AGN with large modulation index and large timescale. This is a point of agreement between observations and predictions. Note that Hancock et al. (2019) found a similar behaviour with observed data.

If we only consider objects with observations above the predictions, we see that the data are much more consistent with this anti-correlation. However, most sources do not have relations with the predicted timescale.

Comparing the predicted timescales with the measured ones (Fig 3.6) showed that for most objects there is no agreement between model and observations. This is due to two main reasons: the limits of the model explained above in this Section and the not heavy sampling of our light curves as there are several months between some consecutive data points (see Fig 3.8).

3.4.4 Single source analysis

We describe all the variable AGN in Table 3.5. From this table we can see that the source with the highest redshift is a BL Lac (ASKAP J013127.3−032059 with photometric $z = 5.2$). This is interesting because it is generally difficult to observe spectral lines in BL Lacs and, hence, measure their redishift (Falomo & Treves, 2007). We also show the light curve for every variable AGN (see Fig. 3.8). We measured the flux densities using the software **Selavy** (Whiting, 2012). Large flux density errors in the light curves are due to forced measurements which are measurements obtained by a forced extraction of a Gaussian fit when there is no detection (see Pintaldi et al. 2021 for more details).

For the highly variable AGN we also show VAST-P1 radio images (see Fig. 3.7). We found 25 variable AGN from the Véron catalogue and 5 variable AGN from the KDEBLLACS. We also found one variable object from the Roma-BZCat catalogue, which is also contained in the Véron catalogue. We found 3 highly variable objects which are 3 QSOs. We also found 27 variables which are 17 QSO, 3 Seyfert galaxies and 7 BL Lacs. For each Véron source, we also report the redshift which is given in the catalogue. Note that there is no redshift associated with 3 KDEBLLACS sources. We found the redshfit for 2 KDEBLLACS thanks to NED. Note also that we have not found variables in the other catalogue listing *WISE* blazars (WIBRaLS2).

3.5 Discussion and conclusions

In this paper, we have described a time-domain analysis of AGN using the VAST-P1 and RACS data. We searched VAST-P1 and RACS for radio counterparts of AGN listed in several large catalogues.

We found 30 variable AGN over the 5000 deg^2 sky area of VAST-P1. The total number of AGN detected was 4008, which means that 0.7 per cent of our sample are variable objects. We reported the percentage of variable objects for every spectral class in Table 3.4. QSOs have the largest percentage of variable sources (1.1 per cent). Note that we did

not report data regarding the LINERs since in the Véron catalogue these objects are described to also be possible Seyfert galaxies. Hence, their classification is uncertain. It is of interest that we did not find variable FSRQs. This could be due to the presence of compact steep spectrum (CSS) sources with a spectral turnover at low radio frequency (between 200 and 843 MHz) with a descending component in the spectrum at higher frequencies (Callingham et al., 2017). Low-frequency soft sources can also be a possibility. These are radio sources with a turnover between 72 and 231 MHz (Callingham et al., 2017). On the other hand, there are also non-variable FSRQs with a modulation index very close to 26% and χ^2 far above 2.06 (see Fig. 3.2). We recall that these numbers are the threshold for selecting variables. The total number of FSRQs is also lower than for other classes (see Table 3.3) and it is less likely to find variables in a smaller sample.

We classified 27 AGN as variable objects (above 1σ in m and χ^2). We also selected 3 highly variable AGN which are 0.07 per cent of the whole AGN sample. Highly variables are above 1.5σ in m and χ^2. We found that 3 QSOs are highly variables. Considering that QSOs are the largest population in our sample, it is not a surprise that most variables are QSOs. None of the 7 variable BL Lacs is highly variable. This is plausible since blazars are the AGN class with the largest χ^2 but lowest modulation index.

The cause of variability in our sample is most likely explained by scintillation because the brightness temperature values are larger than the Compton catastrophe limit (10^{12} K). These values are above this limit even after dividing by a factor D_p^3. This result is consistent with previous studies in the low-radio-frequency regime (below 1 GHz) showing extrinsic variability on these time-scales (Hunstead 1972, Heeschen & Rickett 1987, Rickett 1990, Lovell et al. 2003, Bell et al. 2014).

At the frequency of VAST-P1 (888 MHz) we expect to observe variability due to strong scintillation (Lazio et al., 2004). Diffractive intensity scintillations (DISS) and refractive intensity scintillation (RISS) can be significant at the observing frequency of VAST-P1. RISS is likely to be the cause of variable AGN in our data since AGN are generally too extended to show DISS (Lazio et al., 2004). Nevertheless, in the literature there are works describing DISS in AGN (Macquart & de Bruyn 2006, McCallum et al. 2007, Tuntsov et al. 2017). Hence, we cannot completely rule out DISS from our AGN sample.

We have shown that our measured modulation indices are systematically lower than the ones predicted by a scintillation model. Hancock et al. (2019) also reported a gap between the model and data. This is not surprising since the model is likely to overestimate the measured values. However, the model underestimates the modulation indices of the highly variable objects.

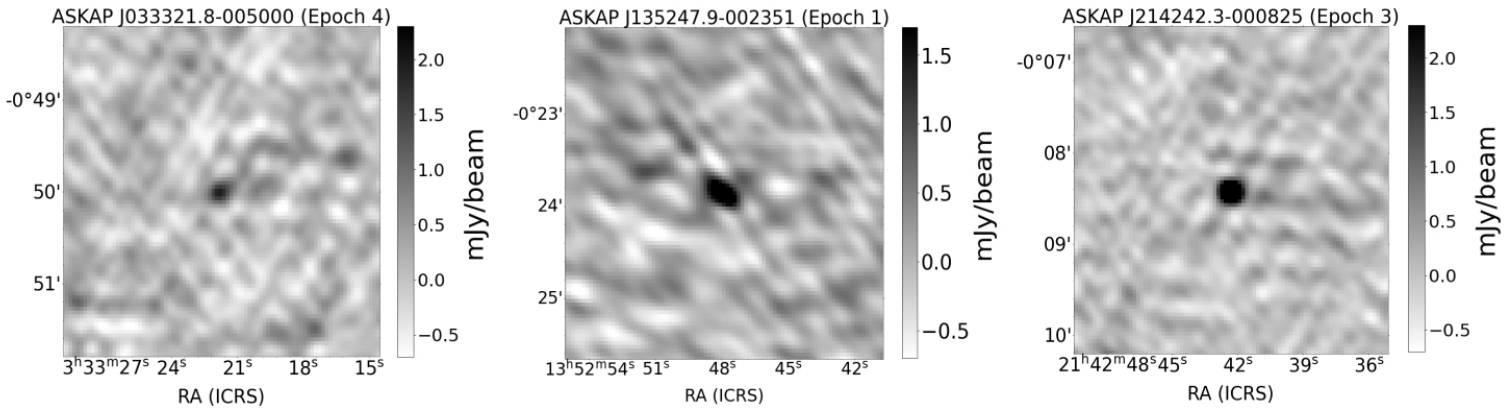

Figure 3.7: Radio images of the 6 high variable AGN. Each source is in the centre of its radio image. VAST 090626.8+033311 is a Seyfert galaxy while the other plotted sources are QSOs.

Table 3.4: Proportion of variables in each AGN class and for the overall study, expressed as both a ratio and a percentage.

Sources	Ratio	%
Seyfert galaxies	3/750	0.4%
BL Lacs	7/817	0.9%
QSOs	20/1770	1.1%
Total	30/4008	0.7%

The scintillation model also predicts an anti-correlation between modulation index and timescale that we tested. There is a wide gap with most observations which do not show a clear anti-correlation. Nevertheless, the distribution of objects above the predictions shows a modulation index decreasing with the timescale.

Several developments of this work are possible. The next developments of this work can involve the usage of the subsequent data releases of RACS and VAST. Using a larger number of epochs spanning a total timescale on the order of years, we can also search for AGN that are not variable over one year of observations but could be variable in the longer term. An "untargeted search" in VAST-P1 of AGN not listed in AGN catalogues will also be useful. Murphy et al. (2021) already found 2 highly variable AGN (selected by choosing 2σ as threshold for variables). Additionally, RISS and intrinsic variability are connected through compactness of sources (Koay et al. 2018, Said et al. 2020). Multi-wavelength observations might be useful for investigating this relation.

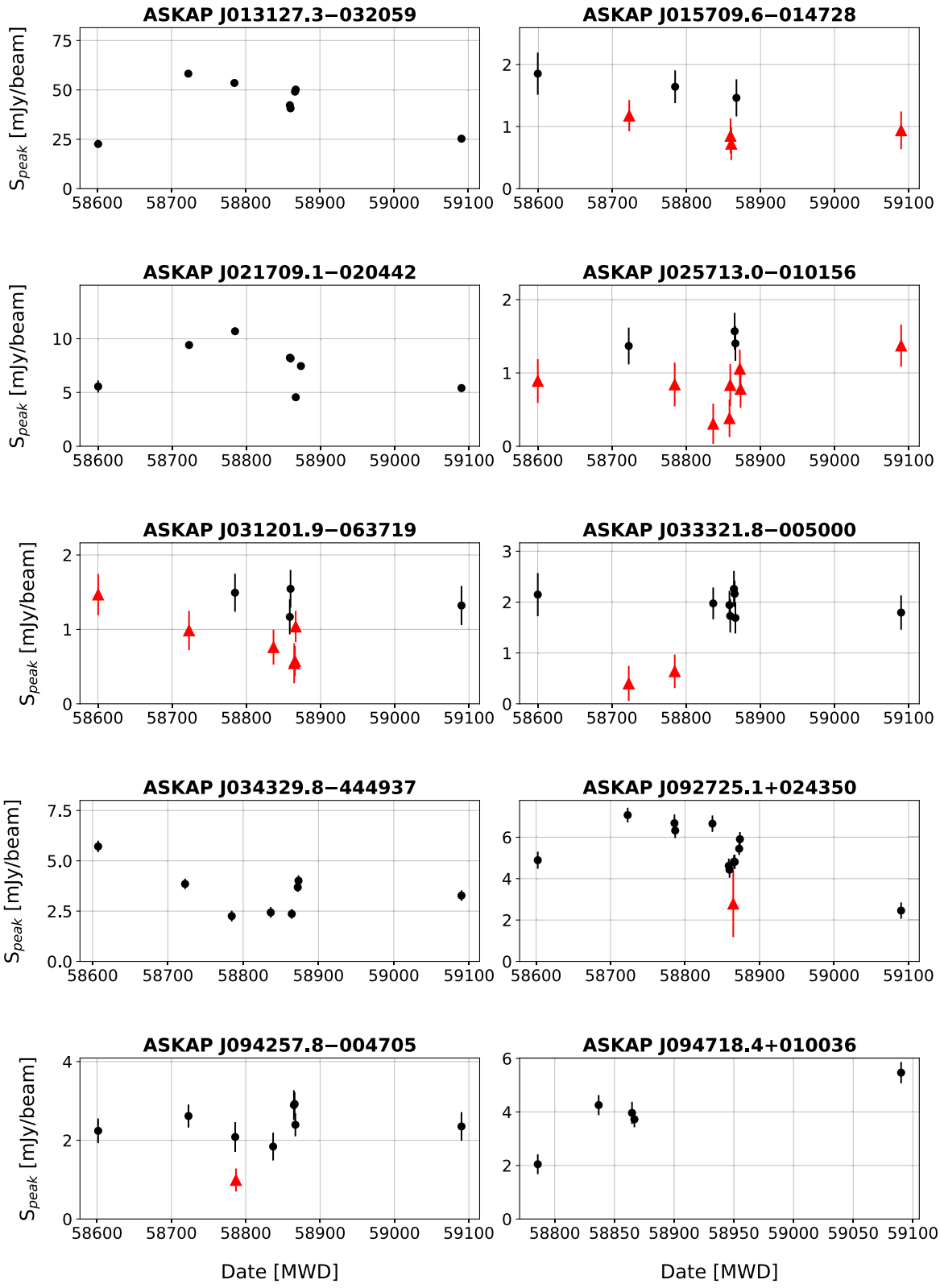

Figure 3.8: Light curves of the variable AGN. The black points are Selavy measurements while the red triangles are forced measurements.

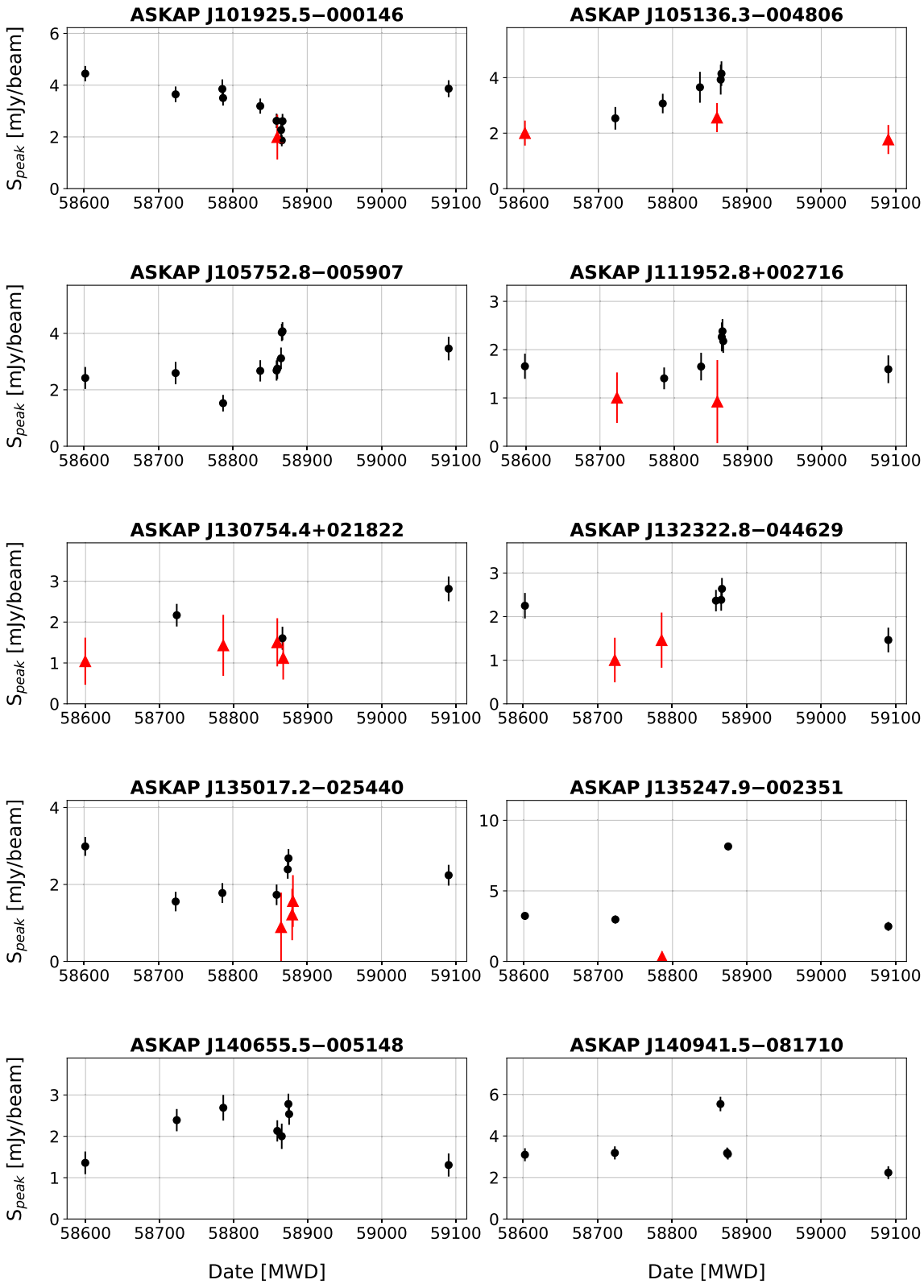

Figure 3.8: (continued) Light curves of the variable AGN. The black points are Selavy measurements while the red triangles are forced measurements.

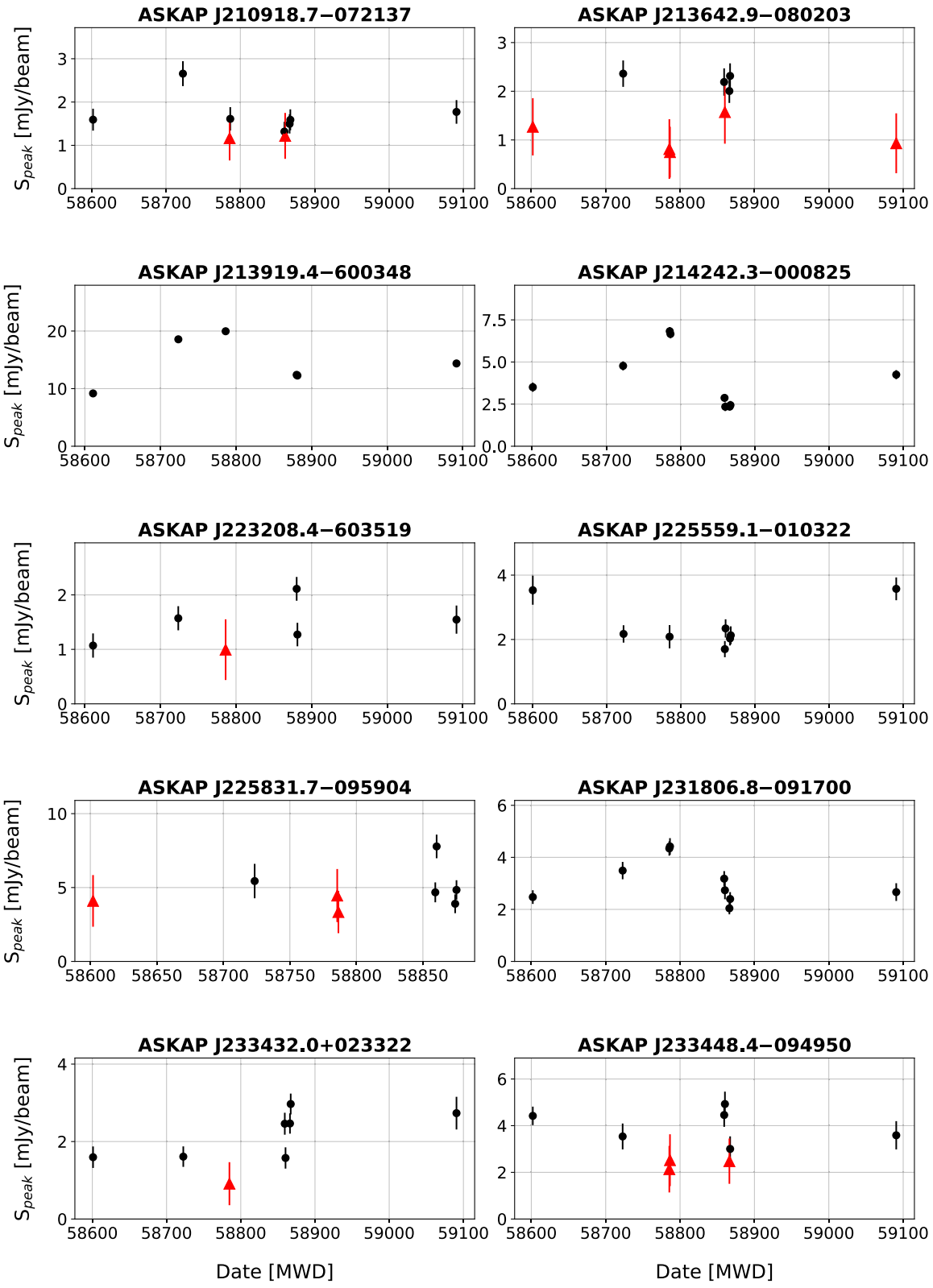

Figure 3.8: (continued) Light curves of the variable AGN. The black points are Selavy measurements while the red triangles are forced measurements.

Table 3.5: Main properties of the Véron and KDEBLLACS variable AGN. The KDEBLLACS AGN are in the last five rows. For each source we report the VAST-P1 name, spectral class, χ^2 value, modulation index and redshift.

ASKAP name	Class	χ^2	$m(\%)$	z
ASKAP J015709.6−014728	QSO	2.1	34.7	0.9
ASKAP J025713.0−010156	QSO	2.5	42.4	1.9
ASKAP J033321.8−005000	QSO	3.7	38.2	1.1
ASKAP J034329.8−444937	QSO	18.1	33.5	1.5
ASKAP J092725.1+024350	QSO	10.6	27.6	0.7
ASKAP J094718.4+010036	QSO	10.4	31.6	0.9
ASKAP J101925.5−000146	QSO	8.1	27.8	0.8
ASKAP J105136.3−004806	QSO	3.3	30.0	1.3
ASKAP J130754.4+021822	QSO	2.7	37.4	1.9
ASKAP J132322.8−044629	QSO	2.9	31.9	0.4
ASKAP J135017.2−025440	QSO	3.6	34.6	2.2
ASKAP J135247.9−002351	QSO	110.7	83.9	1.7
ASKAP J140655.5−005148	QSO	4.3	26.4	2.4
ASKAP J210918.7−072137	QSO	2.1	27.6	1.2
ASKAP J213642.9−080203	QSO	2.3	41.9	2.0
ASKAP J214242.3−000825	QSO	50.6	44.3	1.3
ASKAP J225559.1−010322	QSO	4.1	28.9	1.8
ASKAP J225831.7−095904	QSO	2.5	28.2	1.9
ASKAP J231806.8−091700	QSO	9.2	27.5	1.8
ASKAP J233432.0+023322	QSO	4.5	35.0	4.1
ASKAP J105752.8−005907	BL Lac	6.0	26.3	0.5
ASKAP J094257.8−004705	BL Lac	3.7	26.2	1.4
ASKAP J223208.4−603519	Seyfert 2	2.7	28.7	0.3
ASKAP J031201.9−063719	intermediate Seyfert	2.3	34.3	0.4
ASKAP J111952.8+002716	Seyfert 1	2.2	31.3	0.4
ASKAP J013127.3−032059	BL Lac	1919.7	30.2	5.2
ASKAP J021709.1−020442	BL Lac	37.0	28.6	N/A
ASKAP J140941.5−081710	BL Lac	10.9	32.8	N/A
ASKAP J213919.4−600348	BL Lac	299.5	28.4	N/A
ASKAP J233448.4−094950	BL Lac	2.1	28.8	0.21

Part II

Part II

CHAPTER 4

MODELLING TIME SERIES IN ASTROPHYSICS

In this Chapter, I propose the usage of an innovative method for selecting transients and variables using State Space Models (Tusell, 2008) which are also referred to as Dynamic Linear Models (Tusell, 2008). State Space Models (and more generally parametric auto-regressive models) have been the mainstay of economic modelling for some years, but rarely they have been used in Astrophysics. These models could be used to detect transients in complex scenarios, such as the case of a transient source within an active galaxy (e.g. Keane et al. 2016), whereby it is difficult to determine using the metrics commonly used in time-domain radio astronomy (e.g modulation index or χ^2 described in Section 3.3.2) if the variability is stochastic (and related to the AGN) or transient (and related to an explosive and independent object within the galaxy).

The statistics currently used to identify variables and transients (see eq. 3.3 and eq. 3.4) are not sophisticated enough to distinguish different types of variability. They simply report on the overall modulation and significance, and the ordering of the data in time is insignificant. State Space Models are much more advanced and can encode not only the amount and significance of the variability but also properties, such as slope, rise or decline for a given time t.

If we observed a variable active galaxy hosting a gravitational waves (GW) transient, or indeed any other transient source, it could be difficult to separate out and distinguish the two processes. This was indeed the scenario that was realised for FRB 150418 (Keane et al., 2016). It was initially reported that the radio variability was due to the afterglow of a transient source which was a fast radio burst called FRB 150418 (e.g. Keane et al. 2016,

Johnston et al. 2016) but later it was recognized that it was the standard scintillation behaviour of the hosting AGN (Williams & Berger, 2016).

In this chapter I evaluate the effectiveness of State Space Models for transient and variable detection including classification in time-series astronomy.

4.1 Why State Space Models?

The current strategy adopted for selecting variables in Section 3.3.2 has been successfully used in a number of studies (e.g. Bell et al. 2015, Swinbank et al. 2015, Rowlinson et al. 2019, Murphy et al. 2021). State Space Models can identify more features in time series (e.g. the level component in the Local Level Model see Section 4.3.2).

The case of the FRB 150418 is an example of a difficult scenario where State Space Models could be successfully used in Astrophysics. In 2015 a fast radio burst (FRB, Lorimer et al. 2007) called FRB 150418 was detected (Keane et al., 2016). The transient was hosted by the galaxy WISE J071634.59−190039.2. However, other works claimed that there was no transient activity and only a scintillating AGN was observed (e.g. Johnston et al. 2016, Williams & Berger 2016). It is important to distinguish these two different scenarios and State Space Models can help to achieve this.

The case of FRB 150418 caused debate about the detection, or the non-detection of a radio transient (e.g. Keane et al. 2016, Williams & Berger 2016) hosted by a scintillating AGN. State Space Models could extract the typical features of time series and resolve this kind of issues. For example, we could use a model to distinguish an AGN from a transient source. For instance, a stochastic trend would indicate a scintillating AGN. A trend is called stochastic if it is a random function of time (Hyndman, 2018). A transient source model would have instead a rising phase, a peak and declining ending trend. We could then distinguish the possible transient from the hosting AGN.

State Space Models could be used to classify transients and variables. Time domain astronomy includes the study of quite different objects such as gamma-ray bursts, flare stars, variable AGN etc, where each of object has its own physical process driving a specific kind of time series. For example, variable AGN are likely to show stochastic light curves with a variable behaviour lasting on time scales of months (see Chapter 3). Alternatively, flare stars can show light curves with bursts on the timescale of days (see Chapter 2) and Gravitational Waves afterglows can show a unique bursting light curve (e.g. Dobie et al. 2018). State Space Models can represent all these different behaviours, therefore these models may be used to identify and classify known and

unknown transients.

Moreover, advanced statistical models are not completely new to Astrophysics. Parametric autoregressive models have been applied in a few works (Lazio et al. 2001, Templeton & Karovska 2009, Kelly et al. 2014, Feigelson et al. 2018). In particular, Lazio et al. (2001) used these models to study the radio light curves of 149 radio sources at 2.5 and 8.2 GHz. The authors used autoregressive and moving average models and found that the sources analysed presented short-term variability (~10 days) caused by radio-wave scattering in an extended medium. Note that this is the only work at radio frequencies using advanced statistical time series models that I found in literature.

However, these techniques have been used in other bands of the electromagnetic spectrum. Templeton & Karovska (2009) worked at optical wavelengths to examine variable stars. An autoregressive moving average (ARMA) model (see Section 4.3.3.6) was used to search for quasiperiodic and variable behaviour. The model also included a seasonal component as it was known that there was a period of 333 days in the data. The analysis allowed the authors to rule out long secondary periods in a sample of AGB variables (see Templeton & Karovska 2009 for more details). Kelly et al. (2014) analysed optical AGN light curves, the X-ray light curve of a binary system and the optical light curves of variable stars using a continuous-time autoregressive moving average model (see Kelly et al. 2014 for model explanation). Thanks to this model, it was possible to estimate power spectra in the light curves. It is also possible to identify variability features that could be used for variability selection methods and identifying new classes of variables. Feigelson et al. (2018) also provided an exhaustive explanation on the analysis of variable stars (optical band). For instance, Feigelson et al. (2018) used a moving average (MA) process which allows to describe a rise or a decline between two consecutive data points (see Section 4.3.3.6 for more details). Autoregressive models with moving average (MA) process were also used to study variable AGN (Bhattacharyya et al. 2020, Sarkar et al. 2020).

In addition, these models have been widely used in Economy, climate change, forensic sciences and several other fields. There is definitely a lack of the usage of these methods in Astrophysics.

4.2 The first gravitational waves source observed by telescopes: GW170817

4.2.1 The discovery of gravitational waves

In 2015 the Laser Interferometer Gravitational-Wave Observatory (LIGO) detected gravitational waves for the first time in history (Abbott et al., 2016c). The extraordinary discovery confirmed what had been predicted by Albert Einstein almost 100 years previously as a result of the General Theory of Relativity. Rainer Weiss, Barry C. Barish and Kip S. Thorne were awarded the Nobel Prize thanks to this result in 2017. The source detected by LIGO was a binary black-hole merger (GW150914, Abbott et al. 2016a). Unfortunately, an observation by electromagnetic telescopes was not possible because of the absence of radiation from black holes (Zhang et al., 2016). In particular, electromagnetic radiation should be generated by an accretion disk around the newly formed black hole. The accretion time scale is, however, shorter than the coalescence time necessary for the two black holes in GW150914 (Zhang et al., 2016) therefore, before the merging stage of the two black holes, all of the available matter would be absorbed into the black holes.

However, on 17 August 2017 gravitational waves from two colliding neutron stars were detected (GW170817, Abbott et al. 2017a). The source was 10.6 arcsec (or 2 Kpc) off-set from the centre of the NGC 4993 galaxy (Coulter et al., 2017). The *Fermi* satellite detected electromagnetic radiation (gamma-rays) 1.7 seconds later than the LIGO detection. The gamma-ray counterpart was also detected by *INTEGRAL*, two seconds later than LIGO (Savchenko et al., 2017). The X-ray counterpart was detected by Chandra on 26 August 2017 (Troja et al., 2017) and on 18 August 2017 *Swift* provided the UV and the optical counterparts (Evans et al., 2017). Further optical and infrared counterparts were detected by several teams within 12 hours (Chornock et al., 2017). The radio counterpart was detected 16 days post-burst by the Jansky Very Large Array (JVLA) and confirmed by the Australia Telescope Compact Array (ATCA) as reported by Mooley et al. (2018). Fig. 4.1 shows radio images of the source obtained from the Giant Metrewave Radio Telescope (GMRT), the Very Large Telescope Array (VLA) and the Australia Telescope Compact Array (ATCA).

The observation of GW170817 had an important significance for Astrophysics. Apart from the confirmation of the existence of gravitational waves, other physical phenomena were also confirmed. For example, it has been confirmed that gravitational waves travel

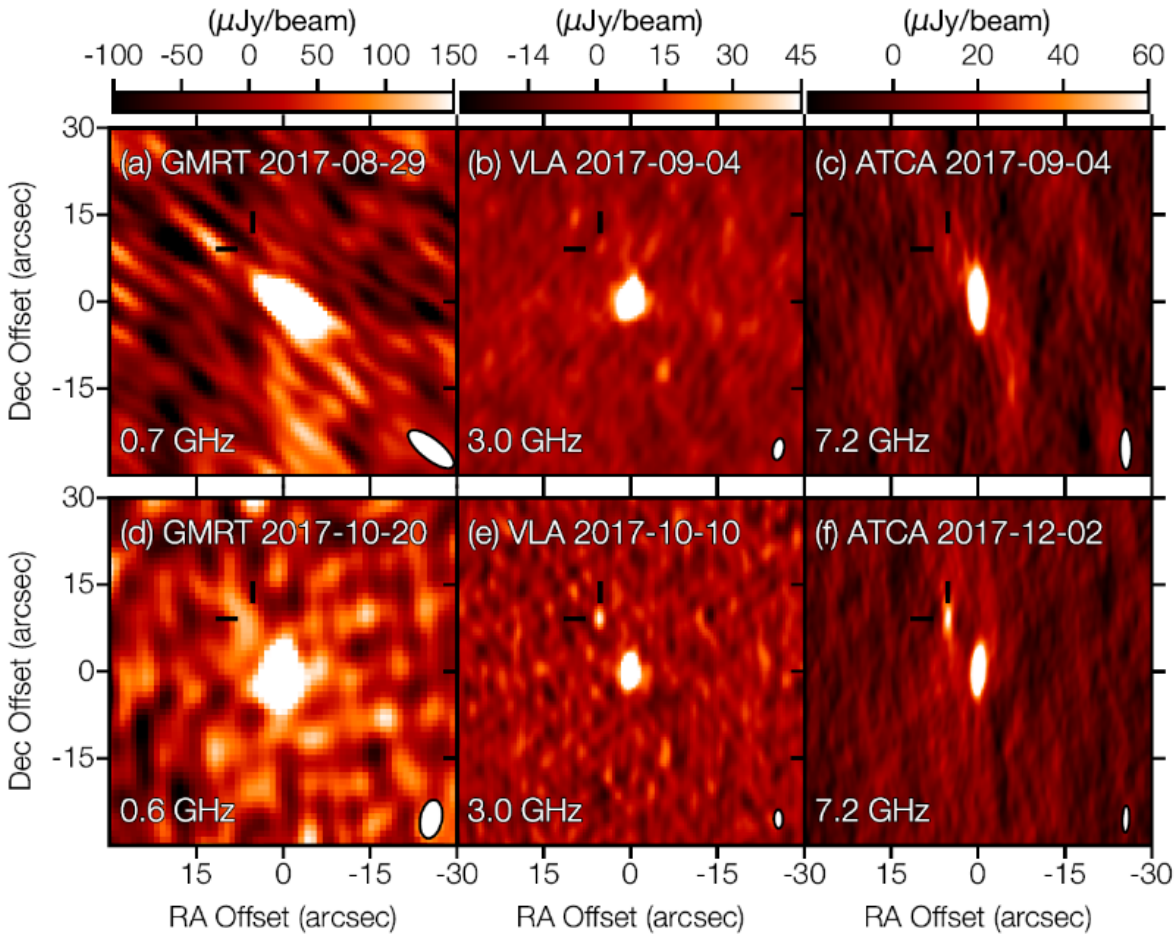

Figure 4.1: Images cutout from three radio telescopes: Giant Metrewave Radio Telescope (GMRT), Very Large Array (VLA) and Australia Telescope Compact Array (ATCA). The two black lines indicate the position of the gravitational waves source. Panels (a), (b) and (c) show images from August to September 2017. Panels (d), (e) and (f) show images from October 2017. The white ellipse in the lower right corner of each image is the synthesised beam. Credit: Mooley et al. (2018).

at the light speed (Abbott et al., 2016a). This detection confirmed that short gamma-ray bursts (sGRBs) are linked with gravitational waves (Abbott et al., 2016d) and previously, this was only a theory (Narayan et al., 1992). Another important implication is the confirmation of heavy elements being produced by neutron stars mergers (Drout et al. 2017, Kasen et al. 2017). Theoretical models show that matter expelled from a two neutron star merger event, can assemble into heavy elements such as gold and platinum thanks to the r-process (Lattimer & Schramm 1974, Sekiguchi et al. 2016). A comparison between these models and the optical and infrared radiation of GW170817 was done by Kasen et al. (2017). The study showed two different components of the ejecta: one mostly comprised of light elements and one of heavy elements. Kasen et al. (2017) specify that light elements have a mass number lower than 140, while heavy elements have a mass number above 140. Kasen et al. (2017) demonstrate that neutron stars mergers are a dominant formation channel for forming heavy elements through the r-process.

Abbott et al. (2017b) also reported a new and independent measurement of the Hubble constant ($H_0 = 70.0^{+12.0}_{-8.0}$ km s^{-1} Mpc^{-1}). The value estimated is consistent with previous measurements. For instance, Planck Collaboration et al. (2016) measured H_0 = 67.8± 0.9 Km s^{-1} Mpc^{-1} analysing Planck observations of temperature and polarization anisotropies of the Cosmic Microwave Background (CMB). Another example is given by Riess et al. (2016); the authors used near-infrared data from the Hubble Space Telescope (HST) to observe Cepheid variables. The measurement of the Hubble constant reported was H_0 = 73.2± 1.7 Km s^{-1} Mpc^{-1}.

4.2.2 Electromagnetic emission models of GW170817

Kasliwal et al. (2017) considered different models to explain the electromagnetic counterpart (EM170817) of GW170817. The electromagnetic counterpart is not caused by a classical gamma-ray burst with ultra-relativistic jets (Kasliwal et al., 2017). Below, I briefly discuss each model and show why a classical gamma-ray burst has been ruled out. Fig. 4.2 is a representation of the models.

4.2.2.1 Classical on-axis short hard gamma-ray burst model

A classical short gamma-ray burst (sGRB) has an ultra-relativistic jet (Lorentz factor $\Gamma >\sim 100$) on the line-of-sight with an opening angle is $\theta \sim 10^{\circ}$ (Model A, Fig. 4.2).

The observed gamma-ray luminosity of EM170817 is about 10^{47} erg s^{-1} which is four orders of magnitude lower than expected in a classical sGRB (Nakar 2007, Fong et al.

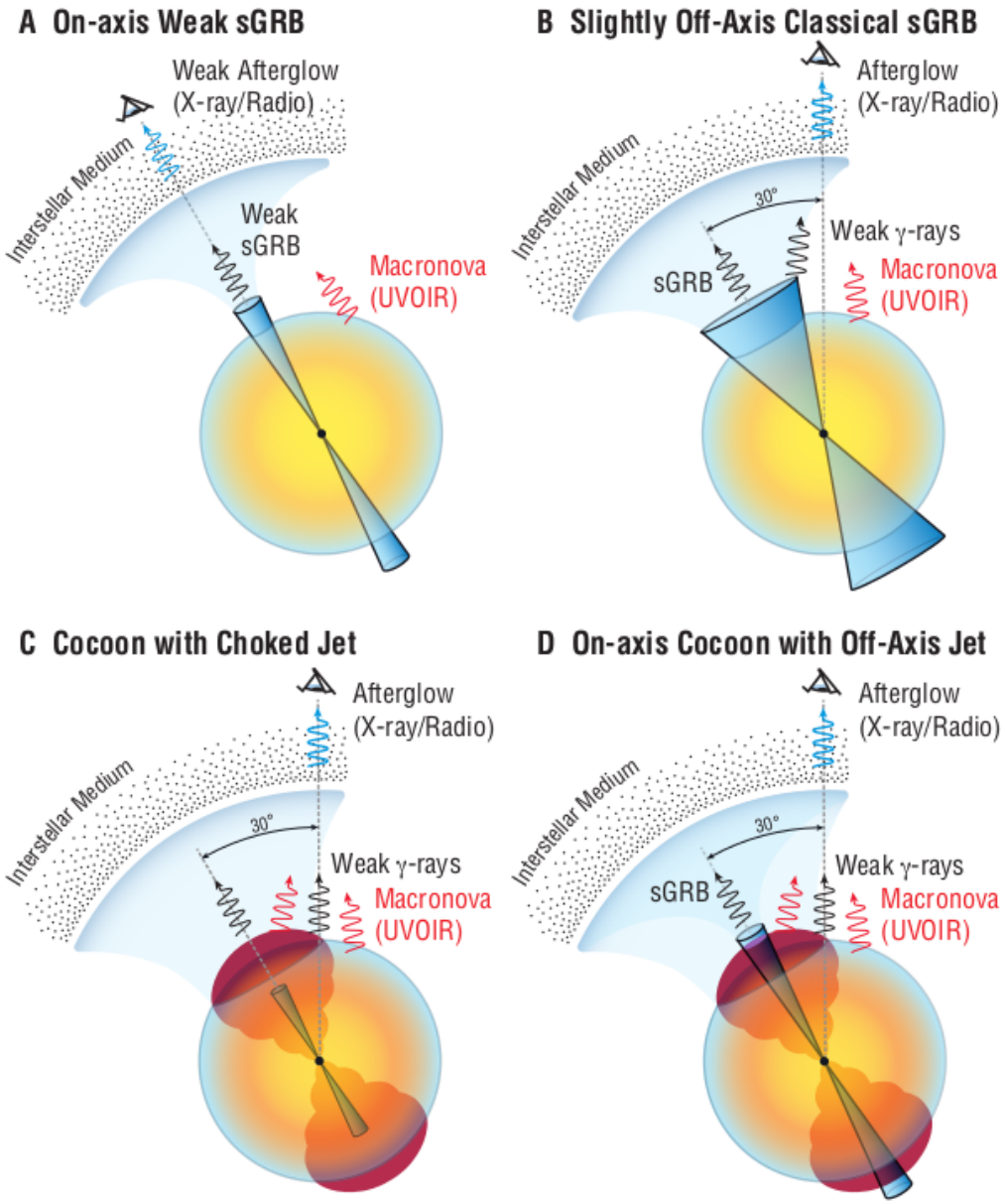

Figure 4.2: In each figure, the eye indicates the line of sight. Model (A) is a classical weak sGRB with an ultra-relativistic jet on-axis. Model (B) is a classical strong sGRB with an ultra-relativistic jet slightly off-axis. Model (C) is a mildly relativistic, wide angle, strong cocoon with a chocked jet. Model (D) is a mildly relativistic, wide angle, weak cocoon with a jet coming out from the lobe. Credit: Kasliwal et al. (2017).

2015). This could be explained by a weak sGRB. Nevertheless, Kasliwal et al. (2017) claim that the breakout of a narrow and ultra-relativistic jet would require $< 3 \times 10^{-6}$ $M_\odot$ of matter ejected in the direction of the jet itself. A wider opening angle would also allow less material for the breakout. However, the ultra-violet, optical and infrared (UVOIR) counterparts indicate the presence of much more mass (~ 0.05 $M_\odot$). This model also cannot explain the delay of X-ray (Evans et al., 2017) and radio emission (Hallinan et al., 2017) post-burst. Thus, this model has been ruled out (Kasliwal et al., 2017).

4.2.2.2 Classical off-axis short hard gamma-ray burst model

This model considers a classical sGRB of which the ultra-relativistic jet is off-axis and this means that the observer is not on the line-of-sight (Model B, Fig. 4.2). The gamma-ray luminosity decreases with the opening angle (Kasliwal et al., 2017) therefore the opening angle cannot be too wide ($< 8°$). This small off-axis orientation is not impossible but it is unlikely. Only ~5% of the sGRB have opening angles within these criteria (Kasliwal et al., 2017). Furthermore, this model cannot explain the X-ray and radio delay. Indeed, a sGRB consistent with this model should show a bright afterglow at every wavelength one day post-burst (Kasliwal et al., 2017) and this kind of afterglow was not observed. The Gamma-ray photons should also be harder at such low opening angle (Kasliwal et al., 2017).

The gamma-ray emission observed from the electromagnetic counterpart (EM170817) of GW170817 is hence different from the classical gamma-ray burst with ultra-relativistic jets (Kasliwal et al., 2017).

4.2.2.3 Cocoon breakout model

This model presents a relativistic jet launched after a brief delay due to a delayed hyper-massive neutron star collapse into a black hole (Falcke & Rezzolla 2014, Zhang 2014, Kasliwal et al. 2017). This process would imply the formation of a cocoon structure. Indeed, the jet would drill the ejecta and the material enveloping the jet would blow out and form the cocoon expanding outward at mildly relativistic velocity. There are two versions of this model: wide angle jet ($\sim 30°$) chocked, failed to drill out (Model C, Fig. 4.2) and narrow angle jet ($\sim 10°$) successfully drilling out with a classical sGRB if observed by an on-axis observer (Model D, Fig. 4.2) and narrow angle jet ($\sim 30°$).

If the jet drills out of the cocoon the radio and X-ray data can be explained with an off-axis jet (wide opening angle). If the emission is caused by the afterglow of a widely off-axis jet, it will slowly rise and then fade. If the emission is caused the forward shocks

of the cocoon, it is expected to rise. Regardless, we need the presence of a cocoon to explain the gamma-ray emission. The emission observed across the entire spectrum is consistent with the two cocoon models (Evans et al. 2017, Hallinan et al. 2017, Kasliwal et al. 2017). The cocoon scenario is hence the most likenly one.

4.2.2.4 GW170817 light curve

A power law was used to fit the light curve of the source (see Fig. 4.3) by Dobie et al. (2018). The power law given by the relation $S \propto \nu^{\alpha} t^{\delta}$ where S is the flux density, ν is the frequency, t is the time, δ is called temporal index and α is the spectral index. The radio light curve initially rises and peaks at 149 ± 2 days with a following decline. There is no steep rise which could be caused by a dominant off-axis jet Nakar & Piran (2018) but it is still possible to have a weaker jet. The sharpness of the peak indicates that the energy injection dramatically reduced or stopped (Dobie et al., 2018). This would be relevant for a successful jet (e.g. Kasliwal et al. 2017). In particular, Margutti et al. (2018) computed a synchrotron light curves simulation of a successful off-axis relativistic jet. The model properly reproduce the observations and predict a peak after 100 days post-merger. The sharpness of the light curve peak is also consistent with a low-energy choked-jet cocoon (e.g. Kasliwal et al. 2017, Mooley et al. 2018). Another model considers an isotropic fireball (e.g. Mooley et al. 2018). Dobie et al. (2018) ruled out a highly relativistic and quasi-isotropic outflow. Dobie et al. (2019) showed the light curve for the first 300 days (see Fig 4.3).

4.3 An alternative way for time series analysis in Astrophysics: State Space Models

4.3.1 The current method for time series analysis

Time variable and transient radio sources are identified using the following metrics. These are called modulation index m or V and weighted reduced χ^2 or η (e.g. Swinbank et al. 2015, Rowlinson et al. 2019, Murphy et al. 2021). These metrics were also used in Chapter 3 and are defined below:

$$V = \frac{1}{\overline{S}} \sqrt{\frac{N}{N-1} (\overline{S^2} - \overline{S}^2)}, \tag{4.1}$$

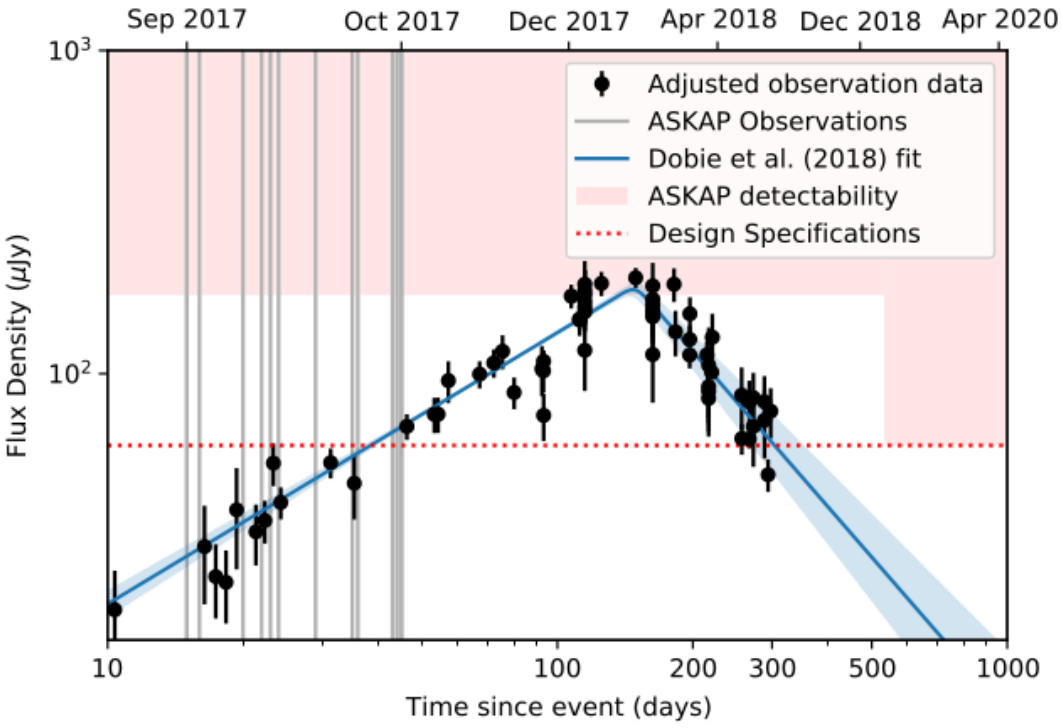

Figure 4.3: GW170817 radio light curve of the first 300 days. The data are scaled to 1.4 GHz given a spectral index $\alpha = -0.58$ ($S \propto \nu^{\alpha}$). The blue fitting line with the shaded uncertainties region is the power law from Dobie et al. (2018). Credit: Dobie et al. (2019).

$$\eta = \frac{N}{N-1}\left(\overline{wS^2} - \frac{\overline{wS}^2}{\overline{w}}\right), \tag{4.2}$$

where N is the number of measurements, S is the flux density value of a single measurement, $\overline{S}$ is the average flux density, $\overline{S^2}$ is the average square flux density, $\overline{S}^2$ is the square average flux density, and w is the weight defined as

$$w = \sum_{i=0}^{N} \frac{1}{\sigma_i^2}, \tag{4.3}$$

where σ_i is the error of the ith flux density measurement. Therefore, $\overline{wS^2}$ is the average of the weights multiplied by the square of flux density measurements for each source and $\overline{wS}$ is the average of the weights multiplied by the flux density measurements.

In a sample of sources, variables are objects having metrics above a threshold value. An example is shown in 4.4, where variables are defined beyond a 2σ threshold from a distribution fitted with a Gaussian function.

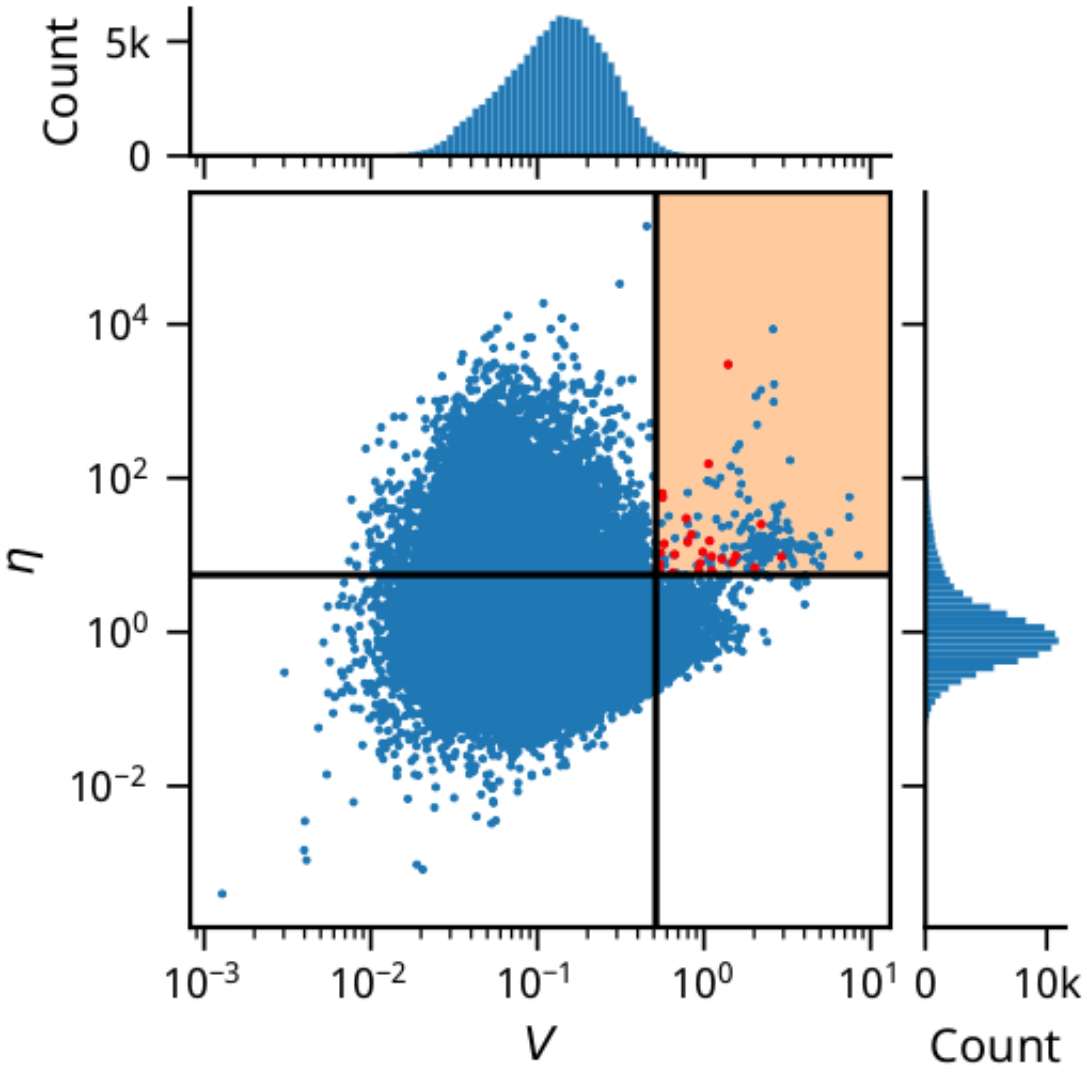

Figure 4.4: Plot of the two variability parameters for the radio sources of the VAST Pilot Survey Phase I (Murphy et al., 2021). Sources in the yellow region are classified as variables. These variables exceed 2σ for each parameter distribution, fitting a Gaussian function. Credit: Murphy et al. (2021).

The modulation index m indicates the variability degree and the weighted reduced χ^2 the variability significance. These metrics give a "summary statistic" of the time series but do not give statistical information of the time evolution of the system.

A future possible method for selecting variables involves the usage of a class of statistical models used for time series: the Space State Models (also called Dynamic Linear Models).

4.3.2 Introduction to State Space Models

Time series models can be univariate or multivariate. The former only have one variable (Brooks, 2008) whereas the latter have more than one variable (Wei, 2019). Notice that all the models presented in this Chapter are univariate time series models. In particular, Univariate State Space Models are based on two conditions (Tusell, 2008):

- the presence of a latent or hidden process x_t named the state process at the time t, here the value of x_t does not depend on x_{t-1} and x_{t+1};
- the presence of observations y_t that are independent given the the states x_t.

To better understand the conditions explained above we can consider a simple example of a space state model which is called **Local Level Model**. This can be expressed with the two equations below (Tusell, 2008):

$$y_t = \mu_t + \epsilon_t, \qquad \epsilon_t \sim N(0, \sigma_\epsilon^2), \tag{4.4}$$

$$\mu_{t+1} = \mu_t + \xi_t, \qquad \xi_t \sim N(0, \sigma_\xi^2), \tag{4.5}$$

where y_t is the observation at the given time t. If we were analysing the light curve of an astronomical source, y_t would be the flux density. The *level component* μ_t can be seen as the intercept of the function over time. The term ϵ_t is the *irregular component* that is an observation disturbance. It represents the error to add on the signal. Finally, ξ_t is called the level disturbance as it can be seen as the error associated with the *level component*. The two disturbance terms have a normal distribution centered on 0 as shown by the notation $N(0, \sigma^2)$ in equations 4.4 and 4.5.

The local level model satisfies the two criteria required to have a State Space Model: the presence of a latent process and independent observations. The flux density measurements y_t are the observations which are measured directly. The latent process is given by μ_t which is the intercept for each value of flux density at a given time t. We do not measure this term directly.

We can use this model to fit a light curve as shown in Fig. 4.5, where the gravitational wave event GW170817 (Dobie et al., 2019) has been fitted. In this case, using the Local Level Model, I added a 95% confidence region within I guarantee there is observation with a 95% probability. Every modelled observation at a given time t has been estimated based on the value of the previous one at the time $t-1$. Most measured data points are nearby the blue line of the model and inside the confidence region, therefore, this is a good fit. This model can hence be used to find other transients with the same physical origin and to extract physical parameters from the time series. For example, we could extract the gradient to derive the rise phase gradient and thus the physical parameters of the explosion / merger. In addition, the Local Level Model is only one of several state space models that we can use to identify sources of interest, and I will explore these models next.

4.3.3 Fitting GW170817 radio light curve with State Space Models

State Space Models may be applied not only to candidate FRB radio afterglows (see Section 4.1) but any other kind of transients and variables. In this Section, I will show the application of State Space Models to the gravitational waves event GW170817. While Dobie et al. (2018) adopted a power law to fit the light curve, I have used more advanced statistical models which can provide a better description of the flux density behaviour over time.

4.3.3.1 Brief introduction on model selection criterion and heteroskedasticity

In this Section I shortly explain the statistics I adopted to test the models for fitting the GW170817 light curve. The statistics involves the Aikaike Information Criterion (AIC), the Bayesian Information Criterion (BIC), the Hannan-Quinn Information Criterion (HQIC) and the Heteroskedasticity (H).

The AIC provides a measurement of the model "goodness" with respect to the data and is defined by the following formula (Burnham & Anderson, 2004):

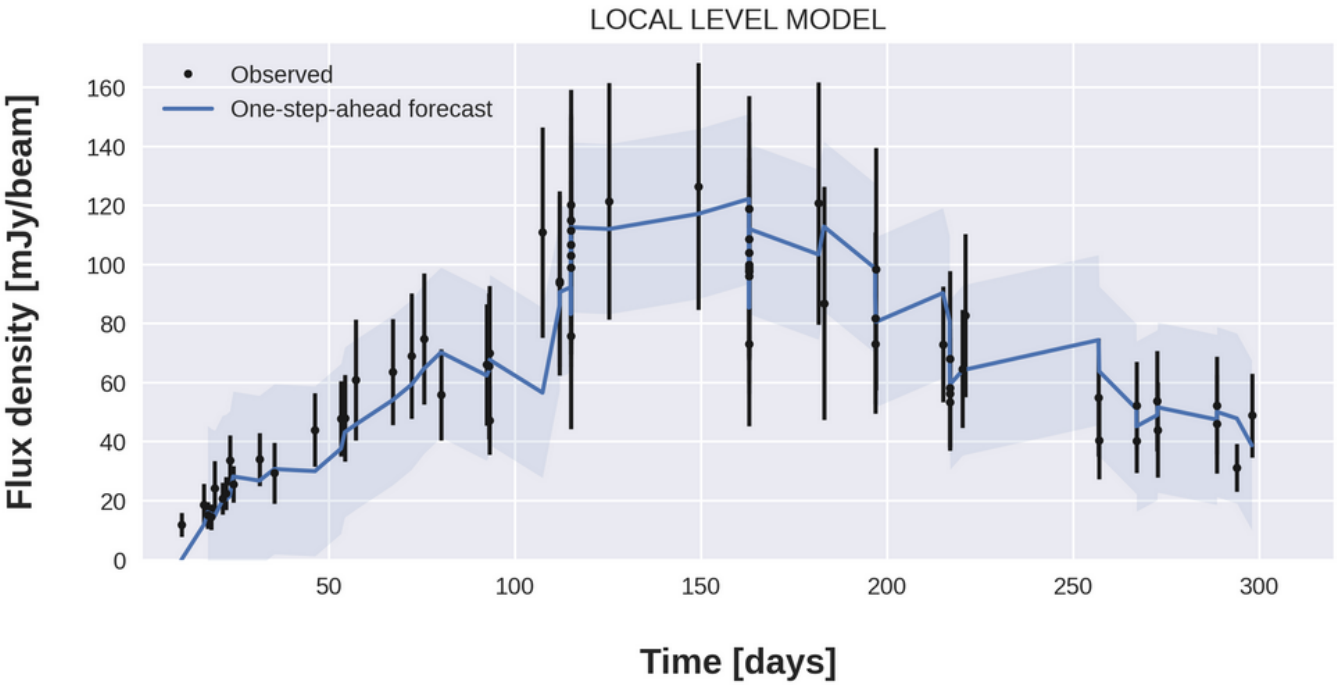

Figure 4.5: Local level model fitting GW170817 (Dobie et al., 2018). The black points (with their errors also in black) are data from Dobie et al. (2018). The blue line is the modelled fit of the light curve. Every modelled value at the time t is estimated based of the value of the previous modelled value at the time $t-1$. Hence, the model is "one step ahead." The light blue area is the 95% confidence region. Obviously, the negative values included in the confidence region should be ignored.

$$\mathrm{AIC} = 2k - 2\ln L, \tag{4.6}$$

where L is the likelihood function which is the Joint Probability of our observations as a function of the parameters of the statistical model. Let us suppose we have a sample of observations y_t. The probability density function (PDF) of each observation is $f(y_i,\theta)$ where θ is a parameter of the statistical model. The likelihood function is given by

$$L(\theta) = f(y_1,\theta)\cdot f(y_2,\theta)\ldots\cdot f(y_n,\theta) = \prod_{n=1}^{N} f(y_i,\theta), \tag{4.7}$$

in eq. 4.7 we considered the case of one parameter θ but it is also possible to have more parameters. It depends on the model adopted. In our case the observations are the values of y_t in eq. 4.12. Instead, k is the number of parameters of the model.

The BIC is also called the Schwarz Information Criterion. It is a model selection criterion (likewise the AIC) and is defined by the relation (Burnham & Anderson, 2004):

$$\mathrm{BIC} = k \ln n - 2 \ln L, \tag{4.8}$$

where n is the sample size.

Another alternative for selecting models is the HQIC. This is formally defined as (Burnham & Anderson, 2002):

$$\mathrm{HQIC} = -2L + 2k \ln(\ln n), \tag{4.9}$$

lower values of AIC, BIC and HQIC implies a better statistical model to represent the observed data. I will compare the values of these three parameters among different models later in this chapter.

The Heteroskedasticity (Barreto & Howland, 2006) gives an estimation of the conditional variance ($Variance(y|X)$) which is the variability of the observed data y_t for each value of the variable X or time t. We have a heteroscedastic data set when the standard deviations σ of a predicted variable y are not constant over an independent variable X or time t. This implies that the absolute residuals of the variable y are not constant over the variable X or the time t. The residuals are the difference between the predicted values and the actual measurements of the variable y.

If the standard deviations and the absolute residuals were constant, we would see a homoskedastic data set. In Fig. 4.6 there is a comparison between a homoskedastic data set and a heteroscedastic one.

4.3.3.2 Testing time series stationarity

Before trying to fit GW 170817 light curve with statistical models, it is necessary to find out if the time series is stationary. Some models are indeed suitable to stationary time series only (see Section 4.3.3.6). A time series is stationary if the following conditions are satisfied as reported in the R packages web pages[2]:

- Constant mean μ over the time t.
- Constant variance σ over the time t.

[2] https://cran.r-project.org/web/packages/TSTutorial/vignettes/Stationary.pdf

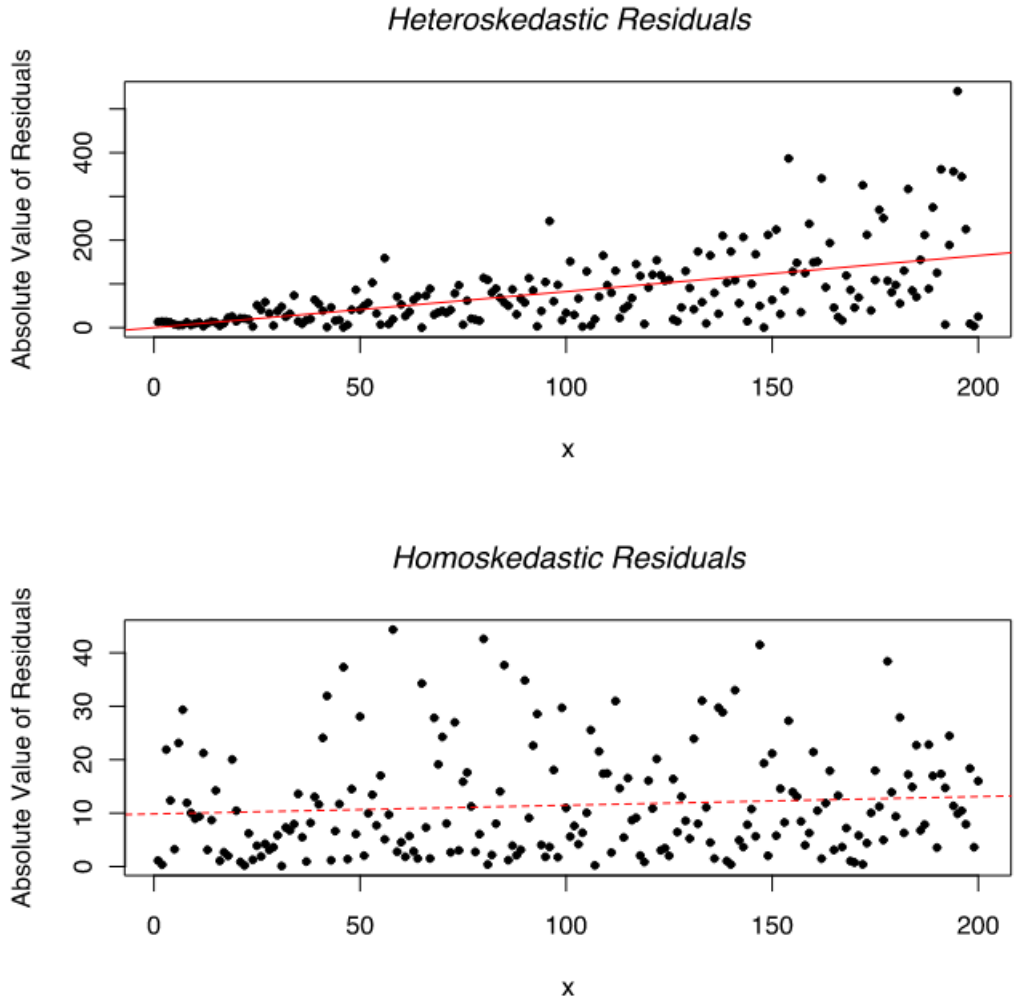

Figure 4.6: Example of heteroscedastic data set (top) and homoskedastic data set (bottom). The two plots show the behaviour of residuals vs. a variable X. The residuals are the difference between the predicted values (red fitting) and the actual measurements. Credit: The Free Encyclopedia. [1]

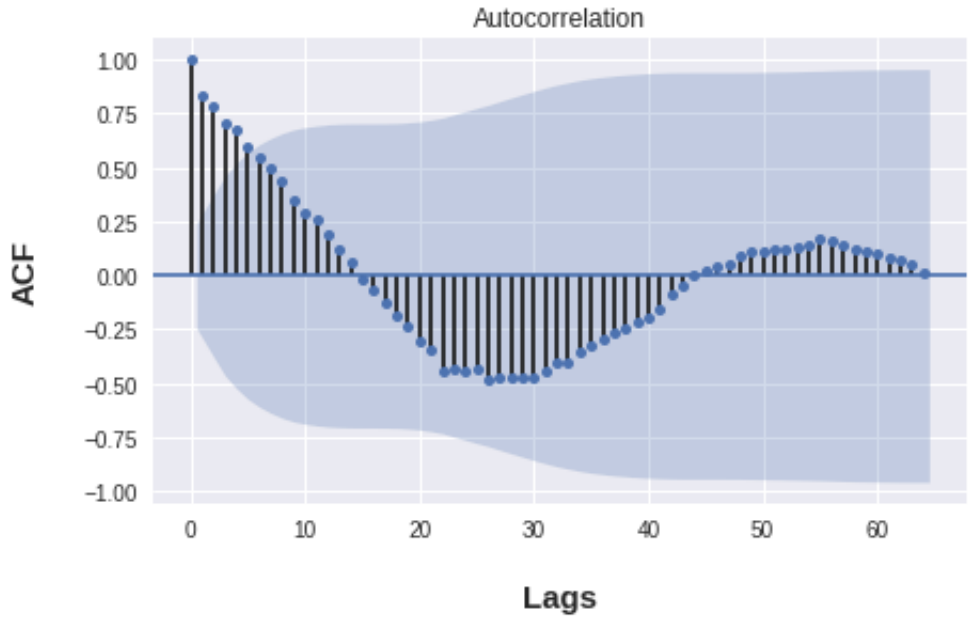

Figure 4.7: Autocorrelation function of GW170817 light curve.

- The Autocorrelation function (ACF) have a steep decline to 0.0.

To verify whether if GW170817 time series is stationary, I analysed its Autocorrelation function (ACF). This is a function giving the correlation between the value of the time series at given time t and the value of the same time series at the time $t-1$. In other words, we see the correlation between two flux density values y_t and y_{t-1}. The formula of autocorrelation is reported below (Shumway & Stoffer, 2017):

$$\text{ACF} = \frac{\sum_{t=k+1}^{T}(y_t - \bar{y})(y_{t-k} - \bar{y})}{(y_t - \bar{y})}, \tag{4.10}$$

where y_t is the flux density value at the time t, $\bar{y}$ while k is the number of lags. Every lag is the time interval between y_{t-1} and y_t. For $k = 1$ the autocorrelation is estimated between y_{t-1} and y_t while for $k = 2$ it is estimated between y_{t-2} and y_t and so on. Stationary time series have a dramatic decline around 0.0 and maintain this value for all lags (Shumway & Stoffer, 2017). The ACF in Fig 4.7 shows a different behaviour as does not keep a value near 0.0 for all lags.

I also used the Augmented Dickey-Fuller test to verify the stationarity of GW170817 time series. This test verifies the relation:

$$\Delta y_t = \delta y_{t-1} + u_t, \tag{4.11}$$

where u_t is a *random walk* which is a random shift from y_t. With eq. 4.11 we expect to have a non-stationary time series. The tests verifies that eq. 4.11 is actually correct ("null hypothesis"). The python library *statsmodels* calculates the p-value of the test. The p-value provides the probability to determine if there is evidence for rejecting the null hypothesis (Shumway & Stoffer, 2017). If the p-value is above a critical value we cannot reject the null hypothesis (Shumway & Stoffer, 2017). I obtained a p-value of 0.4 and three critical values: -3.5 (with a confidence level of 99%), -2.9 (with a confidence level of 95%) and -2.6 (with a confidence level of 90%). The critical values were also provided by *statsmodels* in Python. Because the p-value is above the critical value, we cannot reject the hypothesis the time series is non-stationary.

4.3.3.3 Local Level Model

I briefly described this model in Section 4.3.2. In Fig. 4.5 we can see the model fitting the GW170817 light curve. In the legend of the graph the model is described as "one-step-ahead forecast." As mentioned in Section 4.3.2 every modelled observation at a given time t has been estimated based on the value of the previous one at the time $t-1$. We can see this from eq. 4.14. Hence, the forecasting acts on the level component rather than the observation. Note that there is no confidence region for the first data point in time as the model is one-step-ahead.

In general, models can be "N-step-ahead." In other applications (e.g. finance, market) it is necessary to predict the behaviour of time series with many steps in advance. This would happen when we only have data points up to a time t and we do not have data points at $t' > t$. However, for our purposes forecasting one step only is suitable as we have all the data points we need. We just need to fit the time series.

By using the python library *statsmodels*, I retrieved the estimation of the Aikaike Information Criterion (AIC), the Bayesian Information Criterion (BIC), the Hannan-Quinn Information Criterion (HQIC) and the Heteroskedasticity (H) as well as the parametric model of the time series. The values of the parameters are in Table 4.1.
The model successfully fits the observed the data as we can see in Fig. 4.5.

4.3.3.4 Local Linear Trend Model

By adding a slope term ν_t to the Local Level Model, we obtain the Local Linear Trend Model (Koopman & Durbin, 2012):

Table 4.1: The following statistical parameters for the Local Level Model are listed: Aikaike Information Criterion (AIC), Bayesian Information Criterion (BIC), Hannan-Quinn Information Criterion (HQIC) and Heteroskedasticity (H).

Statistics	Value
AIC	531.8
BIC	538.2
HQIC	534.3
Heteroskedasticity (H)	2.6

$$y_t = \mu_t + \epsilon_t, \qquad \epsilon_t \sim N(0, \sigma_\epsilon^2), \tag{4.12}$$

$$\mu_{t+1} = \mu_t + \nu_t + \xi_t, \qquad \xi_t \sim N(0, \sigma_\xi^2), \tag{4.13}$$

$$\nu_{t+1} = \nu_t + \zeta_t, \qquad \zeta_t \sim N(0, \sigma_\zeta^2), \tag{4.14}$$

the term ν_t is a slope term generated by a random walk. A random walk is a time series model where the next observation y_{t+1} equals the previous one y_t with a random step up or down. In the same way as ϵ_t and ξ_t, ζ_t is a disturbance term normally distributed. The model can also be written in the following matrix form (called state space form):

$$\mathrm{y}_t = \begin{vmatrix} 1 & 0 \end{vmatrix} \begin{pmatrix} \mu_t \\ \nu_t \end{pmatrix} + \epsilon_t \tag{4.15}$$

$$\begin{pmatrix} \mu_{t+1} \\ \nu_{t+1} \end{pmatrix} = \begin{vmatrix} 1 & 1 \\ 0 & 1 \end{vmatrix} \begin{pmatrix} \mu_t \\ \nu_t \end{pmatrix} + \begin{pmatrix} \epsilon_t \\ \zeta_t \end{pmatrix} \tag{4.16}$$

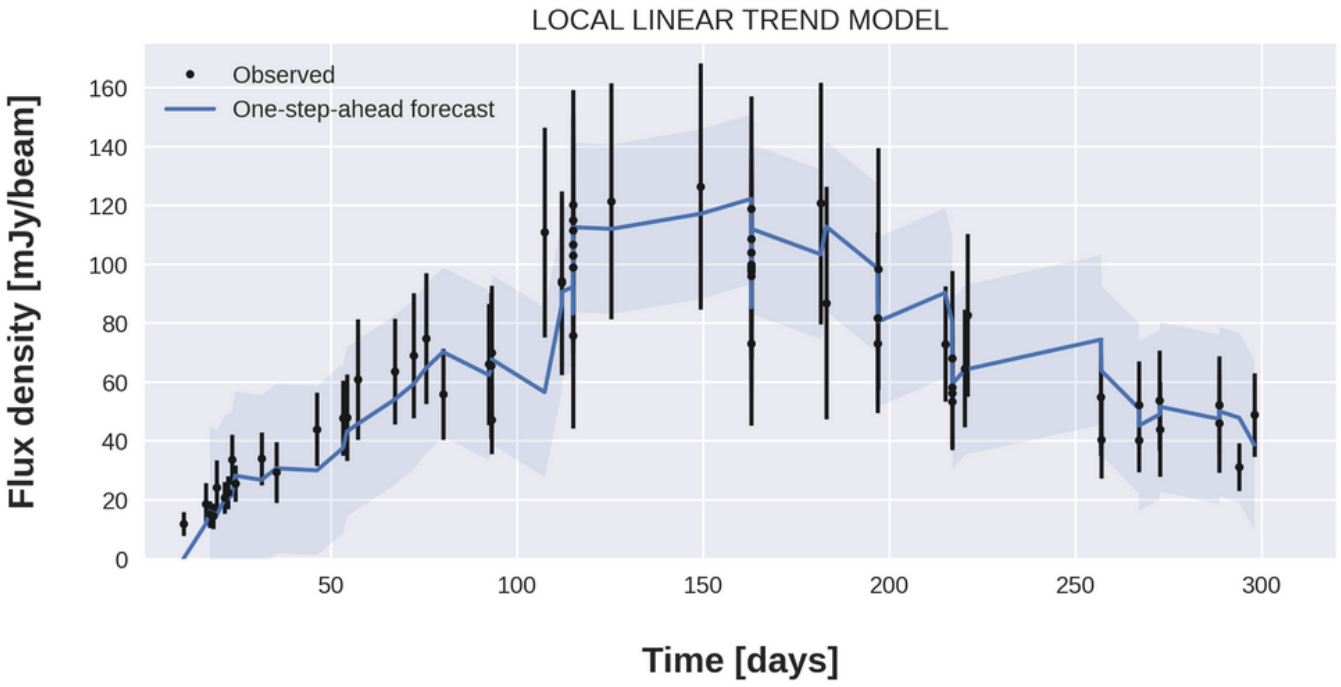

Figure 4.8: Local Linear Trend Model fitting GW170817 (Dobie et al., 2018). The black points (with their errors also in black) are data from Dobie et al. (2018). The blue line is the modelled fit of the light curve. The light blue area is the 95% confidence region. Obviously, the negative values included in the confidence region should be ignored.

in Table 4.2 the values of the statistical parameters obtained by fitting GW170817 are listed. In Fig. 4.8 we can see the model fitting the data. This fitting may appear to be very similar to the Local Level Model one, however, the confidence region of the Local Linear Trend Model is wider. For each time series model, I estimated the difference between the lower limit and the upper limit of the confidence region. In Table 4.5 I reported the width of the confidence region for each model so that we can compare the effectiveness of each model.

4.3.3.5 Autoregressive State Space Model

Autoregressive (AR) models can be written as (Feigelson et al., 2018):

$$y_t = a_1 y_{t-1} + a_2 y_{t-2} + ... + a_p y_{t-p} + \epsilon_t, \tag{4.17}$$

Table 4.2: The following statistical parameters for the Local Linear Trend Model are listed: Aikaike Information Criterion (AIC), Bayesian Information Criterion (BIC), Hannan-Quinn Information Criterion (HQIC) and Heteroskedasticity (H).

Statistics	Value
AIC	533.9
BIC	540.4
HQIC	536.4
Heteroskedasticity (H)	2.8

where y_t indicates the observed data, a_1, a_2....a_p are coeffients, ϵ_t is a normally distributed random error and p is the order of the model. If $p = 2$, the model is:

$$y_t = a_1 y_{t-1} + a_2 y_{t-2} + \epsilon_t, \qquad \epsilon_t \sim N(0, \sigma^2) \tag{4.18}$$

In space state form the process is:

$$\mathrm{y}_t = \alpha_t \begin{vmatrix} 1 & 0 \end{vmatrix} \tag{4.19}$$

$$\alpha_{t+1} = \begin{vmatrix} a_1 & a_2 \\ 1 & 0 \end{vmatrix} \alpha_t + \begin{vmatrix} 1 \\ 0 \end{vmatrix} \eta_t \qquad \eta_t \equiv \epsilon_{t+1} \sim N(0, \sigma^2) \tag{4.20}$$

I tested different values for the p parameter (from 1 to 20). I have decided to fit an autoregressive model with with $p = 2$, as this was the value for which I found the lowest AIC, BIC and HQIC. The values of AIC, BIC, HQIC and heteroskedasticity are in Table 4.3. The model is able to fit the data efficiently (see Fig. 4.21).

Table 4.3: The following statistical parameters are listed: Aikaike Information Criterion (AIC), Bayesian Information Criterion (BIC), Hannan-Quinn Information Criterion (HQIC) and Heteroskedasticity (H). The model is an Autoregressive (p=2) State Space Model.

Statistics	Value
AIC	549.9
BIC	556.5
HQIC	552.5
Heteroskedasticity (H)	3.5

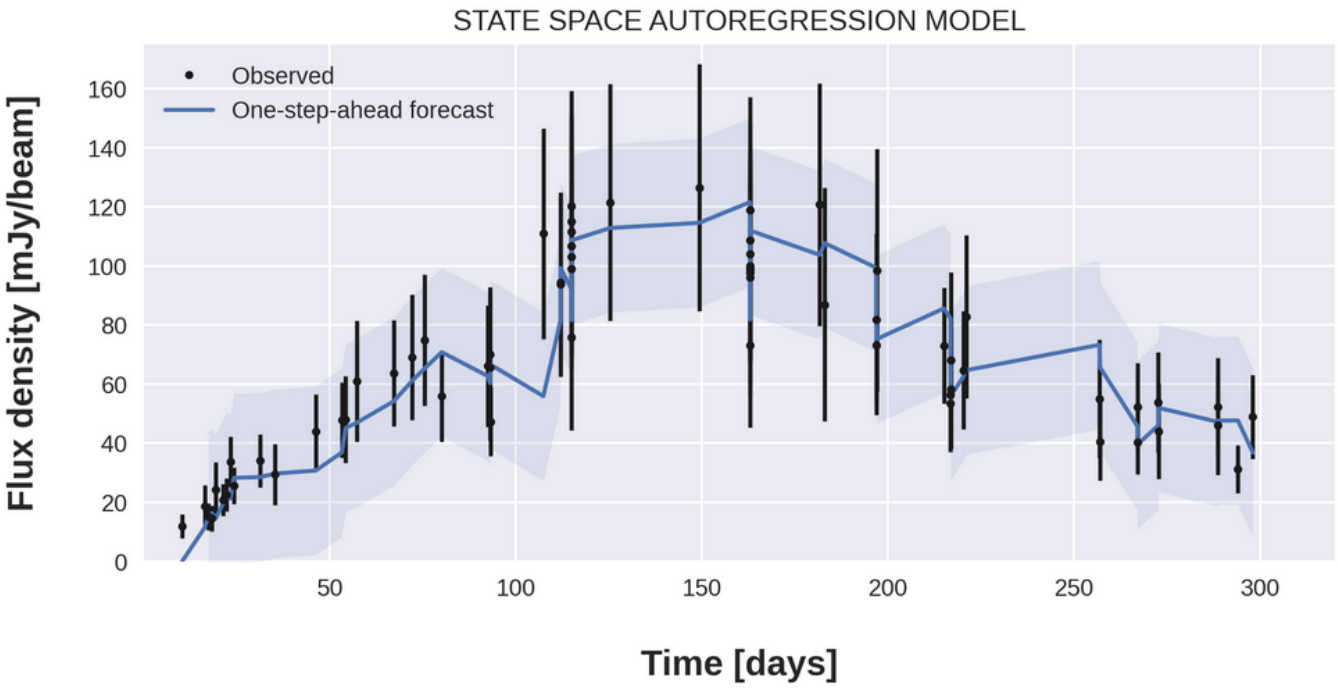

Figure 4.9: AR model in space state representation form (blue fitting and light blue confidence region) with GW170817 light curve (black points and black error bars).

4.3.3.6 State Space ARIMA Model

ARIMA models contain an autoregressive (AR) process (Feigelson et al., 2018) which can be written as:

$$y_t = a_1 y_{t-1} + a_2 y_{t-2} + ... + a_p y_{t-p} + \epsilon_t, \tag{4.21}$$

where y_t indicates the observed data, a_1, a_2....a_p are coeffients and ϵ_t is a normally distributed random error.

In ARIMA models a moving average (MA) process is also included (Feigelson et al., 2018) and is formulated as:

$$y_t = \epsilon_t + b_1 \epsilon_{t-1} + b_2 \epsilon_{t-2} + ... + b_q \epsilon_{t-q}, \tag{4.22}$$

where ϵ_t is the error term for the t-th time point, b_1, b_2....b_q are coefficients. The error terms are described as "random shocks." In the GW 170817 time series there is a rising trend up to 149 days (Dobie et al., 2018) and then a falling behaviour up to 300 days (Dobie et al., 2019). However, in the rising phase of the light curve (up to 149 days) we do not see that for all data points $y_t > y_{t-1}$. Every now and then, the light curve rises, declines, rise again and so on. There are much more rises than declines. The light curve is thus rising up to 149 days. When in statistical time series analysis, we see this combination of rises and declines, we talk about "shocks." In the GW light curve, there are also shocks between 150 and 300 days.

The two processes of autoregression (AR) and moving average (MA) result into ARMA models. In general, we talk about ARMA (p,q) process, where p and q are the orders of the AR and the MA process, respectively. ARMA models are suitable for time series with the assumption of stationarity. This means to have constant mean and variance at the beginning, middle and end of the data set (Shumway & Stoffer, 2017). This condition does not apply to GW170817 light curve. This is verifiable by analysing the time series but I also did two tests: the Autocorrelation function (ACF) analysis and the Dickey-Fuller test (see Section 4.3.3.2).

It is possible to remove the non-stationarity by differencing (Feigelson et al., 2018). In fact, we can replace the time series y_t with another y'_t that can be written as:

$$y'_t = y_t - B y_t = y_t - y_{t-1}, \tag{4.23}$$

Table 4.4: The following statistical parameters are listed: Aikaike Information Criterion (AIC), Bayesian Information Criterion (BIC), Hannan-Quinn Information Criterion (HQIC) and Heteroskedasticity (H). The model is a State Space ARIMA (1,2,1).

Statistics	Value
AIC	536.3
BIC	545.0
HQIC	539.7
Heteroskedasticity (H)	3.3

where B is called backshift operator (Feigelson et al., 2018). We can use a stationary ARMA process for the differenced time series. The original time series can be recreated by reversing or integrating the differenced time series. This process is called ARIMA(p,d,q) model where d is the number of differencing operations applied to the original time series (Feigelson et al., 2018). In eq. 4.23 this parameter is d = 1.

The model I used is an ARIMA model in state space form (Durbin & Koopman, 2012):

$$\Delta^2 y_t = \Delta(y_t - y_{t-1}), \tag{4.24}$$

$$y_t = \Delta y_t + y_{t-1} = \Delta^2 y_t + \Delta y_{t-1} + y_{t-1}, \tag{4.25}$$

where Δ is the differencial operator. The model that I applied is a State Space ARIMA (1,2,1) which is also called SSARIMA (1,2,1). I chose the values of the three parameters p,d,q by comparing the AIC, BIC and HQIC for different ARIMA models with various configurations of p,d,q. I found that the AIC, BIC and HQIC increase for p>1 and/or q>1 and/or d<2. The simple ARIMA model with no state space representation also gave higher values.

The statistical analysis of the State Space ARIMA (1,2,1) model gave the numbers reported in Table 4.4. In Fig 4.10 we can see that the model properly fits the observed data.

4.3.3.7 Best model selection

I tested four state space models: Local Level Model (LLM), Local Linear Trend (LLT), State Space Autoregression (AR) Model and SSARIMA (1,2,1).

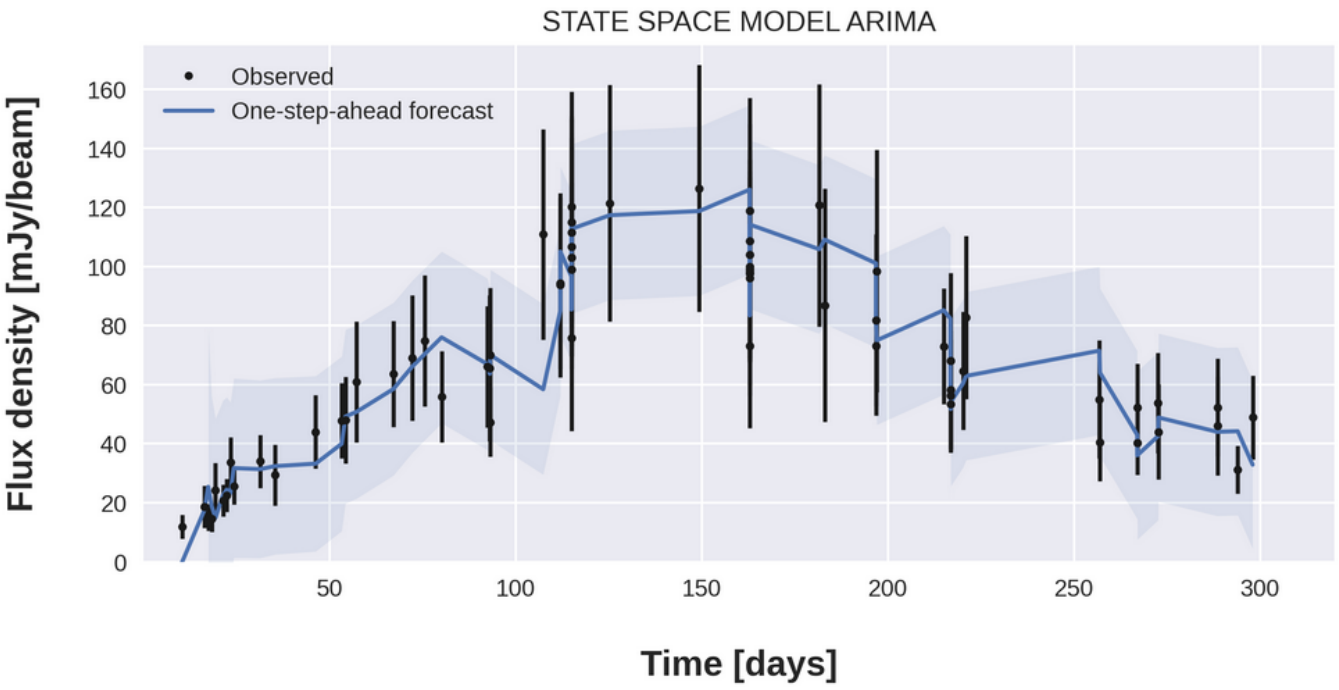

Figure 4.10: ARIMA model in space state representation form (blue fitting and light blue confidence region) with GW170817 light curve (black points).

Table 4.5: Confidence region width of the five models adopted: Local Level Model (LLM), Local Linear Trend (LLT) Model, State Space AR(2) Model, SSARIMA (1,2,1) and SSARIMA(2,1,1) with missing values. The first data point over time was not included for estimating these parameters.

Model	LLM	LLT	AR(2)	SSARIMA(1,2,1)
Width average	56.6	57.5	55.9	57.7
Max width	57.6	79.8	57.1	79.4
Min width	43.8	51.9	43.0	48.6
Width median	57.6	57.0	57.1	57.3

In Table 4.5 the width average, the maximum width, the minimum width and the width median of the confidence region for each model are reported. The four models have confidence regions with similar size. Note that I estimated these mean values without considering the first data point for the two models. Because in these models every value y_t is modelled considering the previous one y_{t-1}, the first data point always has a large confidence region which is not statistically relevant.

The model selection criteria and the heteroskedasticity values are reported in Ta-

Table 4.6: Statistical results of the four models adopted: Local Level Model (LLM), Local Linear Trend (LLT) Model, State Space AR(2) Model and SSARIMA (1,2,1).

Model	LLM	LLT	AR(2)	SSARIMA(1,2,1)
AIC	531.8	533.9	549.9	536.3
BIC	538.2	540.4	556.5	545.0
HQIC	534.3	536.4	552.5	539.7
Heteroskedasticity (H)	2.6	2.8	3.5	3.3

ble 4.6. The Local Level Model is the model with the lowest statistical values. This indicates that the Local Level Model is the most suitable model. However, before establishing that the Local Level Model is the best model, it is necessary to run detailed tests on the model residuals. This is explained in Section 4.3.3.8.

4.3.3.8 Model diagnostics

In this Section I test the goodness of fit of the Local Level Model on the data. I have already done this by comparing the Local Level Model with other models (see Section 4.3.3.7). Nevertheless, it is required to do other tests to further improve the model if necessary. I indeed did a residuals diagnostics.

Residuals in Univariate Space State Models are supposed to satisfy three properties (Tusell, 2008):

- independence;
- homoskedasticity;
- normality.

If at least one of these properties is not verified, some other model may be more suitable.

I verified that the residuals are independent with the plot of the Autocorrelation function of the residuals in Fig. 4.11. The residuals fall in the confidence region of the autocorrelation function which is given by the limits $\pm 1.96\sqrt{N}$. When the residuals are within this confidence region, the mean of the residuals is enough close to zero to state that there is no evident correlation in the residuals time series (Brockwell & Davis, 2010).

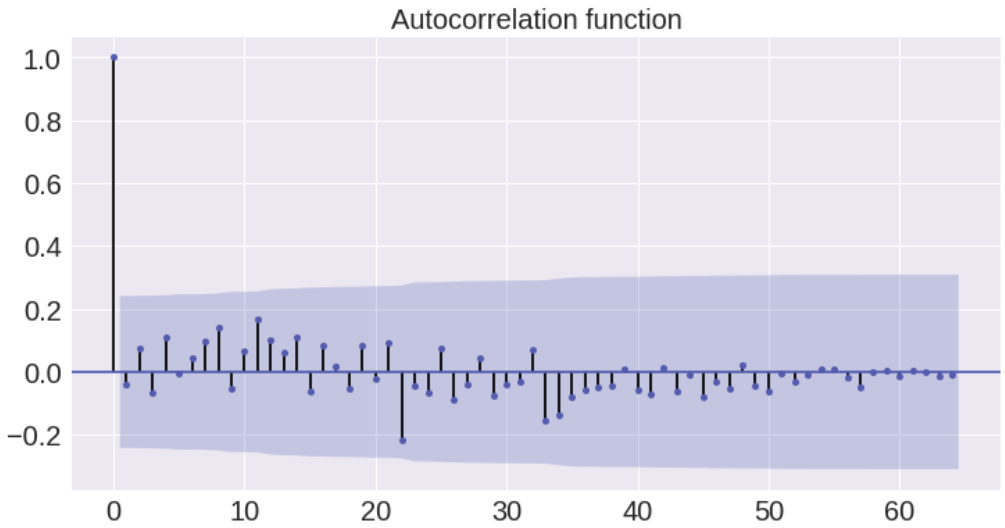

Figure 4.11: Autocorrelation function of the residuals from the Local Level Model. The blue area is the confidence region which is included in the interval $\pm 1.96\sqrt{N}$.

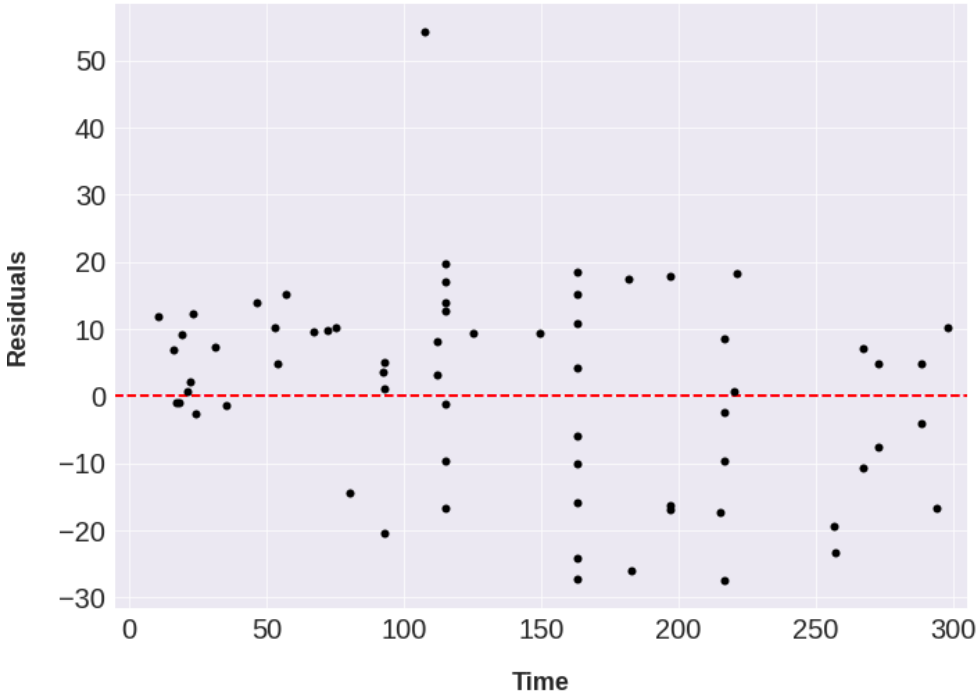

Figure 4.12: Residuals vs. time for the Local Level Model.

To satisfy the condition of homoskedasticity it is necessary to have residuals with constant variance. A simple check is a plot the residuals vs. time or responses. If the condition of homoskedasticity is satisfied, the spread of residuals vs. time needs to be roughly constant. The dispersion around 0 seems to increase from a time of 80 days (see Fig. 4.12). This is due to the presence of a residual value above 50. Apart from this large residual, all the other values are between -20 and 20. The trend is roughly constant. Residuals versus time were plotted even for the other time series models explored in this Chapter. The other models also showed a similar behaviour with a residual value much larger than all the others.

The data point causing this large residual was observed at 107.4 days. The data point is not even included in the confidence region of the Local Level Model (see Fig. 4.5). Interestingly, none of the time series models can fit this "critical" data point (see also Fig. 4.8, 4.21, 4.10). This data point is above 100 mJy and starts a sudden raise in the time series as the previous data point is below 80 mJy. In general, the one-step-ahead models examined in this Chapter, struggle on predicting sudden rises or declines. The observations following the critical data point are properly fitted by the all time series models. There is hence a sort of "delay" on fitting the first data point starting a sudden phase of rise or decline. In this case we have a rise.

In Fig 4.13 there is histogram of residuals fitted by a normal distribution. The residuals distribution is right-skewed with an excess of negative residuals on the left side of the plot. The other time series models also present the same behaviour. This may be caused again by the largest residual.

The analysis of a Q-Q plot is a more sophisticated method for verifying that the residuals follow a normal distribution (see Fig 4.14). A Q-Q plot is a graph of theoretical quantiles of a normal distribution with mean $\mu = 0$ and standard deviation $\sigma = 1$ (Koopman & Durbin, 2012). We also plot the sample quantiles. In this case the sample quantiles are the residuals. The Q-Q plot is a graph sample quantiles vs. theoretical quantiles (Koopman & Durbin, 2012). In Statistics and Data Science this plot is used to find the type of distribution of a random variable (see *Towards Data Science Web Pages*[3]). The residuals are the values of a random variable. If the points of the Q-Q plot fall on the straight line $y = x$, the residuals follow a normal distribution (Koopman & Durbin, 2012). Most points on the Q-Q plot follow this trend except the one with the largest residual (see Fig 4.14). I hence concluded that the residuals approximately follow a normal distribution.

[3] https://towardsdatascience.com/q-q-plots-explained-5aa8495426c0

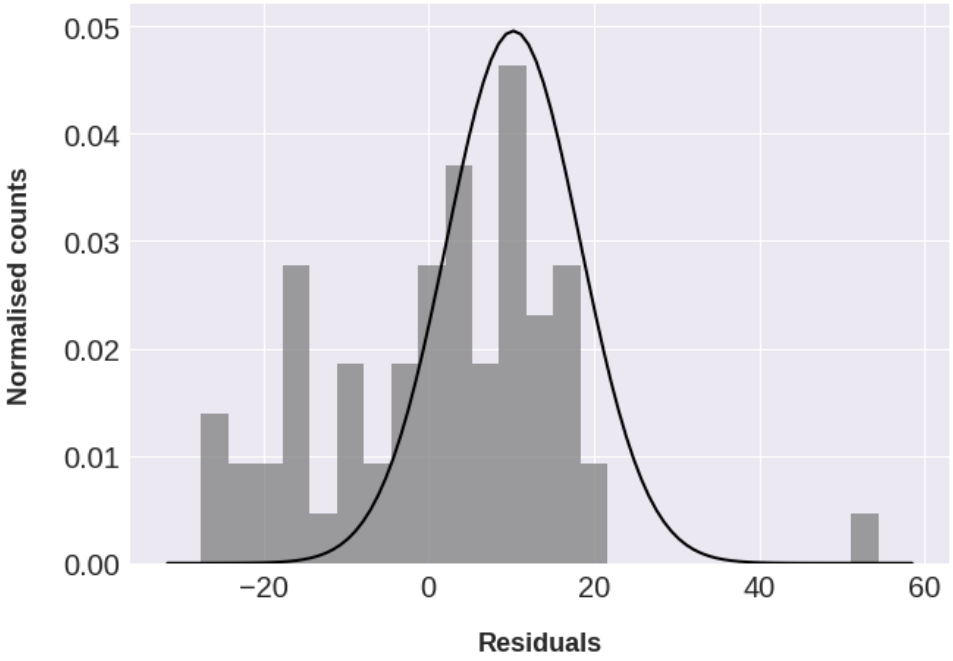

Figure 4.13: Plot of the residuals fitted a normal distribution (black fitting).

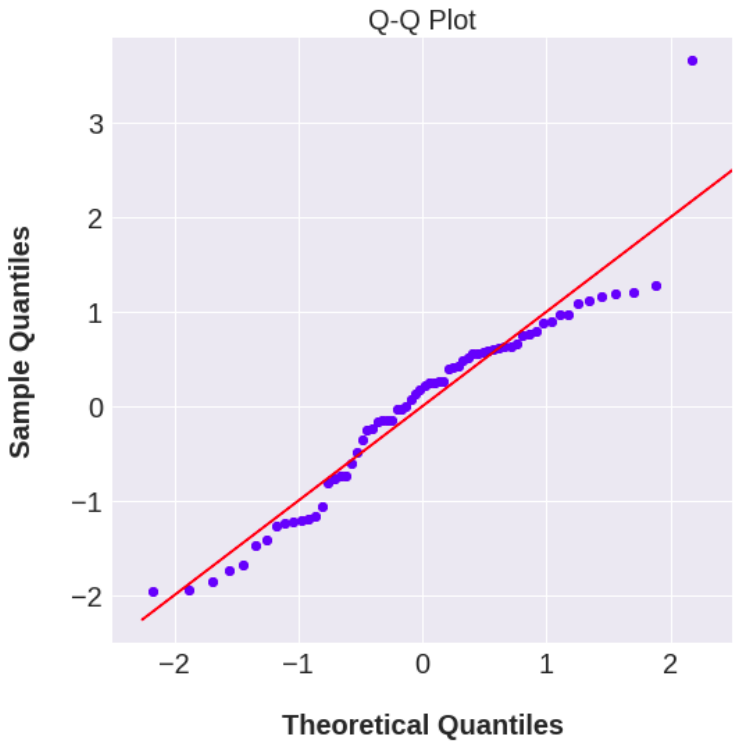

Figure 4.14: Q-Q plot of the residuals.

In summary, the residuals of the Local Level Model satisfies the conditions of independence, normality and homoskedasticity. Thus, the conclusion is that the Local Level Model is suitable for the GW170817 light curve.

4.4 Conclusions and possible developments

In this Chapter, innovative methods to analyse the variability of time series in Astrophysics were described and applied to the transient GW170817 light curve. The current metrics involving χ^2 and modulation index used in Astronomy, only provide an overall description of the variability. They do not give any description regarding the order of the data points. This is instead possible by using State Space Models. In detail, this study showed that it is possible to examine variability with several approaches. These methods and their possible developments are outlined below:

- Time series decomposition into components. An example is given by the SSARIMA model (1,2,1) used to fit the GW light curve. A moving average component describes a stochastic behaviour. A simple Local Level Model also provides a description about the trend of the time series between two data points thanks to the level component. This tells us if there is a decline, a rise or a flat trend in the time series for a given time t.

- Time series stationarity. Testing time series stationarity provides other information such as a constant or not constant mean of the time series. I remind the reader that the variance is the variability of the observed data y_t for each given time t.

- State Space Models that could allow the detection of transients even if hosted by another source such as a variable active galaxy. This is the same scenario of the fast radio burst FRB 150418 (Keane et al., 2016). State Space Models could indeed be used to detect bursts within an active galaxy and establish if a transient is detected or not. This kind of application with State Space Models will be shown in Chapter 5.

- State Space Models that also open the possibility of classifying different transient and variable sources. The Local Level Model successfully fits the gravitational wave event GW170817. This model is suitable for a sheer burst with a fast rise and decline. Other transients and variables with a different behaviour may need a different model. For instance, the flare star AT Mic in Chapter 2 presents a

main initial burst and then some secondary bursts. This might require a slightly different model, and hence for each transient class we may have a different model. State Space Models combined with supervised machine learning techniques of regression analysis (Liu, 2021) could be used for classifying transients.

- A further development with State Space Models could be in the direction of understanding physical processes. For instance, changes in the autoregressive behaviour and the moving average process may lead to a detailed description of the gravitational waves burst. The following questions could be faced: what physical phenomena cause the presence of shocks in the time series? What physical phenomena made necessary an autoregressive component AR = 2? Or in the case of the Local Level Model what physical events caused the presence of an irregular component? What is the cause of this disturbance in the time series? Feigelson et al. (2018) also highlighted that regression processes could be used to remove noise in astronomical observations.

- The State Space Models used in this Chapter, do not consider that the GW light curve is an irregularly spaced time series. This means that observations are not recorded with a regular time interval. In fact, in Astrophysics light curves are unlikely to be regular. In literature there are Models developed to better fit this kind of time series. These are time series models able to predict missing values (Durbin & Koopman, 2012). State Space Models taking into account missing values could allow to achieve better results.

CHAPTER 5

USING STATE SPACE MODELS FOR DETECTING GRAVITATIONAL WAVES

In Chapter 4 State Space Models were introduced and applied to the gravitational wave event GW170817. Now in this Chapter, the target is to show how State Space Models can detect a transient or gravitational wave within an active galaxy. Distinguishing between a transient signal and an active galaxy signal could be a complex task if the transient is within an active galaxy. I created a scenario where GW170817 is associated with a simulated AGN light curve and I used State Space Models to detect the burst from the transient source.

A similar case was observed in 2015, when a discovery of a fast radio burst afterglow was reported but was associated with an AGN (Keane et al., 2016). However, Giroletti et al. 2016b reported the radio variability was in fact due to the scintillating AGN itself and ruled out an FRB afterglow detection. Hence there is the ongoing problem of understanding if these candidate afterglows are a result of scintillation or really a true afterglow event.

Johnston et al. (2016) stated the development of new instruments would provide progress on this issue. On the other side, advanced models could solve the problem before a technological development. This is the goal of this Chapter.

5.1 The case of the fast radio burst FRB 50418

In 2015 a fast radio burst (FRB, Lorimer et al. 2007) was detected and was named FRB 50418 (Keane et al., 2016). The radio source was found within the galaxy WISE J071634.59−190039.2. Observations obtained with the Australia Telescope Compact Array (ATCA), the Karl Jansky Very Large Array (JVLA) and the Giant Metre-Wave Telescope suggested that this was the first detected afterglow of a FRB (Keane et al., 2016). An alternative hypothesis is that this source was in fact a scintillating AGN (e.g. Johnston et al. 2016, Williams & Berger 2016). It is important to distinguish these two different scenarios and State Space Models can help to achieve this.

In detail,Bassa et al. (2016) and Giroletti et al. (2016b) found a compact source in the optical galactic centre of the elliptical galaxy WISE J0716,àí190039.2. However, an evident connection with FRB 150418 was not found.

Johnston et al. (2016) considered two possibilities. In the first scenario the radio source is a scintillating AGN not associated with the FRB. In the second scenario the source is actually associated with the FRB. The authors stated that the variability observed from the galaxy WISE J071634.59−190039.2 is due to refractive scintillation as diffractive scintillation would imply variability timescales of about 10 minutes given the position of the source. The variability timescale observed is much longer (order of days). Johnston et al. (2016) has estimated the probability that the data are consistent with the shape of an intensity probability distribution function expected by refractive scintillation. For Johnston et al. (2016) the light curve of FRB 50418 (see Fig. 5.1) suggests the presence of a fading radio transient because of the high flux density value in the first epoch of the light curve. The probability to get such a high value is 0.3%. Johnston et al. (2016) also pointed out that scintillation is intermittent in compact AGN (Lovell et al., 2008) and the light curve is only sparsely sampled during the first few months. These arguments lead to a FRB in conjunction with a scintillating AGN as the most likely explanation. However, the possibility of a scintillating AGN not associated with a FRB is not ruled out. It is only considered as an unlikely scenario.

As already mentioned, the radio light curve of FRB 50418 is shown in Fig. 5.1. The light curve is comprised of data from ATCA, JVLA, the Very Long Baseline Array (VLBA), e-MERLIN and the European VLBI Network (EVN). All these observations are described by Johnston et al. (2016).

Williams & Berger (2016) instead rule out the presence of a transient source. The authors indeed state that the claimed radio transient is actually AGN variability. Williams

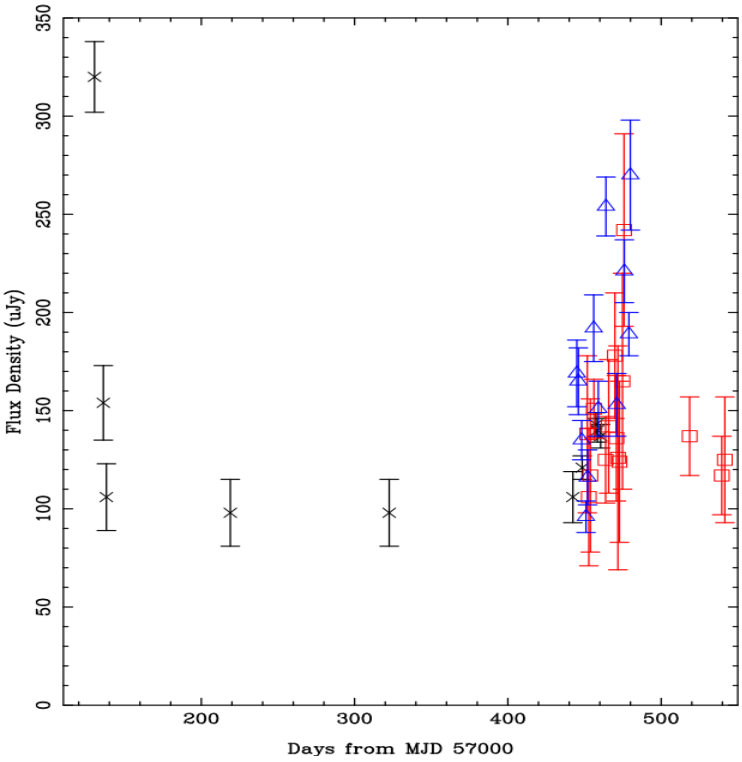

Figure 5.1: Radio light curve at 5.5 GHz of the source (FRB 50418) within the galaxy WISE J071634.59−190039.2. Black crosses are ATCA observations, blue triangles JVLA observations, and red squares VLBA, e-MERLIN and EVN. Credit: Johnston et al. (2016).

& Berger (2016) modelled the radio light curve using the GRB afterglow model of Granot & Sari (2002). The model was compared with a steady source modulated by refractive scintillation (RISS). The analysis shows a rapid spectral evolution (spectral index $\alpha \lesssim -3.4$ assuming a ν^{-1} spectrum) not expected by a synchrotron blastwave caused by a transient. Williams & Berger (2016) claim that this rapid spectral evolution can be due to an AGN flare. This is suggested by another object with a similar behaviour (VTC225411−010651) showing α increased from -1.7 to +0.4 over 15 days. In summary, Williams & Berger (2016) affirm that the light curve of the claimed transient is explained as a steady source affected by strong interstellar scintillation showing an AGN flare.

Williams & Berger (2016) also explain that Keane et al. (2016) consider the probability of finding an unassociated radio transient in their search field but not the probability of finding a variable radio source. The latter is not negligible.

The agreement between the redshift of WISE J071634.59−190039.2 and the dispersion measure (DM) of FRB 50418 could indicate the association of the two. Nevertheless, Williams & Berger (2016) run a Monte Carlo simulation and showed that this is not

unlikely if the host is a randomly selected radio variable.

The case of FRB 50418 opened a discussion with published manuscripts claiming the detection or the non-detection of a radio transient (e.g. Keane et al. 2016, Williams & Berger 2016) hosted by a scintillating AGN.

5.2 Detecting a gravitational waves event in a simulated host active galaxy

I reproduced a scenario of GW170817 associated with an active galaxy. The AGN light curve was reproduced with the same sampling of the GW time series extended by five cycles.

5.2.1 Conditions and scenarios for detecting transients within an active galaxy

The burst of a transient is visible if the host galaxy is much fainter than GW170817. I simulated an AGN light curve with a mean flux density of 30 mJy. Each associated error bar is 20% of its flux density measurement. In Fig. 5.2 there is a plot of the light curve.

On the other side, detecting a transient can be very difficult if the host galaxy is much brighter as shown in Fig. 5.3. The detection would not be possible unless we did observations with very good sensitivity and resolution which will be possible with the Square Kilometre Array (SKA[1]). The SKA will have 50 times the sensitivity of current imaging instrument with 5,000 M^2/K (400 μJy in 1 minute) between 70 and 300 MHz while the resolution will be < 0.1 arcsec.

In general, the detection of a transient hence depends on the mean brightness of the host galaxy. Nevertheless, a host galaxy with low mean flux density but high dispersion of the flux measurements would also complicate the detection. This is the case in Fig. 5.4. The associated errors are still 20% of their flux densities measurements. The mean flux density of the AGN is 30 mJy which is the same mean value of the scenario in Fig. 5.2. However, the dispersion of the data points is much larger. In this case the presence of a transient can be suggested by the lack of low flux measurements between 900 and 1200 days of observations.

Let us consider a scenario for which the AGN is not excessively bright and the mean flux density is not extremely low. Fig. 5.5 shows this scenario. The simulated AGN has

[1] https://www.skatelescope.org/the-ska-project/

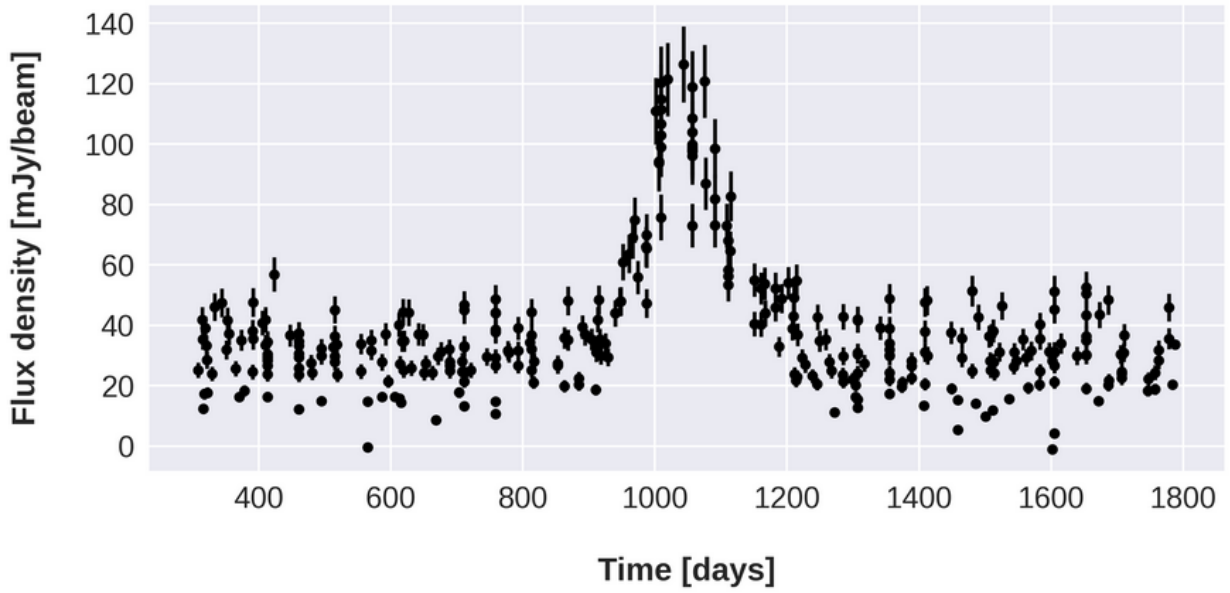

Figure 5.2: GW170817 hosted by a faint AGN. The transient source is between 1000 and 1200 days of observations. The host galaxy is much fainter than the gravitational waves source. It is then simple to detect a transient source.

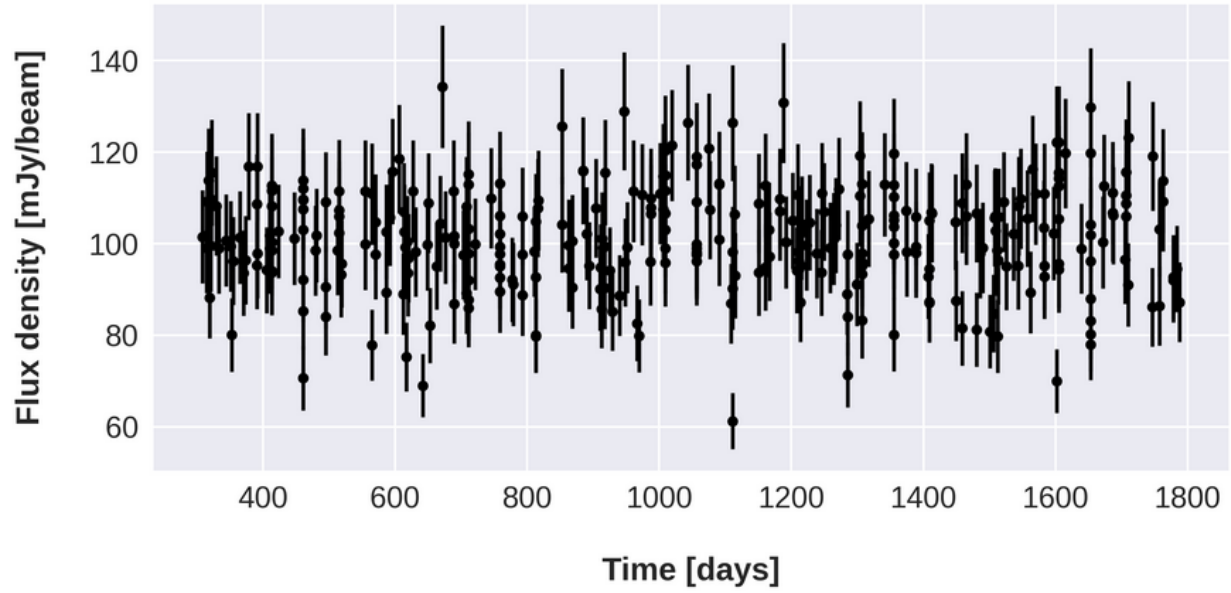

Figure 5.3: GW170817 hosted by a bright AGN. The transient source is between 1000 and 1200 days of observations. The brightness of the host galaxy is comparable the one of the transient. It is then very challenging to detect a transient source.

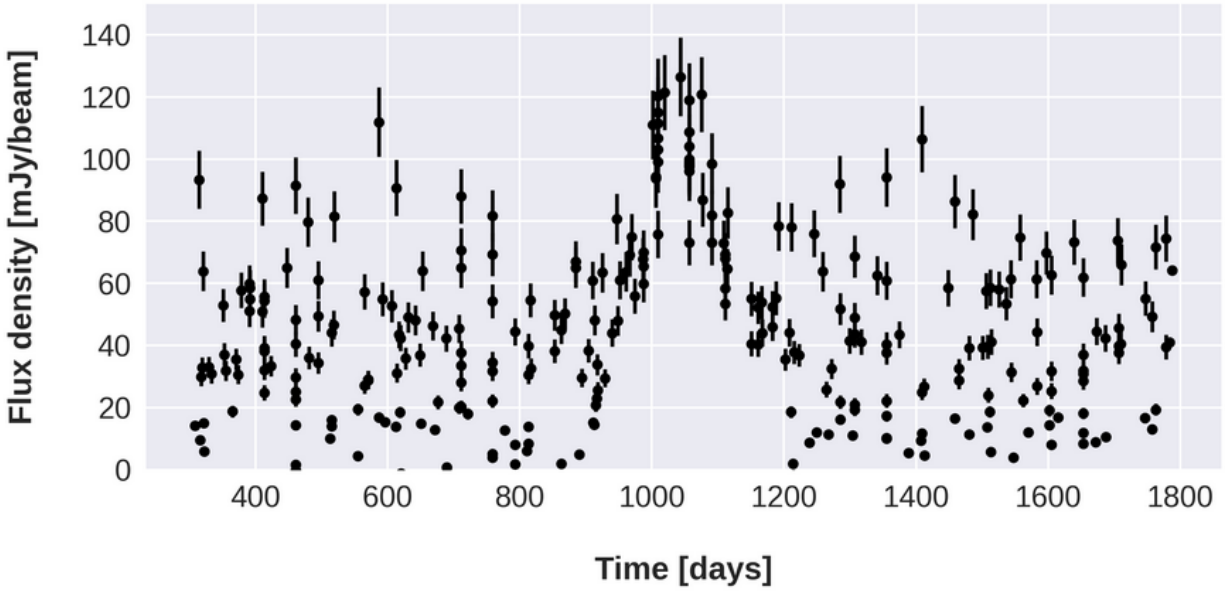

Figure 5.4: GW170817 hosted by a bright AGN. The transient source is between 1000 and 1200 days of observations. The mean brightness of the host galaxy is much lower than the one of the transient. However, there are a few measurements comparable to the ones of the transient.

flux density measurements between 40 and 120 mJy and a mean value of 80 mJy. The associated errors are still 20% of their flux densities measurements. Note that the larger the flux density for each AGN data point, the larger the error bars. This makes the detection of the transient source more difficult.

5.2.2 Using State Space Models for detecting transient signals

The detection of GW170817 can be made simpler thanks to a time series model for the AGN. I hence tested different time series models on the the AGN light curve. The models are the following: Local Level Model (LLM), Local Linear Trend (LLT) Model, State Space AR(3) Model and SSARIMA (3,1,25) and the result of their statistical performance is reported in Table 5.1. Note that these models are explained in Section 4.3.3.

The Local Level Model is the the model with the best parameters (see Table 5.1).In Fig. 5.6) we can see the model fitting the time series. Interestingly, the SSARIMA model can reproduce the stochastic behaviour of the time series (see Fig. 5.7).

Stochastic time series have several declines and rises between consecutive data points. ARIMA models are suitable to reproduce this behaviour. Rises and declines can indeed be fitted using a regression and a moving average process (see Section 4.3.3.6).

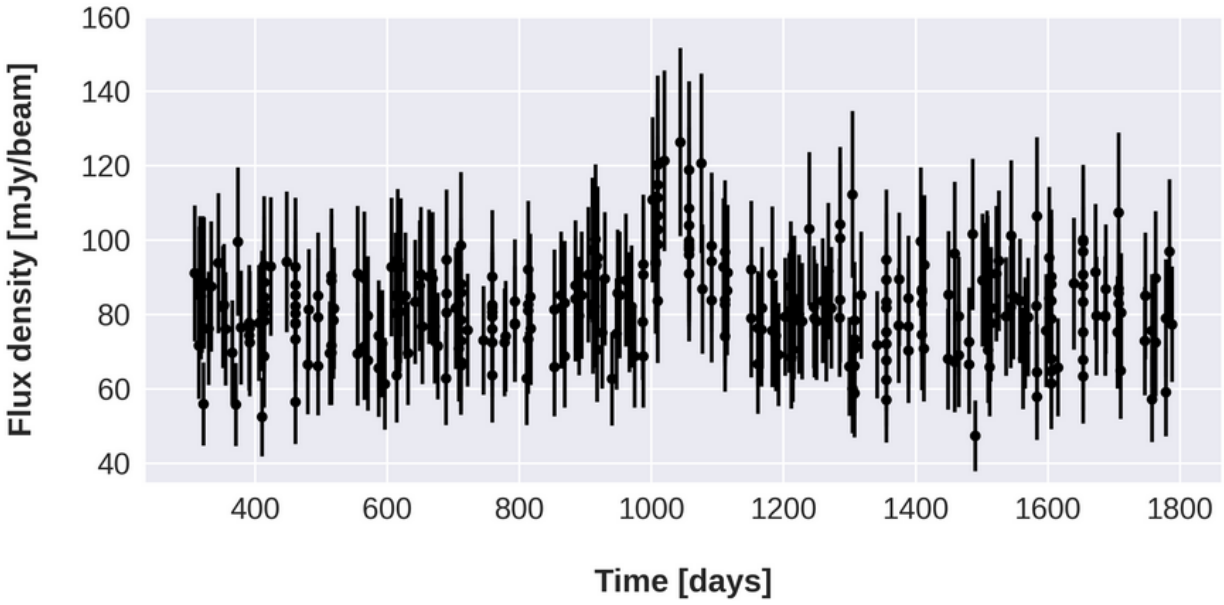

Figure 5.5: GW170817 hosted by a bright AGN. The transient source is between 1000 and 1200 days of observations. However, the presence of the source is not evident as it is within a variable active galaxy.

Table 5.1: Statistical results of the four models tested: Local Level Model (LLM), Local Linear Trend (LLT) Model, State Space AR(3) Model and SSARIMA (3,1,25).

Model	LLM	LLT	AR(3)	SSARIMA(3,1,25)
AIC	2536.5	2548.1	2558.7	2559.0
BIC	2547.9	2559.5	2577.7	2672.9
HQIC	2541.0	2552.7	2566.3	2604.5
Heteroskedasticity (H)	1.6	1.6	1.5	1.5

This is demonstrated by works in literature showing ARIMA models fitting AGN light curves (Bhattacharyya et al. 2020, Sarkar et al. 2020). In this case, the high moving average of 25 reproduces the local shocks in the time series while the regression order of 3 reproduces the global stochastic trend of the data. The values of the moving average and regression orders were chosen after testing integer values from 0 to 50. The values of 25 and 3 gave the best fitting and lowest statistical parameters (AIC, BIC, HQIC).

The data were also fitted by the autoregression model of order 3. With this model there is no a moving average component reproducing local shocks but the general stochastic trend is still reproduced. This model can also be described as the trend component of the

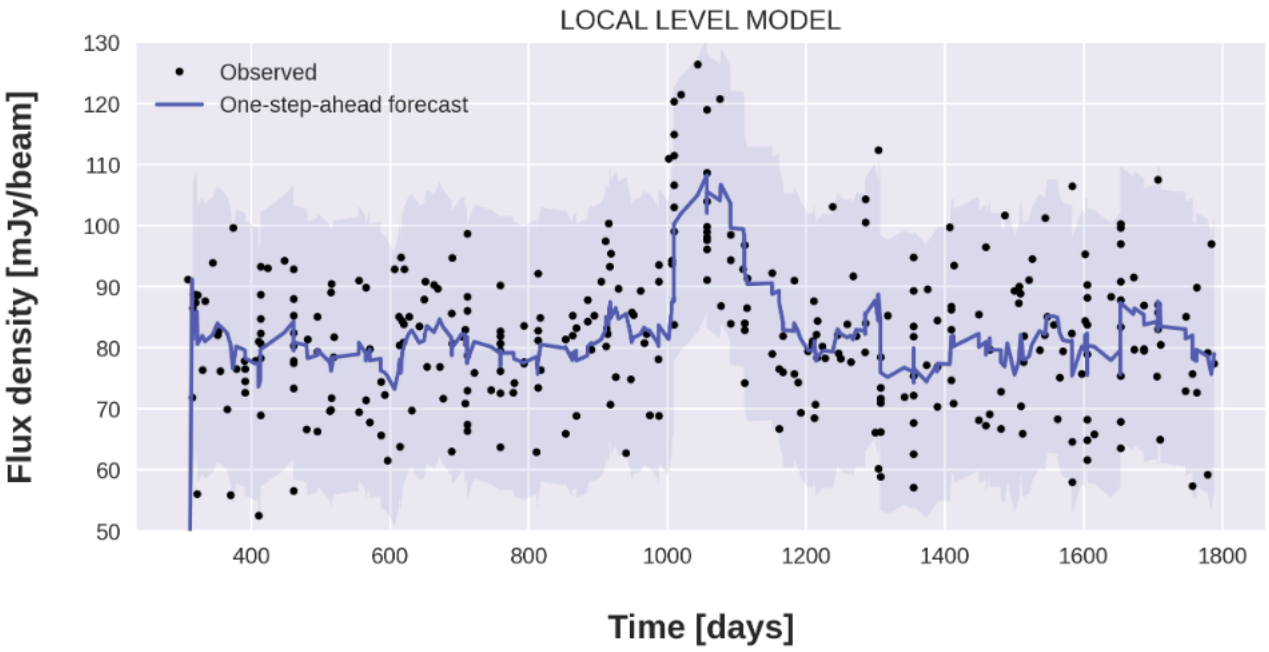

Figure 5.6: Local Level Model fitting the light curve. The error bars were omitted to clearly show the model fitting the data.

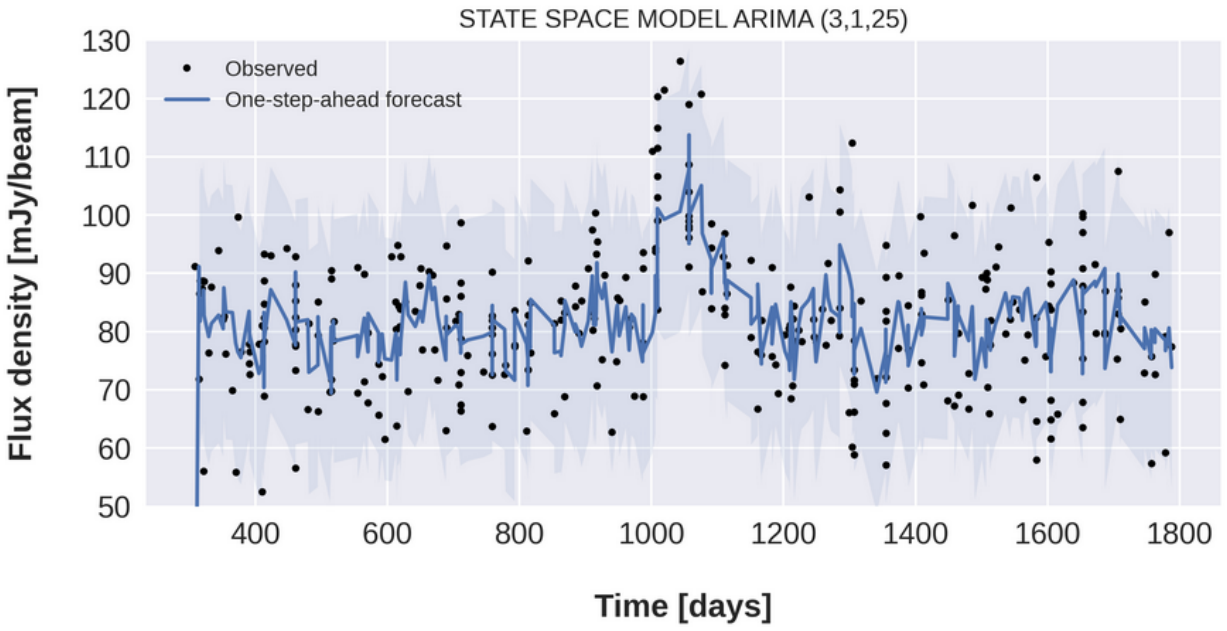

Figure 5.7: SSARIMA(3,1,25) model fitting the light curve. The light blue region is the 95% confidence region. The error bars were omitted to clearly show the model fitting the data.

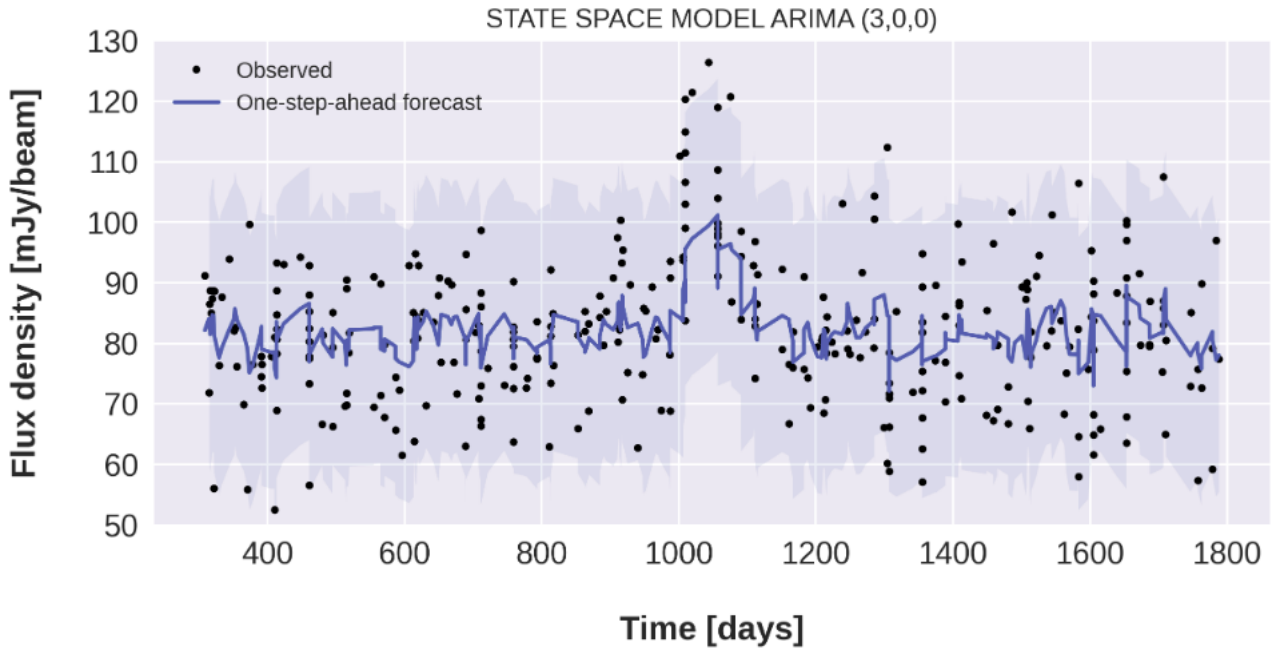

Figure 5.8: SSARIMA(3,0,0) model fitting the light curve. The light blue region is the 95% confidence region. The error bars were omitted to clearly show the model fitting the data.

SSARIMA(3,1,25) model (see Fig. 5.8).

Note that all the models fails on fitting the data points of the peak region of the light curve. This indicates a sharp change of the time series trend.

To detect a transient within the light curve in Fig. 5.5 it is necessary to analyse the trend of the time series which is successfully reproduced by the Local Level Model. If there is a detectable transient within the light curve, there must be a discrepancy between the time series model trend and the mean flux density value of the data. In Fig. 5.9 we can see that there is a large gap 1000 and 1200 days of observations. The trend model is mostly around the mean value of 82 mJy with a gap below 10 except for this time interval. The maximum gradient between the trend and the mean flux density is 26.16 after 1057 days of observations.

5.2.3 Change points search in time series

A method for detecting a transient within an active galaxy was proposed above. The light curve interval where the transient has been detected is approximately between 1000 and 1200 days. In this interval the flux density must be dominated by the transient source. This leads to the problem of understanding when the transient starts dominating, when

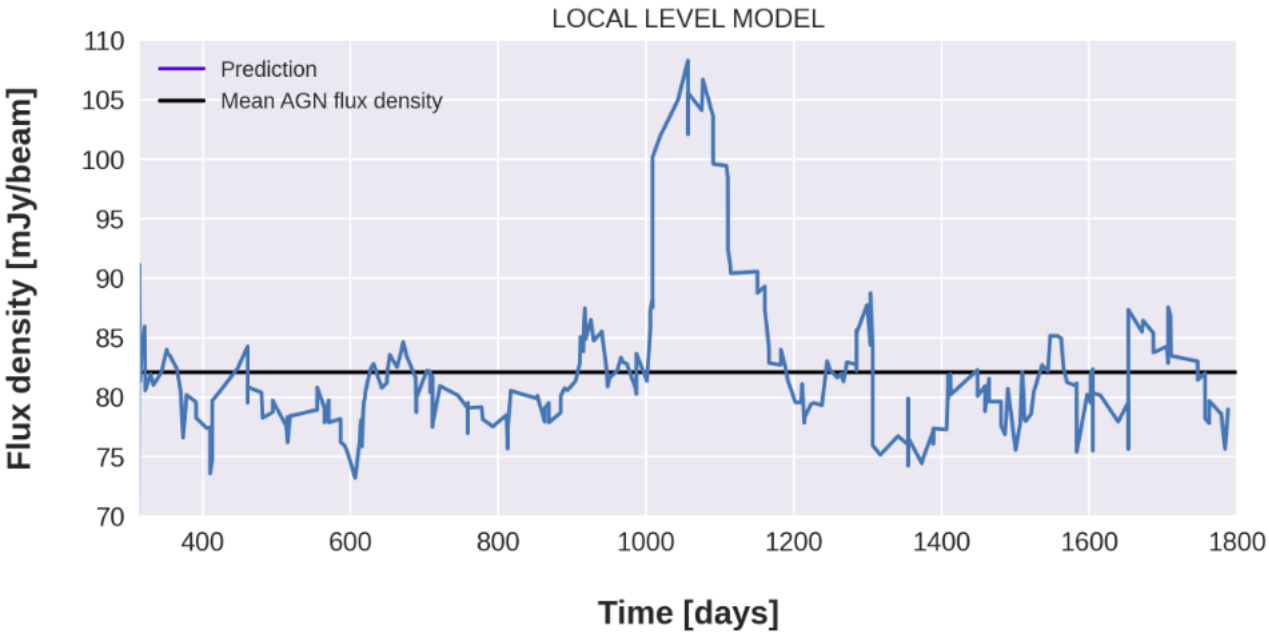

Figure 5.9: Local Level Model compared to the mean flux density. The blue trend is the prediction of the Local Level Model while the black line is the level of the mean flux density of the light curve.

it ends dominating and how long the burst dominates. In other words, we know that this interval is between 1000 and 1200 days but this is a rough indication. We do not know the exact time interval dominated by the transient. The solution is to detect change points in the time series **trend**.

A change point divides a time series in two segments where each segment has its own statistical characteristics such as mean and variance (Sharma et al., 2016). The statistical properties of each segment are different from the statistical properties of the other segment. In Fig. 5.10 there is an example of a change point in a time series.

To detect change points in the AGN light curve a Window-based change point detection method was applied. This method is based on the usage of sliding windows. A sliding window is a subset of n data points in the main time series. In detail, given a time series T of fixed length m (subset of the time series data stream) and x_t a series sample at time t, we can build a matrix W M of all possible subsequences of length k by moving a sliding window of size k across the main time series T (Aminikhanghahi, 2016). In Fig. 5.11 there is a representation of slide windows in time series.

The Window-based change point detection method consists of computing the discrepancy between two adjacent windows sliding along the signal y (Truong et al., 2020). Let

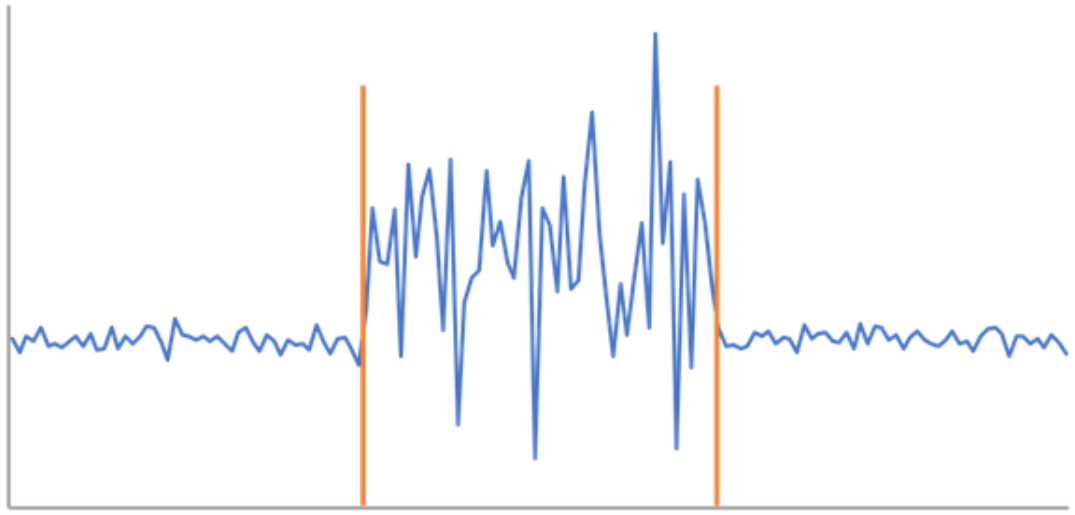

Figure 5.10: Example of change points in a time series. The change points are highlighted by the red vertical lines. The change points divides the time series into segments with different statistical characteristics (standard deviation in this case). Credit: webpages of Arc GIS Pro.[2]

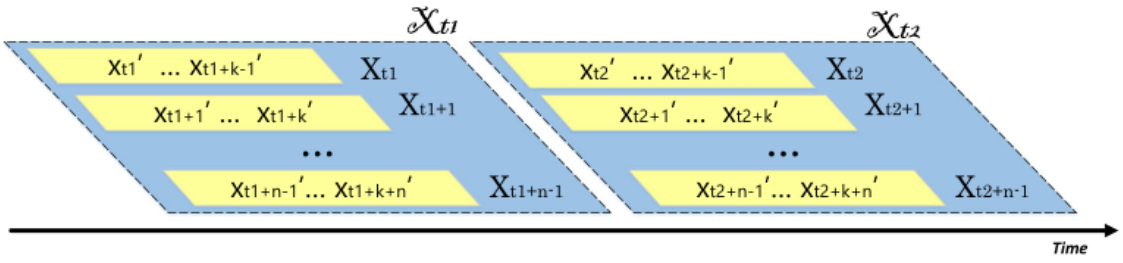

Figure 5.11: Illustration of sliding windows in time series. Credit: Aminikhanghahi (2016).

us consider two adjacent sliding windows as shown in Fig. 5.12.

The discrepancy between two sliding windows is given by the following formula:

$$d(y_{a\ldots t,b\ldots t}) = c(y_{a\ldots t}) - c(y_{a\ldots b}) - c(y_{b\ldots t}), \tag{5.1}$$

where d is the discrepancy, y is the signal, a, b and t define the time intervals covered by the two windows in Fig. 5.12. The function $c()$ is called cost function and is used to determine a difference of the statistical properties of the two subsets (windows) of the time series T. The discrepancy has its largest values when is calculated between two dissimilar subsets. In Fig. 5.13 we can see that change points are detected for large discrepancy values. These correspond to peaks in the discrepancy curve (see Fig. 5.13).

To detect the change points in the AGN light curve I used the following information:

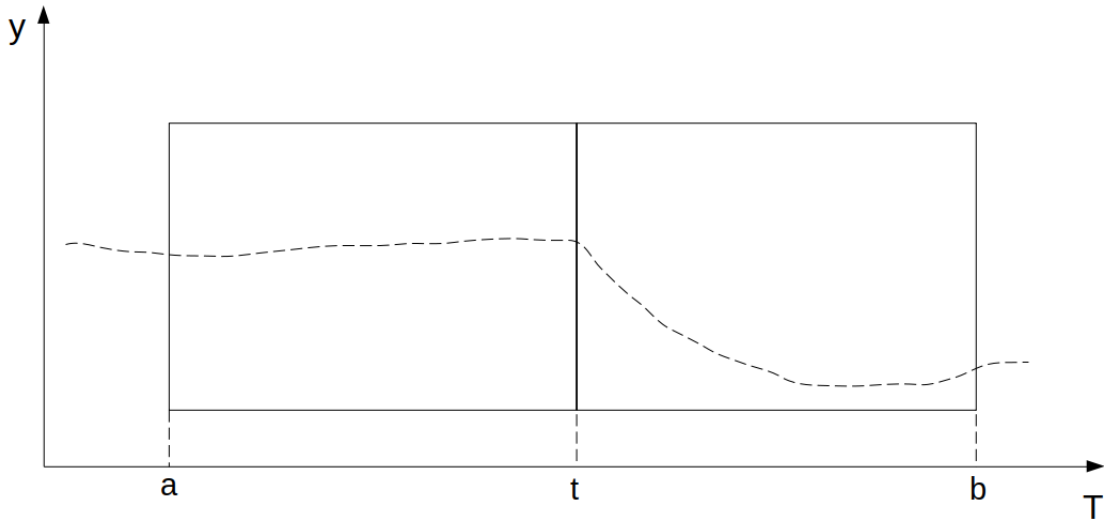

Figure 5.12: Illustration of two adjacent sliding windows in a given time series T. The dashed line is the signal. The two rectangles are two sliding windows covering a time interval $a \leq t$ and $b \geq t$, respectively.

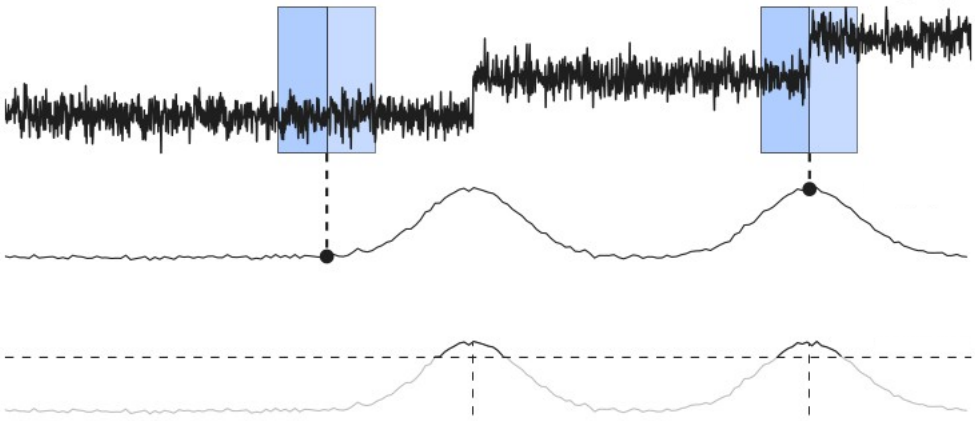

Figure 5.13: Schematic view of the Window-based change point detection method. The time series on the top is the original signal, the one in the middle is the discrepancy curve and the one on the bottom is still the discrepancy curve where the peaks of the curve are highlighted. We have a change point for each peak of the discrepancy curve. Credit: Truong et al. (2020).

- the number of change points in the time series is 2 as we expect the GW source to have a burst behaviour with a rising peak and then a decline.
- The burst is approximately located between 1000 and 1200 days as shown in Fig. 5.9.

The cost function adopted is the least squared deviation defined by the following equation:

$$c(y_I) = \sum_{k=1}^{N} ||y_t - \bar{y}||^2, \tag{5.2}$$

where $\bar{y}$ is the mean of the signal y in the interval I. This function can be used to detect mean-shift in a signal and is implemented by the $Python$ package $ruptures$.

The length of the sliding windows was chosen with an empirical method to detect change points in an interval consistent with the one described by the Local Level Model in Fig 5.9 (1000 - 1200 days). Setting for each window a number of samples (data points) $n < 14$ gave a change point at $t = 1307$ days which is not consistent with the target interval 1000-1200 days. With $n > 49$ the method shows a change point at $t = 617.4$ days which is also not consistent with the interval 1000-1200 days. Hence, the suitable number of samples must be $13 < n < 50$. For $13 < n < 50$ we have change points at $t_1 = 1009$ and $t_2 = 1114$ days. This was hence the chosen number of samples. In Fig. 5.14 the location of the change points is represented.

The detection of the change points gives the precise segment of the light curve which is dominated by the gravitational waves event. The light curve subset outside this segment is instead dominated by the AGN.

The usage of the Local Level Model combined with the change point detection hence shows that the transient source dominated between 1009 and 1114 days. Note that this estimation is close to the actual one. Because I used a simulated AGN, I actually know which data points are originated by the GW event and which data points are simulated. A check of the origin of every single data point revealed that the GW dominated between 987 and 1091 days which is close the interval predicted by the change points detection method.

Note that the Window-based search method is only one of several change point detection methods available in literature (see Truong et al. 2020). Other change point detection methods were also used and resulted in providing the same change point location found with the Window-based search method.

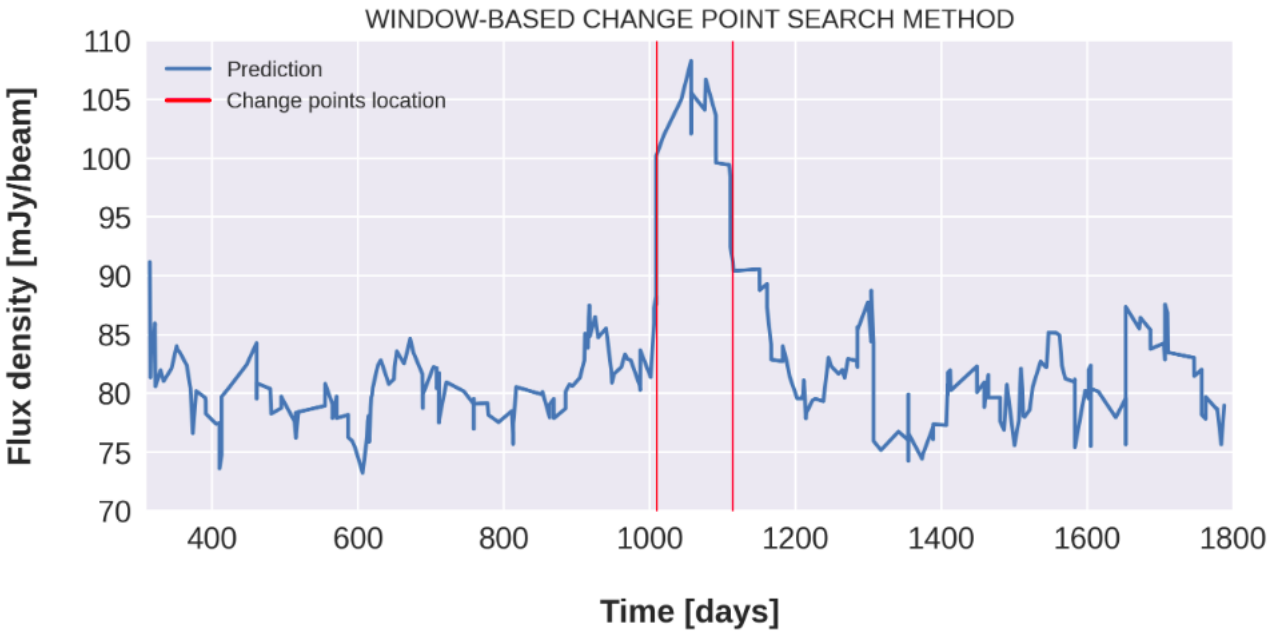

Figure 5.14: Change points location detected with the window-based method.

5.3 Conclusions

In this Chapter, the usage of State Space Models demonstrated a possible technique for detecting transient sources hosted by a variable active galaxy. The method has been applied to a gravitational waves source but can be used for every kind of transient.

The usage of State Space Models also open new scenarios such as the usage of change points detection in time series. Thanks to change point detection methods it is possible to know the exact locations of a transient activity in a light curve such as in the scenario of the GW event hosted by an active galaxy. Furthermore, change points detection could be used even for detecting the given time t when a light curve shows a variable behaviour.

This Chapter also showed a time series decomposition only mentioned in Chapter 4. In this Chapter, the time series model SSARIMA (3,1,25) was decomposed to analyse the autoregressive component. However, other components of the model are also interesting. For example, a moving average component order MA = 25 describes a strong stochastic behaviour. This property would not be described by the traditional metrics such as modulation index and χ^2.

CHAPTER 6

CONCLUSIONS

In this last Chapter, I summarise the main results of this thesis and also outline future possible development for all the research projects described in the previous chapters.

6.1 Main thesis findings and future research

6.1.1 Gamma-ray burst GRB190114C investigation

Chapter 2 describes a study of the gamma-ray burst grb190114c. This gamma-ray burst was the third burst detected from the same source as there had also been two previous bursts (GRBs 180720B and 190829A). The source was initially detected by MAGIC in the TeV regime (MAGIC Collaboration et al., 2019) and a radio detection was obtained within 24 hours post-burst. The source is particularly interesting as it was the first GRB detected at this energy regime (0.2-1 TeV). Radio observations at 5 and 9 GHz are likely to be affected by interstellar scintillation (Lazio et al. 2001). This is also suggested by the early drop at roughly 5 days post-burst (see Fig. 2.2). Misra et al. (2021) confirms this interpretation by claiming the presence of weak and strong scintillation.

Multi-wavelength observations and TeV regime modelling show that high energy photons are caused by up-scattered synchrotron photons (MAGIC Collaboration et al., 2019). Misra et al. (2021) rule out the standard fireball model. In detail, the standard model assumes that the energy in the magnetic field ϵ_B and the energy in non-thermal electrons ϵ_e are constant during the shock evolution (Misra et al., 2021). However, the

multi-wavelength evolution is not consistent with the model. Misra et al. (2021) propose a model where ϵ_B and ϵ_e change over time. More sophisticated models could be tested with these radio observations.

Models including lateral jet expansion and jet dynamics could explain unclear components in the latest model (Misra et al., 2021). For instance, the early reverse shock emission at millimeter wavelengths is not explained by the model proposed by Misra et al. (2021). Moreover, the coming era of the Square Kilometre Array (SKA) may provide more detailed observations and grow our knowledge about these extreme events.

6.1.2 A flare stars study

In Chapter 2 a study of flare stars is described. Radio observations of the two M-dwarf binary systems AT Mic (Sasaki et al., 2019) and UV Ceti (Lynch et al., 2017) are reported. ATCA radio observations were triggered 1 hour post-flare for AT Mic and 13 hours post-flare for UV Ceti. I observed circular polarisation at 5 and 9 GHz from both the two stellar system. This is an interesting result as previous works in literature claimed circular radiation only at lower frequencies (e.g. Dulk 1985). For both the two systems the flare could be caused by gyrosynchrotron radiation, electron cyclotron maser (Leto et al., 2016) or plasma radiation (Dulk, 1985). The flare stars light curves are in Fig. 2.5 and Fig. 2.6.

More observations may definitely help to understand the radiation process causing flares. Pritchard et al. (2021) analysed data from a circular polarization survey for radio stars in the RACS survey with observations centered at 887.5 MHz and a bandwidth of 288 MHz. Because circular polarisation was also observed in AT Mic and UV Ceti, it could be interesting to compare ATCA observations at 5 and 9 GHz with ASKAP data below 1 GHz. Future SKA observations may also allow the detection of fainter objects.

A campaign for detecting ultra-cool dwarfs was also described in Chapter 2. The target of this research field is to understand how the stellar magnetosphere is generated, how the plasma is generated, and how electrons reach the necessary energy to cause the observed gyrosynchrotron emission. To better understand the physics of ultra-cool dwarfs more detections would be required. At the moment of writing this thesis, only 25 objects have been detected.

In Chapter 2 a new method for detecting ultra-cool dwarfs was also described. The strategy consisted in targeting objects with rapid rotation and photometric variability. As a result, at least 3 detections out of 11 observations were achieved. There is also an uncertain detection that might increase the number of detections from 3 to 4. This

search strategy is promising and may help on answering the open questions about these sources.

6.1.3 Radio variable AGN in VAST-P1 and RACS

In Chapter 3 a study of variable AGN was reported. In a sample of 4008 AGN selected from the first release of VAST and RACS, 30 sources were variable (corresponding to 0.7% of the sample). The variable AGN have modulation indices between 26% and 84% with timescales of months.

The most likely explanation for the observed variability is scintillation as the brightness temperature values are above the Compton catastrophe limit of 10^{12}K. The observed modulation index values were also compared to a scintillation model (Hancock et al., 2019). The measured values were systematically lower than the predicted ones. Because the model is likely to overestimate the modulation indices (Hancock et al., 2019).

The subsequent data releases of RACS and VAST would allow more epochs spanning timescales on the order of years. This would open the possibility of AGN that are variables with timescales longer than one year. I recall that one year is the timescale spanning the observations of RACS and VAST-P1.

Multi-wavelength observations may also play an important role for future studies to investigate the intrinsic variability in AGN. The study in Chapter 3 showed that RISS is the most likely cause of the observed variability in the AGN found in VAST and RACS. Hence, this analysis involved extrinsic variability. However, RISS and intrinsic variability are connected through compactness of sources (Koay et al. 2018, Said et al. 2020). This relation may be studied thanks to multi-wavelength analysis.

Multi-wavelength time-domain analysis could provide useful clues on the origin of the relativistic radio-jets and the high energy emission site in AGN (Blandford et al., 2019b). Readhead et al. (1978) found that the higher radio frequency the closer to the supermassive black hole through an investigation of detailed maps of radio sources (identified as QSOs) at different frequency regimes. Images show a rotation of the position angle of radio sources increasing the distance from the core. However, increasing the frequency, the main radio emission belongs to the same location of the optical source in a compact region ($\leq$ 100 Kpc).

Max-Moerbeck et al. (2014) suggested that the gamma emission region should be closer to the central engine. Nevertheless, Kim, Dae-Won et al. (2020) describes the gamma and the radio emission region to be in the same site. Therefore, the position of different bands in AGN is still not completely understood (Blandford et al., 2019b). The

interest in multi-wavelength analysis has caused the publication of several studies at various frequency regimes such as at 154 MHz (Bell et al. 2014), at 1.4 GHz (Hancock et al. 2016, Hodge et al. 2013, Ofek & Frail 2011), at 3.1 GHz (Bower et al. 2011), at 5.5 GHz (Bell et al. 2015) and comparing data at 5 GHz and 15 GHz (Koay et al. 2018).

All the results mentioned in this Section, lead to possible future developments that can be aimed even thanks to new telescopes. The next generation of telescopes with eROSITA[1] and SKA could improve our understanding of AGN behaviour across the different bands of the electromagnetic spectrum.

6.1.4 State Space Models in time domain astronomy

The metrics currently used in time domain astronomy to identify variables and transients are based on modulation index and χ^2 (see 3.3 and eq. 3.4). This metrics describe the overall modulation and significance of time series while the ordering of the data is not described. State Models can report more properties that are reported below:

- slope, rise or decline for a given time t.
- Shocks in time series.
- Autoregression processes capable of describing stochastic behaviour.
- Stationary or non-stationary behaviour of time series.
- Identification of trend change in time series with change point detection.

These properties were explained in Chapter 4 and 5. In particular, in Chapter 4 State Space Models were used to fit GW170814 light curve while in Chapter 5 were used to detect the same GW event within a simulated scintillating active galaxy.

The usage of these models open several research scenarios in Astrophysics such as the possibility to classify transients. A common problem in time domain astronomy is to identify the class of transients. State Space Models could identify the typical properties of a flare star, a gravitational waves event, a gamma-ray burst and so on.

The properties listed above, could be linked to the physical process generating the variable and transient behaviour we observe in astronomical objects (e.g. a stochastic trend could suggest scintillation).

[1] https://www.mpe.mpg.de/eROSITA

State Space Models could also be used for detecting transients hosted by another source. This is a scenario described in Chapter 5 and Keane et al. (2016), where a transient is hosted by an active galaxy.

APPENDIX

A.1 State Space Models in Python

In this Appendix, fragments of the Python code used to fit State Space Models are shown. This is the same code used for the analysis and results described in Chapter 4 and 5.

The code shows how to fit different State Space Models on time series and how to estimate statistical parameters (AIC, BIC, HQIC and Heteroskedasticity).

The models adopted are based on the Python library *statsmodels* which contains a list of functions specifically designed for using State Space Models. In Fig. A.1 we can see the code used for the statistical analysis of the State Space Autoregression Model. The model is defined by the function SARIMAX() of the *stasmodels* library. The SARIMAX() function is used for State Space ARIMA Models and in this case an ARIMA model of order (p=2, d=0, q=0) is used. This model can be seen as an Autoregression process of order 2. In Fig. A.1 we can see that several parameters are estimated such as AIC, BIC, HQIC and Heteroskedasticity. The usage of the other parameters was beyond the goals of this thesis but it is possible to learn more thanks to the *statsmodels* documentation[1].

The code for fitting a time series with the Autoregression process is in Fig. A.2. The code also includes the confidence region of the model. The plot produced by the code in Fig. A.2 was in Chapter 4 and it is shown in this appendix again (see Fig A.3).

In Fig. A.4 there is the code adopted to define the Local Level Model. This code is based on the LocalLinearTrend class. As the name suggests this class can be used to also

[1] https://www.statsmodels.org/stable/index.html

AR state model

In [1394]:
```
# Load the statsmodels api
import statsmodels.api as sm

# Load your dataset
endog = data['scaled_flux']

# We could fit an AR(2) model, described above
mod_ar2 = sm.tsa.SARIMAX(endog, order=(2,0,0))
# Note that mod_ar2 is an instance of the SARIMAX class

# Fit the model via maximum likelihood
res_ar2 = mod_ar2.fit()
# Note that res_ar2 is an instance of the SARIMAXResults class

# Show the summary of results
print(res_ar2.summary())
```

```
                               SARIMAX Results
==============================================================================
Dep. Variable:             scaled_flux   No. Observations:                   66
Model:               SARIMAX(2, 0, 0)   Log Likelihood                -271.963
Date:                Tue, 18 Oct 2022   AIC                            549.927
Time:                        13:06:44   BIC                            556.496
Sample:                             0   HQIC                           552.522
                                  - 66
Covariance Type:                  opg
==============================================================================
                 coef    std err          z      P>|z|      [0.025      0.975]
------------------------------------------------------------------------------
ar.L1          0.5536      0.107      5.185      0.000       0.344       0.763
ar.L2          0.4243      0.103      4.136      0.000       0.223       0.625
sigma2       212.3411     31.810      6.675      0.000     149.994     274.688
===================================================================================
Ljung-Box (Q):                       28.25   Jarque-Bera (JB):                 5.63
Prob(Q):                              0.92   Prob(JB):                         0.06
Heteroskedasticity (H):               3.50   Skew:                             0.24
Prob(H) (two-sided):                  0.00   Kurtosis:                         4.35
===================================================================================
```

Figure A.1: State Space Autoregression Model analysis.

define the Local Linear Trend Model. The Local Linear Trend Model is a generalisation of the Local Level Model. The difference between the two models is a slope component in the Local Linear Trend Model not included in the Local Level Model. In terms of coding, this means to have different coefficients in the matrices defining the model (compare the matrices in Fig. A.4 and A.5). Note also Fig. A.6 where there is the code used for plotting the Local Level Model on a time series. Finally, in Fig A.7 we can see the plot created by the plot.

In [1403]:

```
data.index = data.t

predict_mle = res_ar2.get_prediction()

predict_mle_ci = predict_mle.conf_int(alpha=0.05)
predict_mle_index = data.index

#predict_mle.predicted_mean.index = data.index

# Graph
fig, ax = plt.subplots(figsize=(9,4), dpi=300)


# Plot data points
data['scaled_flux'].plot(ax=ax, style='k.', label='Observed')


dy=data['scaled_rms']
plt.errorbar(data.index,data['scaled_flux'], yerr=dy, fmt='k.');

# Plot predictions
#predict_mle.predicted_mean.plot(ax=ax, style='-', label='One-step-ahead forecast')
predizione.plot(ax=ax, style='-', label='One-step-ahead forecast')

ax.fill_between(predict_mle_index[2:], predict_mle_ci.iloc[2:, 0], predict_mle_ci.iloc[2:, 1], alpha=0.1)

ax.legend(loc='upper left')

plt.title("STATE SPACE AUTOREGRESSION MODEL")

#axis
plt.xlabel('Time [days]', labelpad = 20, weight='bold', size=15)
plt.ylabel('Flux density [mJy/beam]', labelpad = 20, weight='bold', size=15)

plt.ylim(0,175)
plt.xlim(0.1,320)


plt.show()
```

Figure A.2: Code for fitting State Space Autoregression Model on a time series.

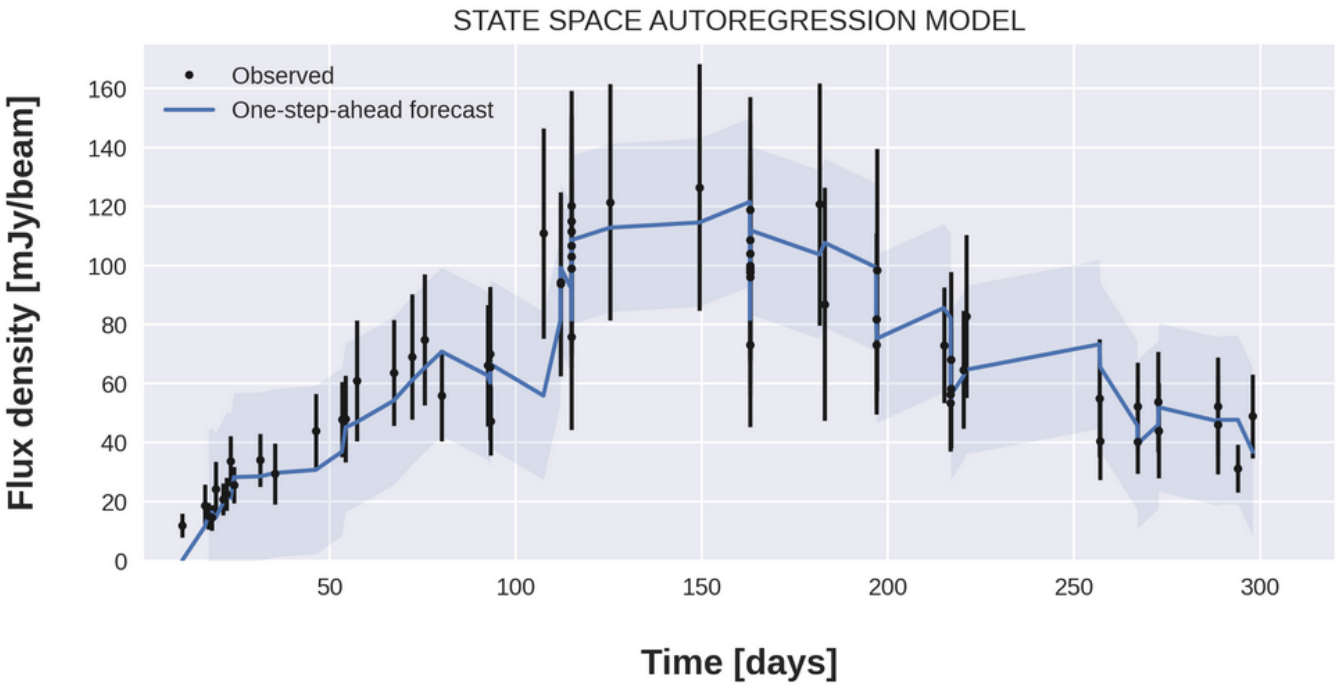

Figure A.3: AR model in space state representation form (blue fitting and light blue confidence region) with GW170817 light curve (black points and black error bars).

LOCAL LEVEL MODEL

In [1417]:
```python
class LocalLinearTrend(sm.tsa.statespace.MLEModel):
    def __init__(self, endog):
        # Model order
        k_states = k_posdef = 2

        # Initialize the statespace
        super(LocalLinearTrend, self).__init__(
            endog, k_states=k_states, k_posdef=k_posdef,
            initialization='approximate_diffuse',
            loglikelihood_burn=k_states
        )

        # Initialize the matrices
        self.ssm['design'] = np.array([1, 0])
        self.ssm['transition'] = np.array([[1, 0],
                                           [0, 0]])
        self.ssm['selection'] = np.eye(k_states)

        # Cache some indices
        self._state_cov_idx = ('state_cov',) + np.diag_indices(k_posdef)

    @property
    def param_names(self):
        return ['sigma2.measurement', 'sigma2.level', 'sigma2.trend']

    @property
    def start_params(self):
        return [np.std(self.endog)]*3

    def transform_params(self, unconstrained):
        return unconstrained**2

    def untransform_params(self, constrained):
        return constrained**0.5

    def update(self, params, *args, **kwargs):
        params = super(LocalLinearTrend, self).update(params, *args, **kwargs)

        # Observation covariance
        self.ssm['obs_cov',0,0] = params[0]

        # State covariance
        self.ssm[self._state_cov_idx] = params[1:]
```

Figure A.4: Code for defining the LocalLinearTrend class which is used for Local Liner Trend Models and Local Level Models.

```python
# Initialize the matrices
self.ssm['design'] = np.array([1, 0])
self.ssm['transition'] = np.array([[1, 1],
                                   [0, 1]])
self.ssm['selection'] = np.eye(k_states)
```

Figure A.5: Matrices defining the Local Linear Trend Model.

In [1419]:
```
predict_mle = res.get_prediction()

predict_mle_ci = predict_mle.conf_int(alpha=0.05)
predict_mle_index = data.index



# Graph
fig, ax = plt.subplots(figsize=(9,4), dpi=300)

# Plot data points
data['scaled_flux'].plot(ax=ax, style='k.', label='Observed')


dy=data['scaled_rms']
plt.errorbar(data.index,data['scaled_flux'], yerr=dy, fmt='k.');

# Plot predictions
predict_mle.predicted_mean.plot(ax=ax, style='-', label='One-step-ahead forecast')

ax.fill_between(predict_mle_index[2:], predict_mle_ci.iloc[2:, 0], predict_mle_ci.iloc[2:, 1], alpha=0.1)

ax.legend(loc='upper left')

plt.title("LOCAL LEVEL MODEL")

#axis
plt.xlabel('Time [days]', labelpad = 20, weight='bold', size=15)
plt.ylabel('Flux density [mJy/beam]', labelpad = 20, weight='bold', size=15)

plt.ylim(0,175)
plt.xlim(0.000001,320)


plt.show()
```

Figure A.6: Code for fitting the Local Level Model on a time series.

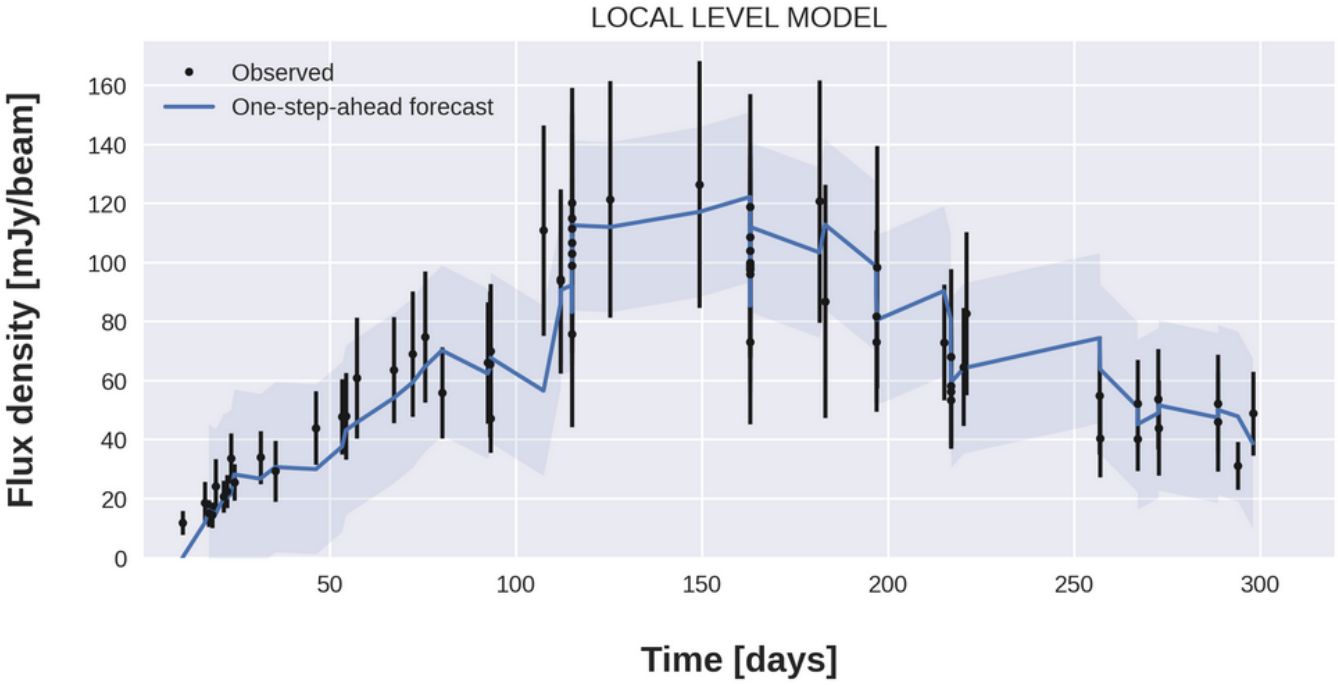

Figure A.7: Local Level Model (blue fitting and light blue confidence region) with GW170817 light curve (black points and black error bars).

Bibliography

Abbott B. P., et al., 2016a, Phys. Rev. Lett., 116, 061102

Abbott B. P., et al., 2016b, Phys. Rev. Lett., 116, 061102

Abbott B. P., et al., 2016c, Phys. Rev. Lett., 116, 061102

Abbott B. P., et al., 2016d, The Astrophysical Journal, 826, L13

Abbott B., et al., 2017a, Physical Review Letters, 119

Abbott B. P., et al., 2017b, , 551, 85

Acernese F., et al., 2014, Classical and Quantum Gravity, 32, 024001

Allison J. R., et al., 2021, The First Large Absorption Survey in HI (FLASH): I. Science Goals and Survey Design (arXiv:2110.00469)

Aminikhanghahi S. C. D., 2016, Knowledge and Information Systems, 51, 339,Äì367

Anderson G. E., et al., 2014, Monthly Notices of the Royal Astronomical Society, 440, 2059

Anderson G. E., et al., 2021, , 503, 4372

Antonova A., Hallinan G., Doyle J., Yu S., Kuznetsov A., Metodieva Y., Golden A., Cruz K., 2013, Astronomy & Astrophysics, 549, A131

Audard M., Güdel M., Drake J. J., Kashyap V. L., 2000, , 541, 396

Avison A., George S. J., 2012, European Journal of Physics, 34, 7,Äì17

Bannister K. W., Stevens J., Tuntsov A. V., Walker M. A., Johnston S., Reynolds C., Bignall H., 2016, Science, 351, 354

Barreto H., Howland F., 2006, Introductory econometrics. Using Monte Carlo simulation with Microsoft Excel. With CD-ROM. Cambridge University Press, https://www.researchgate.net/publication/264950115_Introductory_econometrics_Using_Monte_Carlo_simulation_with_Microsoft_Excel_With_CD-ROM

Bassa C. G., et al., 2016, Monthly Notices of the Royal Astronomical Society: Letters, 463, L36

Bastian T. S., Bookbinder J., Dulk G. A., Davis M., 1990, , 353, 265

Belczynski K., Holz D. E., Fryer C. L., Berger E., Hartmann D. H., O'Shea B., 2010, , 708, 117

Bell M. E., et al., 2014, , 438, 352

Bell M. E., Huynh M. T., Hancock P., Murphy T., Gaensler B. M., Burlon D., Trott C., Bannister K., 2015, , 450, 4221

Berger E., 2014, Annual Review of Astronomy and Astrophysics, 52, 43

Bhandari S., et al., 2018, Monthly Notices of the Royal Astronomical Society, 478, 1784

Bhattacharyya S., Ghosh R., Chatterjee R., Das N., 2020, The Astrophysical Journal, 897, 25

Blandford R. D., Königl A., 1979, , 232, 34

Blandford R., Meier D., Readhead A., 2019a, Annual Review of Astronomy and Astrophysics, 57, 467

Blandford R., Meier D., Readhead A., 2019b, Annual Review of Astronomy and Astrophysics, 57, 467

Bower G. C., Whysong D., Blair S., Croft S., Keating G., Law C., Williams P. K. G., Wright M. C. H., 2011, The Astrophysical Journal, 739, 76

Brockwell Davis 2010, Introduction to Time Series and Forecasting. Springer

Bromberg O., Nakar E., Piran T., Sari R., 2013, , 764, 179

Brooks C., 2008, Univariate time series modelling and forecasting. Cambridge University Press, https://doi.org/10.1017/CBO9780511841644.006

Browning M. K., Miesch M. S., Brun A. S., Toomre J., 2006, The Astrophysical Journal, 648, L157

Bucciantini N., Metzger B. D., Thompson T. A., Quataert E., 2012, , 419, 1537

Burgess A. M., Hunstead R. W., 1995, , 12, 227

Burnham K. P., Anderson D. R., 2002, Model Selection and Multimodel Inference. Springer, http://www.elcom-hu.com/Mshtrk/Statstics/9th%20txt%20book.pdf

Burnham K. P., Anderson D. R., 2004, Sociological Methods & Research, 33, 261

Callingham J. R., et al., 2017, The Astrophysical Journal, 836, 174

Camilo F., et al., 2018, The Astrophysical Journal, 856, 180

Campana S., et al., 2006, , 454, 113

Chornock R., et al., 2017, The Astrophysical Journal, 848, L19

Collaboration L. S., et al., 2015, Classical and Quantum Gravity, 32, 074001

Condon J. J., Cotton W. D., Greisen E. W., Yin Q. F., Perley R. A., Taylor G. B., Broderick J. J., 1998, , 115, 1693

Coulter D. A., et al., 2017, Science, 358, 1556

D'Abrusco R., et al., 2019, , 242, 4

d'Antonio D., Giroletti M., Giovannini G., Maini A., 2019, Monthly Notices of the Royal Astronomical Society, 490, 5798

Dickey J. M., et al., 2013, Publications of the Astronomical Society of Australia, 30, e003

Dobie D., et al., 2018, The Astrophysical Journal, 858, L15

Dobie D., Murphy T., Kaplan D. L., Ghosh S., Bannister K. W., Hunstead R. W., 2019, , 36, e019

Donnarumma I., Rossi E. M., Fender R., Komossa S., Paragi Z., Van Velzen S., Prandoni I., 2015, in Advancing Astrophysics with the Square Kilometre Array (AASKA14). p. 54 (arXiv:1501.04640)

Drout M. R., et al., 2017, Science, 358, 1570

Dulk G. A., 1985, , 23, 169

Durbin J., Koopman S. J., 2012, Time Series Analysis by State Space Methods. Oxford University Press, Incorporated, https://www.researchgate.net/publication/227468262_Time_Series_Analysis_by_State_Space_Methods

Eracleous M., Shields J. C., Chartas G., Moran E. C., 2002, , 565, 108

Evans P. A., et al., 2017, Science, 358, 1565

Falcke H., Rezzolla L., 2014, , 562, A137

Falomo R., Treves A., 2007, The Messenger, 129, 42

Feigelson E. D., Babu G. J., Caceres G. A., 2018, Frontiers in Physics, 6

Fender R. P., Anderson G. E., Osten R., Staley T., Rumsey C., Grainge K., Saunders R. D. E., 2014, Monthly Notices of the Royal Astronomical Society: Letters, 446, L66

Fong W.-f., Berger E., Margutti R., Zauderer B., 2015, The Astrophysical Journal, 815

Frail D. A., Waxman E., Kulkarni S. R., 2000, The Astrophysical Journal, 537, 191

Gaensler B. M., Landecker T. L., Taylor A. R., POSSUM Collaboration 2010, in American Astronomical Society Meeting Abstracts #215. p. 470.13

Ghirlanda G., Nava L., Ghisellini G., Celotti A., Firmani C., 2009, , 496, 585

Giroletti M., et al., 2016a, , 588, A141

Giroletti M., Marcote B., Garrett M. A., Paragi Z., Yang J., Hada K., Muxlow T. W. B., Cheung C. C., 2016b, , 593, L16

Granot J., Sari R., 2002, , 568, 820

Grupe D., Burrows D. N., Patel S. K., Kouveliotou C., Zhang B., Meszaros P., Wijers R. A. M., Gehrels N., 2006, The Astrophysical Journal, 653, 462

Guzman J., et al., 2019, ASKAPsoft: ASKAP science data processor software (ascl:1912.003)

Hallinan G., Antonova A., Doyle J. G., Bourke S., Lane C., Golden A., 2008, , 684, 644

Hallinan G., et al., 2017, Science, 358, 1579

Hancock P. J., Drury J. A., Bell M. E., Murphy T., Gaensler B. M., 2016, Monthly Notices of the Royal Astronomical Society, 461, 3314

Hancock P. J., Charlton E. G., Macquart J.-P., Hurley-Walker N., 2019, arXiv e-prints, p. arXiv:1907.08395

Harding L. K., Hallinan G., Boyle R. P., Golden A., Singh N., Sheehan B., Zavala R. T., Butler R. F., 2013, The Astrophysical Journal, 779, 101

Heckman T. M., 1980, , 500, 187

Heeschen D. S., Rickett B. J., 1987, , 93, 589

Ho L. C., Filippenko A. V., Sargent W. L. W., 1997, , 487, 568

Hodge J. A., Becker R. H., White R. L., Richards G. T., 2013, , 769, 125

Hotan A. W., et al., 2021, Publications of the Astronomical Society of Australia, 38, e009

Hotokezaka K., Kiuchi K., Kyutoku K., Muranushi T., Sekiguchi Y.-i., Shibata M., Taniguchi K., 2013, Phys. Rev. D, 88, 044026

Hovatta T., Nieppola E., Tornikoski M., Valtaoja E., Aller M. F., Aller H. D., 2008a, , 485, 51

Hovatta T., Nieppola E., Tornikoski M., Valtaoja E., Aller M. F., Aller H. D., 2008b, , 485, 51

Hovatta T., Valtaoja E., Tornikoski M., Lähteenmäki A., 2009, , 494, 527

Hughes P. A., Aller H. D., Aller M. F., 1985, , 298, 301

Hunstead R. W., 1972, , 12, 193

Huynh M. T., Hopkins A. M., Lenc E., Mao M. Y., Middelberg E., Norris R. P., Randall K. E., 2012, Monthly Notices of the Royal Astronomical Society, 426, 2342

Hyndman R. J., 2018, Forecasting: principles and practice. OTexts, https://otexts.com/fpp2/

Indermuehle B. T., Harvey-Smith L., Marquarding M., Reynolds J., 2018, in Peck A. B., Seaman R. L., Benn C. R., eds, Vol. 10704, Observatory Operations: Strategies, Processes, and Systems VII. SPIE, pp 1007 – 1012, doi:10.1117/12.2311917, https://doi.org/10.1117/12.2311917

Johns-Krull C. M., Valenti J. A., 1996, The Astrophysical Journal Letters, 459, L95

Johnston S., et al., 2007, , 24, 174

Johnston S., et al., 2016, Monthly Notices of the Royal Astronomical Society, 465, 2143

Jonas J., MeerKAT Team 2016, in MeerKAT Science: On the Pathway to the SKA. p. 1, doi:10.22323/1.277.0001

Kao M. M., Hallinan G., Pineda J. S., Escala I., Burgasser A., Bourke S., Stevenson D., 2016, The Astrophysical Journal, 818, 24

Kasen D., Metzger B., Barnes J., Quataert E., Ramirez-Ruiz E., 2017, Nature, 551

Kasliwal M. M., et al., 2017, Science, 358, 1559

Keane E. F., et al., 2016, , 530, 453

Kellermann K. I., Pauliny-Toth I. I. K., 1969, , 155, L71

Kelly B. C., Becker A. C., Sobolewska M., Siemiginowska A., Uttley P., 2014, The Astrophysical Journal, 788, 33

Khachikian E. Y., Weedman D. W., 1974, , 192, 581

Kim, Dae-Won Trippe, Sascha Kravchenko, Evgeniya V. 2020, A&A, 636, A62

Kinney A. L., Bohlin R. C., Blades J. C., York D. G., 1991, , 75, 645

Koay J. Y., et al., 2018, , 474, 4396

Koay J. Y., et al., 2019, , 489, 5365

Kochanek C. S., 1994, , 422, 508

Koopman S. J., Durbin J., 2012, Time Series Analysis by State Space Methods: Second Edition. OUP Catalogue, Oxford University Press

Koribalski B. S., et al., 2020, Astrophysics and Space Science, 365

Kudryavtseva N. A., et al., 2011, , 526, A51

Lähteenmäki A., Valtaoja E., Wiik K., 1999, , 511, 112

Lamb G. P., Kobayashi S., 2019, Monthly Notices of the Royal Astronomical Society, 489, 1820

Laskar T., et al., 2019, The Astrophysical Journal, 878, L26

Lattimer J. M., Schramm D. N., 1974, , 192, L145

Lazio T. J. W., Waltman E. B., Ghigo F. D., Fiedler R. L., Foster R. S., Johnston K. J., 2001, The Astrophysical Journal Supplement Series, 136, 265

Lazio T. J. W., Cordes J., de Bruyn A., Macquart J.-P., 2004, New Astronomy Reviews, 48, 1439

Lazzati D., Ramirez-Ruiz E., Ghisellini G., 2001, , 379, L39

Leto P., Trigilio C., Buemi C. S., Umana G., Ingallinera A., Cerrigone L., 2016, Monthly Notices of the Royal Astronomical Society, 459, 1159

Lin D. N. C., Shields G. A., 1986, , 305, 28

Liu S., 2021, Regression: Book One, Series of Machine Learning with Scikit-Learn. https://www.amazon.com/Regression-Book-Machine-Learning-Scikit-Learn/dp/B09BGHXBY6

Lorimer D. R., Bailes M., McLaughlin M. A., Narkevic D. J., Crawford F., 2007, Science, 318, 777

Lovell J. E. J., Jauncey D. L., Bignall H. E., Kedziora-Chudczer L., Macquart J. P., Rickett B. J., Tzioumis A. K., 2003, , 126, 1699

Lovell J. E. J., et al., 2008, , 689, 108

Lynch C., Murphy T., Ravi V., Hobbs G., Lo K., Ward C., 2016, Monthly Notices of the Royal Astronomical Society, 457, 1224

Lynch C., Murphy T., Kaplan D. L., 2017, MWA targeted campaign of nearby, flaring M dwarf stars, MWA Proposal id.2017A-02

MAGIC Collaboration et al. 2019, Nature, 575, 2006

MacFadyen A. I., Ramirez-Ruiz E., Zhang W., 2005, arXiv e-prints, pp astro–ph/0510192

Macquart J. P., de Bruyn A. G., 2006, , 446, 185

Macquart J.-P., et al., 2010, , 27, 272

Malesani D., et al., 2007, , 473, 77

Margutti R., et al., 2011, Monthly Notices of the Royal Astronomical Society, 417, 2144

Margutti R., et al., 2018, , 856, L18

Massaro E., Maselli A., Leto C., Marchegiani P., Perri M., Giommi P., Piranomonte S., 2015a, , 357, 75

Massaro E., Maselli A., Leto C., Marchegiani P., Perri M., Giommi P., Piranomonte S., 2015b, , 357, 75

Max-Moerbeck W., et al., 2014, Monthly Notices of the Royal Astronomical Society, 445, 428

McCallum J. N., Ellingsen S. P., Lovell J. E. J., 2007, , 376, 549

McConnell D., et al., 2020, , 37, e048

McKernan B., Ford K. E. S., Reynolds C. S., 2010, , 407, 2399

McMullin J. P., Waters B., Schiebel D., Young W., Golap K., 2007, in Shaw R. A., Hill F., Bell D. J., eds, Astronomical Society of the Pacific Conference Series Vol. 376, Astronomical Data Analysis Software and Systems XVI. p. 127

Melrose D. B., 2017, Reviews of Modern Plasma Physics, 1, 5

Metzger B. D., Quataert E., Thompson T. A., 2008, , 385, 1455

Metzger B. D., Williams P. K. G., Berger E., 2015, The Astrophysical Journal, 806, 224

Meyer M., 2009, Exploring the HI Universe with ASKAP (arXiv:0912.2167)

Michelson A. A., Morley E. W., 1887, American Journal of Science, s3-34, 333

Miller-Jones J. C. A., Gallo E., Rupen M. P., Mioduszewski A. J., Brisken W., Fender R. P., Jonker P. G., Maccarone T. J., 2008, , 388, 1751

Misra K., et al., 2021, Monthly Notices of the Royal Astronomical Society, 504, 5685

Mitra-Kraev U., et al., 2005, , 431, 679

Mooley K. P., et al., 2016, , 818, 105

Mooley K. P., et al., 2018, , 554, 207

Morin J., Dormy E., Schrinner M., Donati J. F., 2011, , 418, L133

Murguia-Berthier A., et al., 2017, , 848, L34

Murphy T., et al., 2013, , 30, e006

Murphy T., et al., 2021, arXiv e-prints, p. arXiv:2108.06039

Nakar E., 2007, Physics Reports, 442, 166

Nakar E., Piran T., 2002, , 330, 920

Nakar E., Piran T., 2011, , 478, 82

Nakar E., Piran T., 2018, Monthly Notices of the Royal Astronomical Society, 478, 407,Äì415

Narayan R., Paczynski B., Piran T., 1992, , 395, L83

Nichols J., Burleigh M. R., Casewell S. L., Cowley S. W., Wynn G. A., Clarke J., West A., 2012, The Astrophysical Journal, 760, 59

Norris J. P., Gehrels N., Scargle J. D., 2011, The Astrophysical Journal, 735, 23

Norris R. P., et al., 2021, , 38, e003

Ofek E. O., Frail D. A., 2011, The Astrophysical Journal, 737, 45

Osten R. A., Hawley S. L., Allred J. C., Johns-Krull C. M., Roark C., 2005, The Astrophysical Journal, 621, 398

Osten R. A., Drake S., Tueller J., Cummings J., Perri M., Moretti A., Covino S., 2007, , 654, 1052

Osten R. A., et al., 2010, The Astrophysical Journal, 721, 785

Osten R. A., et al., 2016, The Astrophysical Journal, 832, 174

Padovani P., et al., 2017, , 25, 2

Partridge B., López-Caniego M., Perley R. A., Stevens J., Butler B. J., Rocha G., Walter B., Zacchei A., 2016, The Astrophysical Journal, 821, 61

Pietka M., Fender R. P., Keane E. F., 2014, Monthly Notices of the Royal Astronomical Society, 446, 3687

Pineda J. S., Hallinan G., 2018, The Astrophysical Journal, 866, 155

Pineda J. S., Hallinan G., Kao M. M., 2017, The Astrophysical Journal, 846, 75

Pintaldi S., Stewart A., O'Brien A., Kaplan D., Murphy T., 2021, A scalable transient detection pipeline for the Australian SKA Pathfinder VAST survey (arXiv:2101.05898)

Piran T., 1999, , 314, 575

Piran T., Nakar E., 2010, The Astrophysical Journal, 718, L63

Piran T., Nakar E., Rosswog S., 2013, Monthly Notices of the Royal Astronomical Society, 430, 2121

Planck Collaboration et al., 2016, , 594, A13

Prentice S., et al., 2018, The Astrophysical Journal Letters, 865, L3

Price D. C., 2016, PyGSM: Python interface to the Global Sky Model (ascl:1603.013)

Prieto M. A., Reunanen J., Tristram K. R. W., Neumayer N., Fernandez-Ontiveros J. A., Orienti M., Meisenheimer K., 2010, Monthly Notices of the Royal Astronomical Society, 402, 724

Pritchard J., et al., 2021, , 502, 5438

Radice D., Perego A., Hotokezaka K., Bernuzzi S., Fromm S. A., Roberts L. F., 2018, , 869, L35

Ravi V., Hallinan G., Hobbs G., Champion D. J., 2011, The Astrophysical Journal Letters, 735, L2

Readhead A. C. S., Cohen M. H., Pearson T. J., Wilkinson P. N., 1978, , 276, 768

Reiners A., Mohanty S., 2012, , 746, 43

Resmi L., Zhang B., 2016, , 825, 48

Rickett B. J., 1990, , 28, 561

Riess A. G., et al., 2016, , 826, 56

Route M., Wolszczan A., 2016, The Astrophysical Journal, 830, 85

Rowlinson A., O'Brien P. T., Metzger B. D., Tanvir N. R., Levan A. J., 2013, Monthly Notices of the Royal Astronomical Society, 430, 1061

Rowlinson A., et al., 2019, Astronomy and Computing, 27, 111

Said N. M. M., Ellingsen S. P., Bignall H. E., Shabala S., McCallum J. N., Reynolds C., 2020, , 498, 4615

Sarbadhicary S. K., et al., 2020, arXiv e-prints, p. arXiv:2009.05056

Sari R., Esin A. A., 2001, The Astrophysical Journal, 548, 787

Sari R., Piran T., 1995, , 455, L143

Sari R., Piran T., 1999, The Astrophysical Journal, 517, L109

Sarkar A., Gupta A. C., Chitnis V. R., Wiita P. J., 2020, Monthly Notices of the Royal Astronomical Society, 501, 50

Sasaki R., et al., 2019, The Astronomer's Telegram, 12748, 1

Sault R. J., Teuben P. J., Wright M. C. H., 1995, in Shaw R. A., Payne H. E., Hayes J. J. E., eds, Astronomical Society of the Pacific Conference Series Vol. 77, Astronomical Data Analysis Software and Systems IV. p. 433 (arXiv:astro-ph/0612759)

Savchenko V., et al., 2017, , 848, L15

Schulze S., et al., 2019, GRB Coordinates Network, 23745, 1

Seaman R., et al., 2011

Sekiguchi Y., Kiuchi K., Kyutoku K., Shibata M., Taniguchi K., 2016, , 93, 124046

Sharma S., Swayne D., Obimbo C., 2016, Energy, Ecology and Environment, 1

Shields G. A., Wheeler J. C., 1978, , 222, 667

Shulyak D., Reiners A., Engeln A., Malo L., Yadav R., Morin J., Kochukhov O., 2017, Nature Astronomy, 1, 1

Shumway R. H., Stoffer D. S., 2017, Time Series Analysis and Applications. Springer, https://link.springer.com/book/10.1007/978-3-319-52452-8

Singer L. P., Price L. R., 2016, Phys. Rev. D, 93, 024013

Smartt S. J., et al., 2018, The Astronomer's Telegram, 11727, 1

Stasińska G., et al., 2008, , 391, L29

Stickel M., Padovani P., Urry C. M., Fried J. W., Kuehr H., 1991, , 374, 431

Swinbank J., 2014, Astronomy and Computing, 7-8, 12

Swinbank J. D., et al., 2015, Astronomy and Computing, 11, 25

Templeton M. R., Karovska M., 2009, The Astrophysical Journal, 691, 1470

Thompson et al. Moran J.M. S. G., 2017, Interferometry and Synthesis in Radio Astronomy. Springer, Cham, https://doi.org/10.1007/978-3-319-44431-4_3

Troja E., et al., 2017, , 551, 71

Truong C., Oudre L., Vayatis N., 2020, Signal Processing, 167, 107299

Tuntsov A. V., Stevens J., Bannister K. W., Bignall H., Johnston S., Reynolds C., Walker M. A., 2017, , 469, 5023

Tusell F., 2008, Journal of the Royal Statistical Society Series A, 171, 756

Ulrich M.-H., Maraschi L., Urry C. M., 1997, , 35, 445

Urry C. M., Padovani P., 1995, , 107, 803

Véron-Cetty M. P., Véron P., 2010, , 518, A10

Wang Y., Tuntsov A., Murphy T., Lenc E., Walker M., Bannister K., Kaplan D. L., Mahony E. K., 2021, Monthly Notices of the Royal Astronomical Society, 502, 3294

Wei W. W. S., 2019, Multivariate Time Series Analysis and Applications. Wiley, https://www.wiley.com/en-us/Multivariate+Time+Series+Analysis+and+Applications-p-9781119502852

Whiting M. T., 2012, Monthly Notices of the Royal Astronomical Society, 421, 3242

Williams P. K. G., Berger E., 2016, , 821, L22

Williams P. K. G., Berger E., Irwin J., Berta-Thompson Z., Charbonneau D., 2015a, The Astrophysical Journal, 799, 192

Williams P. K. G., Casewell S. L., Stark C. R., Littlefair S. P., Helling C., Berger E., 2015b, , 815, 64

Wilson W. E., et al., 2011, Monthly Notices of the Royal Astronomical Society, 416, 832

Wright E. L., et al., 2010, , 140, 1868

Zhang B., 2014, , 780, L21

Zhang S.-N., Liu Y., Yi S., Dai Z., Huang C., 2016, Do we expect to detect electromagnetic radiation from merging stellar mass black binaries like GW150914? No, doi:10.48550/ARXIV.1604.02537, https://arxiv.org/abs/1604.02537

Zhang P., Guo Y., Wang L., Liu S., 2018, , 615, A48

Zheng H., et al., 2016, Monthly Notices of the Royal Astronomical Society, 464, 3486

Zic A., et al., 2019, , 488, 559

Zwart J. T. L., et al., 2008, Monthly Notices of the Royal Astronomical Society, 391, 1545